

# Important Notice

This copy may be used only for the purposes of research and private study, and any use of the copy for a purpose other than research or private study may require the authorization of the copyright owner of the work in question. Responsibility regarding questions of copyright that may arise in the use of this copy is assumed by the recipient.

UNIVERSITY OF CALGARY

A Multicomponent Walkaway Vertical Seismic Profile Experiment in a Heavy Oil Reservoir

by

Bona Wu

A THESIS

SUBMITTED TO THE FACULTY OF GRADUATE STUDIES  
IN PARTIAL FULFILMENT OF THE REQUIREMENTS FOR THE  
DEGREE OF MASTER OF SCIENCE

GRADUATE PROGRAM IN GEOLOGY AND GEOPHYSICS

CALGARY, ALBERTA

APRIL, 2016

© Bona Wu 2016

## **Abstract**

A multicomponent walkaway VSP experiment was successfully processed and used to predict rock properties in a heavy oil reservoir. Post-stack image and pre-stack gathers were made for inversion and AVO analysis. A common shot reflectivity gather was also created for AVO study at the VSP well location. P and S-wave impedance, reflectivity,  $V_p/V_s$  and density were studied. AVO attributes and their crossplots were analyzed. Furthermore, AVO Lambda-mu-rho analysis and AVO modeling were conducted. The analyses helped to identify different lithologies and changes of fluids in the target reservoir. The study showed no obvious gas effects in the target interval, a finding validated by production data. The converted-wave data had good resolution. PP-PS joint inversion added more details to P-wave inversion only. This case study demonstrated that multicomponent VSP is an effective tool to predict rock properties, characterize the reservoir, and monitor production.

## **Acknowledgements**

I sincerely thank my supervisor, Dr. Don C. Lawton, for his guidance and support throughout my M.Sc. program. I have been extremely lucky to have a supervisor who not only cares so much about my study but also is a role model and inspiration to be a good geoscientist.

I would like to thank the directors, staff and students of the CREWES Project at the University of Calgary for their friendship, discussions and helpful insight during my studies. I would like to thank Patricia Esperanza Gavotti for her kind help in my research. I thank my office mates Jessica Dongas, Michelle Montana, and Adriana Gordon for sharing great experience as graduate students. I thank our program manager Laura Baird for her support in my daily study. She makes my study experience enjoyable.

Special thanks to Roy Lindseth for his reviews and edits of this manuscript in his senior years. I admire his dedication to geophysics. He is a true scientist and his spirit inspires me and all other students to devote ourselves to geophysics.

I would like to thank my husband, Zimin Zhang, who has always been encouraging and supportive during my study.

## **Dedication**

I dedicate this thesis to my husband, Zimin Zhang, and my lovely son, Victor Zhang.

## Table of Contents

Abstract .....	ii
Acknowledgements .....	iii
Dedication .....	iv
Table of Contents .....	v
List of Tables .....	vii
List of Figures and Illustrations .....	viii
List of Symbols, Abbreviations and Nomenclature .....	xiv
CHAPTER 1 INTRODUCTION .....	1
1.1 Introduction .....	1
1.2 Thesis objectives .....	1
1.3 Theory and methodology .....	2
1.3.1 VSP seismology .....	2
1.3.2 Converted wave seismology .....	4
1.3.3 Inversion principles .....	4
1.3.4 AVO principles .....	5
1.4 Data used .....	9
1.5 Hardware and software used .....	10
CHAPTER 2 DATA PROCESSING .....	11
2.1 Introduction .....	11
2.2 Processing techniques .....	11
2.2.1 Processing techniques of zero-offset shot .....	11
First arrival picking and velocity computation .....	11
Upgoing and downgoing wavefield separation .....	11
VSP deconvolution .....	12
NMO and statics correction .....	12
Corridor mute and stack .....	13
2.2.2 Processing techniques of offset shots .....	14
Far-offset VSP geometry and horizontal rotation .....	15
Time-variant wavefield separation .....	16
Deconvolution of upgoing P-wave data .....	16
VSP-CDP transform of upgoing P-wave data .....	17
2.3 Field data processing .....	18
2.3.1 Acquisition parameters and raw shot records .....	18
2.3.2 Geometry setup and pre-processing of the VSP data .....	20
2.3.3 Zero-offset VSP processing .....	23
2.3.4 Offset VSP processing .....	30
2.4 Chapter summary .....	37
CHAPTER 3 WALKAWAY VSP ANALYSIS .....	38
3.1 Introduction .....	38
3.2 Phases correction .....	38
3.3 True amplitude recovery .....	39
3.4 Correlation between VSP and synthetic seismogram .....	39

3.5	Registration of PP and PS data .....	43
3.6	Chapter summary .....	47
CHAPTER 4 INVERSION AND AVO ANALYSIS .....		48
4.1	AVO attributes .....	48
4.1.1	Intercept A, Gradient B, and AVO product A*B.....	48
4.1.2	Poisson's Ratio change: A+B .....	48
4.1.3	Shear reflectivity: A-B.....	49
4.1.4	Zero angle P and S-wave reflection coefficients .....	49
4.1.5	Fluid factor.....	50
4.1.6	Lambda-Mu-Rho (LMR) .....	50
4.1.7	Theory of AVO modeling.....	51
4.2	Field data inversion and AVO attributes analysis.....	52
4.2.1	Geological background of studied area.....	52
4.2.2	Inversion analysis.....	53
4.2.3	AVO analysis .....	59
4.2.4	AVO LMR analysis .....	68
4.2.5	AVO modeling.....	69
4.2.6	PP-PS joint inversion .....	71
4.3	Chapter summary .....	73
CHAPTER 5 DISCUSSION AND CONCLUSIONS .....		74
5.1	Conclusions.....	74
5.2	New achievements of this research.....	74
5.3	Discussion and future work .....	75
REFERENCES .....		77

## List of Tables

Table 1-1. AVO classification .....	9
Table 2-1. Main parameters in walkaway VSP acquisition.....	18
Table 3-1. Comparison of calculated $V_p/V_s$ from Garotta method, velocity scanning on seismic and measurements from nearby well log .....	45
Table 4-1. AVO attributes studied in this work.....	48
Table 4-2. Properties of studied reservoir.....	63
Table 4-3. Production of the well A, target formation.....	71

## List of Figures and Illustrations

Figure 1-1. Different types of VSP geometry: (a) zero-offset VSP or check shot survey, (b) offset VSP, (c) walkaway VSP, (d) walk-above VSP, (e) 3D VSP, and (f) 3D reverse VSP (modified from Lines and Newrick, 2004). .....	3
Figure 1-2. Reflection and transmission at an interface between two infinite elastic half-spaces for an incident P-wave (after Castagna and Backus, 1993).....	6
Figure 1-3. Top sand AVO responses on the crossplot (after Castagna et al., 1998). .....	9
Figure 2-1. Raypaths describing the propagation of direct arrival (downgoing) and upgoing energy (after Lines and Newrick, 2004, and Hardage, 1983). .....	13
Figure 2-2. Schematic diagram of corridor mute and stack of zero-offset VSP shot (after Hinds et al., 1989). .....	14
Figure 2-3. Schematic illustration of coordinate system of x, y, and z components at the local receiver depth along with the coordinate axis after rotation (after Hinds et al., 1989).....	15
Figure 2-4. Schematic diagram of time-variant polarization (after Hinds et al., 2007).....	16
Figure 2-5. Schematic diagram of VSP-CDP transform. Curve 1: stretching of shallowest receiver's trace; curve 2: stretching of deepest receiver trace (after Hinds and Kuzmiski, 2001). .....	18
Figure 2-6. Shot records at different offsets (vertical component). The far-offset shots don't show clear direct arrival and reflection waves.....	19
Figure 2-7. 3 component of a shot (offset is 153 m). Small receiver interval (2m) helped to record different wave modes.....	19
Figure 2-8. 3D geometry display of the VSP data. False X and Y coordinates are used in the figure due to confidentiality.....	20
Figure 2-9. Dynamite zero-offset shot vertical component: downgoing P (yellow), upgoing P (red) and downgoing shear (pink) waves (display with AGC window=200 ms). .....	21
Figure 2-10. Vibroseis shot 4 (offset=153 m) vertical component: downgoing P (yellow), upgoing P (red), downgoing S (pink), and upgoing S (green, reflected shear) waves (display with AGC window=200 ms). .....	22
Figure 2-11. Vibroseis shot 4 (offset=153m) Hmax component. Different wave types were marked by color lines (display with AGC window=200 ms). Downgoing P was marked by a yellow line, downgoing SV (direct arrival) pink line, transmitted (downgoing) S blue line (converted from downgoing P), upgoing SV (converted from downgoing P) red line, and reflected SV wave (SS) the green line. ....	22

Figure 2-12. Zero-offset (left) and far-offset (right) VSP processing sequence.....	23
Figure 2-13. Velocity profile calculated from first arrival time of zero-offset VSP data. (a) First arrival picks, (b) calculated average velocities are in blue and interval velocities in red. ....	24
Figure 2-14. Raw vertical component of zero-offset shot before and after wavefield separation. (a) Raw shot; (b) separated upgoing waves; (c) downgoing waves were separated by a 19-trace median filter and displayed in -TT time (flattened on first arrivals). Red ellipses mark downgoing SV on separated upgoing wavefield and residual upgoing waves on the separated downgoing wavefield.....	25
Figure 2-15. (a) Downgoing P wave (-TT time) and its amplitude spectrum before deconvolution. (b) Downgoing P wave (-TT time) and its amplitude spectrum after deconvolution. Average spectrum is displayed as a blue curve, and the color traces are spectra of individual traces. ....	27
Figure 2-16. (a) Upgoing waves before deconvolution; (b) Upgoing waves after deconvolution. Both data displayed in -TT time. Red ellipses highlight the difference before and after deconvolution. After the deconvolution, events show higher resolution and better consistence. ....	28
Figure 2-17. (a) Upgoing waves after exponential gain; (b) with NMO correction; (c) applied statics shifting. Red ellipse highlights SV wave contaminations. ....	29
Figure 2-18. The processed upgoing P-wave gather with corridor mute (yellow dash line), 10 fold corridor and full stack. The reservoir zone is highlighted by the blue rectangle. The corridor stack shows better resolution than the full stack.....	30
Figure 2-19. The second hodogram analysis of Vibroseis shot 4. (a) The hodogram plot of a trace (channel=270, colored by time), black line shows the picked polarization; (b) two input components (Z and Hmax) and output components (Hmax' and Z'); (c) rotation angles of all the receivers in the current shot.....	31
Figure 2-20. Rotation of Z and Hmax into Hmax' and Z'. After rotation, Hmax' is dominated by downgoing P-wave and upgoing SV wave energy, and Z' is dominated by upgoing P-wave and downgoing SV wave energy. ....	32
Figure 2-21. Median filter test on a shot (offset=153 m). (a) Raw Z component, (b) downgoing wave separated by 11 trace filter, (c) downgoing wave separated by 15 trace filter, (d) downgoing wave separated by 19 trace filter respectively.....	33
Figure 2-22. (a) Hmaxdero component after derotation of Hmax' and Z' upgoing wavefield. (b) Zdero component after derotation. Hmaxdero is dominated by upgoing S-waves while Zdero is dominated by upgoing P-waves.....	34
Figure 2-23. Ray tracing (200 rays were used for demonstration, 2000 rays for actual processing) .....	35

Figure 2-24. Time-variant rotation results. (a) The component contains upgoing P-waves; (b) the component contains upgoing SV waves. Note that each component contains some downgoing waves.....	35
Figure 2-25. VSP-CDP stacked images of one shot example (offset =153 m). (a) Bin size=1 m, (b) bin size=2 m, and (c) bin size=3 m. ....	36
Figure 2-26. (a) VSP-CDP mapping of PP data and (b) VSP-CCP mapping of PS data. Both stacked images are merged traces from shot 1 to 6, offset from zero to 308 m, bin size=1 m. ....	37
Figure 3-1 Horizontal component of dynamite shot 4 before and after a 90 degree phase rotation. (a) Before phase correction, (b) after phase correction, the data have minimum phase. ....	38
Figure 3-2. Sonic log calibration: (a) time-depth curves, VSP one-way P-wave travel time in blue, sonic log calculated one-way P-wave time in red, (b) time drift between VSP and well log before calibration, (c) comparison of VSP (blue) and sonic log (red) interval velocities before calibration, (d) time drift after calibration, (e) comparison of VSP (blue) and sonic log (red) interval velocities after calibration. The original sonic logs are plotted in grey. ....	39
Figure 3-3. Input wavelet of synthetic seismogram and spectrum analysis of the VSP data. (a) The 60 Hz Ricker wavelet; (b) spectrum of the VSP data (P-wave). The Ricker wavelet and the VSP data have similar spectra. ....	40
Figure 3-4. Synthetic offset traces gather and stacked traces of the gather (3 fold). Red curves are the incident angles. The reservoir zone is highlighted by the yellow rectangle..	41
Figure 3-5. Composite plot of the sonic log, VSP data and synthetic seismogram. (a) Sonic log, (b) VSP-CDP mapping of an offset shot (offset=153 m), (c) processed upgoing P-wave gather of the zero-offset shot, (d) corridor stack and (e) full stack of the zero-offset shot, (f) synthetic offset seismic gather and it's stacked traces (3 fold). Dash lines highlight geological markers in this area. ....	42
Figure 3-6. A processed converted-wave gather flattened by estimated S-wave velocity. Flatten events indicate good estimation of S-wave velocities. ....	44
Figure 3-7 Prestack depth migration of P-wave (a) and converted-wave data (b). Poor tie of PP and PS images result from errors in shear-wave velocities and the small aperture of the VSP survey.....	46
Figure 3-8. Registration of PP (a) and PS data (b). PS data have been transformed to PP time. The yellow rectangle highlights the reservoir zone. ....	46
Figure 4-1. (a) Logs from the target reservoir. From left to right, the logs are gamma ray, sonic, density and neutron porosity respectively. (b) Resistivity logs from a nearby well. Red curve is the shallow induction resistivity log (10 inch) and black curve is the deep	

induction resistivity log (90 inch). Decreased resistivity around depth 485 m indicates oil water contact. ....	52
Figure 4-2. Statistical wavelet extracted from processed VSP data. ....	53
Figure 4-3. Correlation between VSP trace and synthetic seismogram. (a) P-wave, S-wave velocity and density logs, (b) synthetic traces (blue) and VSP traces (red) at well location, (c) VSP data. ....	54
Figure 4-4. Inversion analysis. From left to right, are impedance log, statistical wavelet, synthetic and seismic traces, and the error between synthetic and seismic. For the impedance logs, the blue curve is impedance from original P-wave velocity and density log, the black curve is the original model, and the red is impedance log from the inversion. ....	54
Figure 4-5. Inverted P-impedance. Reservoir is highlighted by the blue rectangle. ....	55
Figure 4-6. (a) Plots of $Z_s$ vs $Z_p$ and (b) density vs $Z_p$ on a log-log scale. The red lines indicate the current linear trend. ....	55
Figure 4-7. Prestack inversion analysis. (a) The inversion results (in red) $Z_p$ , $Z_s$ , Density, $V_p/V_s$ separately overlaying the original logs from the well (blue), black curves are original models; (b) statistic wavelet; (c) synthetic traces; (d) VSP angle gather; (e) errors between inverted synthetic and seismic. ....	56
Figure 4-8. (a) Inverted P-wave impedance and (b) S-wave impedance. Reservoir is highlighted by the blue rectangle. ....	57
Figure 4-9. S-impedance vs P-impedance crossplot. ....	58
Figure 4-10. (a) Inverted density and (b) $V_p/V_s$ . The reservoir is highlighted by the blue rectangle. ....	58
Figure 4-11. P-wave impedance vs $V_p/V_s$ crossplot. ....	59
Figure 4-12 Workflow to produce offset reflectivity gather for AVO analysis. ....	60
Figure 4-13. (a) Tie of synthetic offset gather (shown in black) and reflectivity gather (shown in red). Top and bottom of the target reservoir are picked and highlighted by blue lines. (b) AVO responses at top and base of the studied reservoir. Red lines are amplitudes from the VSP and blue lines are amplitudes from the synthetics seismogram. ....	61
Figure 4-14. Gradient curve. Dots curves are amplitudes measured from VSP gather and solid lines are amplitudes measured from synthetic seismogram. Red curve and dots are from the top of the reservoir and green curves and dots are from the bottom of the reservoir. ....	62

Figure 4-15. AVO attributes derived from the angle gather at the VSP well location from the two-term Aki-Richards method (angle gather is up to 42 degree). (a) Intercept A, (b) gradient B, (c) AVO product $A*B$ , (d) scaled Poisson's ratio change ( $aA+bB$ ), and (e) scaled S-wave reflectivity ( $aA-Bb$ ). Reservoir is highlighted by the yellow rectangle.....	62
Figure 4-16. (a) P-wave reflectivity $R_{p0}$ , (b) S-wave reflectivity $R_{s0}$ from two-term Fatti's method, and (c) derived fluid factor at $V_p/V_s=2.0$ . Reservoir is highlighted by the yellow rectangle.....	63
Figure 4-17. (a) Intercept A and (b) gradient B from Aki- Richards equation. The reservoir zone is highlighted by the yellow rectangle.....	64
Figure 4-18. A vs B crossplot. Small deviation from wet trend line ( $V_p/V_s=2.0$ ) indicates no gas anomaly. ....	64
Figure 4-19. (a) AVO product $A*B$ and (b) scaled Poisson's ratio change. The target reservoir is highlighted by a rectangle. ....	65
Figure 4-20. $R_p$ vs $R_s$ crossplot. Samples from the reservoir top show lower $R_p/R_s$ than the samples from the bottom of the reservoir. ....	66
Figure 4-21. (a) Inverted $Z_p$ and (b) $Z_s$ from $R_p$ and $R_s$ . The reservoir zone is highlighted by a rectangle. ....	66
Figure 4-22. Inverted $Z_p$ vs $Z_s$ crossplot. The top sand has higher $Z_p/Z_s$ than the bottom water sand. Inside the reservoir, sand samples show both low $Z_p$ and $Z_s$ . ....	67
Figure 4-23. (a) Angle gathers at CDP 35 to 41. Incident angles are from 0 to 42 degree. (b) Fluid factor ( $V_p/V_s=2.0$ ) inverted from the two-term Fatti equation. The reservoir is highlighted by a yellow rectangle. ....	67
Figure 4-24. (a) Inverted Lambda Rho and (b) Mu Rho. The reservoir is highlighted by a rectangle.....	68
Figure 4-25. Mu-rho vs Lambda-rho crossplot. Lithology and fluid changes in the target reservoir were identified through the LMR analysis. ....	69
Figure 4-26. Estimated logs from AVO modeling. (a) P-wave, (b) shear-wave, (c) density and (d) Poisson's ratio logs. The reservoir is highlighted by the blue color. ....	70
Figure 4-27. Comparison of synthetics created in different scenarios in AVO modeling and VSP gather. Reservoir zone is highlighted by the blue color. (a) Synthetic from pure gas, (b) 80% brine with 15% oil and 5% gas, (c) pure brine, (d) pure oil, and (e) VSP data. ....	70
Figure 4-28. Inverted (a) density, (b) $V_p/V_s$ , (c) $Z_p$ , (d) $Z_s$ from PP-PS joint inversion. The reservoir is highlighted by a rectangle. ....	72

Figure 4-29. (a) Crossplot of S-impedance vs P-impedance from PP-PS joint inversion. (b)  
Crossplot of S-impedance vs  $V_p/V_s$  inverted from PP-PS joint inversion..... 73

## List of Symbols, Abbreviations and Nomenclature

<b>Symbol</b>	<b>Definition</b>
VSP	Vertical seismic profile
SAGD	Steam assisted gravity drainage
AVO	Amplitude versus offset
PSDM	Pre-stack depth migration
3D	3 dimension
S/N	Signal to noise ratio
P-wave	Compressional wave
S-wave	Shear wave
PP	Downgoing p and upgoing p-wave
PS	Downgoing p and upgoing shear-wave(converted-wave)
SV wave	A shear wave that is polarized so that its particle motion and direction of propagation occur in a vertical plane
3C	3 component
m	Meter
MS	Millisecond
AGC	Automatic Gain Control
Hodogram	A crossplot of two components of particle motion over a time window
CDP	Common depth point
CCP	Common conversion point
$V_p$	P-wave velocity
$V_s$	Shear wave velocity
NMO	Normal moveout
F-K	Frequency-wavenumber domain
Q	Quality factor(attenuation)
E-GAIN	Exponential gain
$\lambda$	Lamé parameter
$\mu$	Shear modulus (rigidity)
$\rho$	Density
LMR	Lambda-mu-rho analysis
DAS	Distributed acoustic sensor

## **CHAPTER 1 INTRODUCTION**

### **1.1 Introduction**

In oil sands production, SAGD operations can be enhanced significantly by the accuracy of predictions of rock properties from a subsurface geological model. The need for a better understanding of the reservoir motivates geophysicists to improve the resolution of seismic and conduct more accurate time-depth conversion. A Vertical Seismic Profile (VSP) provides advantages in both. First, a VSP survey records reflections in both time and depth. Therefore, it is widely used to tie surface seismic data to subsurface geological features. In addition to that, due to its geometry, VSP data usually has better resolution and higher signal-to-noise ratio than surface seismic data. A VSP survey yields a more detailed image around the borehole than surface seismic data and provides accurate time-depth conversion; it has great potential for reservoir characterization and production monitoring.

In this study, a multicomponent walkaway VSP dataset was processed to image an oil sands reservoir and study the Amplitude Versus Offset (AVO) response and rock properties. This case study demonstrated that the multicomponent VSP is an effective tool to predict rock properties and fluid changes hence, consequently it can be applied to reservoir characterization and monitoring of SAGD operations.

### **1.2 Thesis objectives**

The principle goal of this thesis is imaging and studying the rock properties of the target heavy oil reservoir from a VSP experiment. To achieve the main goal, specific objectives are defined for this case study:

- Processing the multicomponent walkaway VSP data. Developing proper workflows and optimizing parameters in processing to preserve amplitudes of data for inversion and AVO analysis. Estimating shear-wave velocity, testing VSP pre-stack depth migration (PSDM).
- Creating synthetic seismograms and correlating to VSP data, and conducting PP-PS registration.
- Inverting rock properties of the target interval through post-stack, and pre-stack inversion, AVO attributes analysis and AVO modeling on P-wave reflections. Through crossplots of inverted rock properties, predicting lithology and fluid changes in the reservoir.

- Conducting PP-PS joint inversion, using converted-wave data to improve the accuracy of the predictions.

Through this work, I take advantage of the VSP survey to better characterize a heavy oil reservoir. The outcome of this study is a workflow that can be applied to other areas and, promote further technical development and application of VSP data in heavy oil reservoir characterization.

### **1.3 Theory and methodology**

In this study, VSP and converted-wave seismology, inversion and AVO techniques were employed. Fundamentals of these techniques are briefly introduced in this section.

#### *1.3.1 VSP seismology*

A vertical seismic profile (VSP) is a measurement in which seismic signal is generated at the surface of the earth but recorded by receivers secured in a borehole (Hardage, 1983). There are various types of VSPs as shown in Figure 1-1. The shot is close to the borehole in both a zero-offset VSP and a check-shot survey (Figure 1-1a). A zero-offset VSP records the entire wavefield while in a check-shot survey, receivers are spread sparsely down the borehole and the survey is designed to use first breaks only, mostly for calibrating some logs. Figure 1-1b shows an offset VSP survey in which the shot is at a significant distance from the borehole. A walkaway VSP (also known as a multi-offset VSP) consists of different offset VSPs (Figure 1-1c). Similarly, a multi-azimuth VSP contains many shots at different azimuths from the borehole. In addition to the types of VSPs discussed above, the receivers can be deployed in the horizontal portion of a well and the source arrays are arranged on the surface above. This is commonly known as a “walk-above” VSP (Figure 1-1d). A 3D VSP is a survey combined of multi-offset and multi-azimuth VSPs (Figure 1-1e). A 3D reverse VSP is acquired by locating the receivers at the surface and the sources within the borehole (Figure 1-1f). It has advantage of being conducted quickly, so it is more economical but one major concern is the possibility of damage to the borehole.

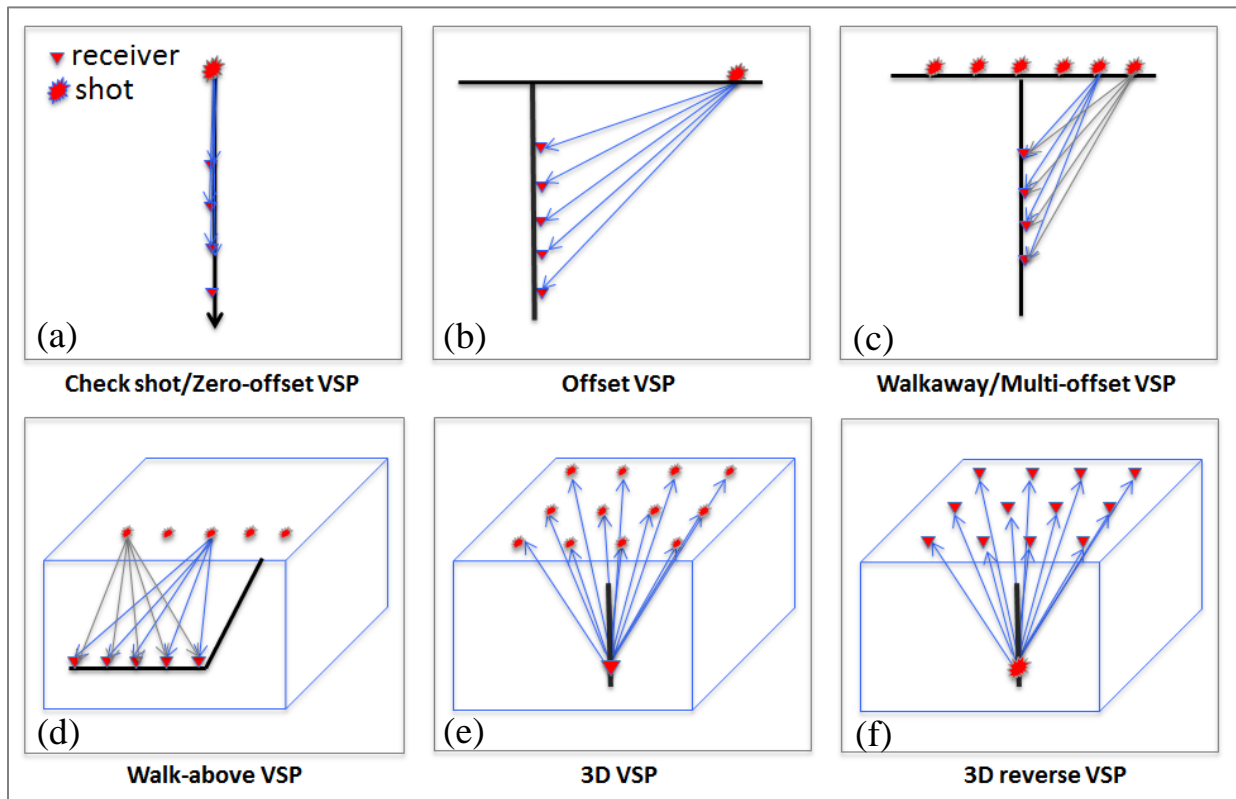


Figure 1-1. Different types of VSP geometry: (a) zero-offset VSP or check shot survey, (b) offset VSP, (c) walkaway VSP, (d) walk-above VSP, (e) 3D VSP, and (f) 3D reverse VSP (modified from Lines and Newrick, 2004).

Since a VSP survey records both time and receiver depth, it is used principally to calibrate the surface seismic data by giving an accurate depth-time tie to geological features. The VSP dataset has greater resolution than surface seismic because the seismic wave travels through attenuating near surface strata only once. It enables more detailed structural information to be obtained within the vicinity of the borehole. Although the image quality of a far offset VSP decreases quickly with increasing distance from the borehole, this drawback can be mitigated by walkaway VSP. Besides broader frequency bandwidth, VSP surveys have other advantages for AVO analysis (Coulombe et al., 1996): (1) VSP data have less noise interference due to the quiet borehole environment, where the S/N is higher than that of surface seismic data; (2) the downgoing wavefield is also recorded and can be used to design the deconvolution operator to better remove wavefield propagation effects such as multiples; (3) a VSP survey records both downgoing and upgoing waves, for the reflections close to their reflection points, it is relatively easy to obtain the reflection coefficients through dividing the upgoing wave amplitude by

downgoing wave amplitude; (4) the walkaway VSP survey is ideal for AVO analysis. Considering all these advantages, the walkaway VSP is especially suited for reservoir characterization.

### 1.3.2 *Converted wave seismology*

Since the cost of three component (3C) acquisition has reduced in recent years and multicomponent seismic data are now recorded in VSP surveys. The 3C data capture the seismic wave field more completely than traditional single-element techniques (Stewart, et al., 2002). The application of P-S (converted seismic wave, downgoing reflection P-waves convert to upcoming S-waves) enhances the traditional compressional wave exploration in many aspects, such as structural imaging, lithology estimation, anisotropic analysis, and subsurface fluid analysis. The benefits of converted-wave data in exploration have led to the development of processing and interpretation techniques in the industry. Although some key techniques in converted-wave data processing were applied in production and produced satisfactory result, the asymmetric ray path of converted-waves still cause problems in data processing. Converted-wave data processing needs specific techniques, including 3C data rotation, common conversion point (CCP) binning, and PS migration. VSP data analyzed for this thesis were recorded with 3C geophones.

### 1.3.3 *Inversion principles*

Inversion is a procedure for obtaining models which adequately describe a data set. In the case of geophysical data, inversion seeks to determine the rock properties and define a geologic model, which agrees with the geophysical observations.

It has been assumed that the seismic data equals wavelet convolved with reflectivity plus noise:

$$S=W*R+Noise \tag{1-1}$$

where S is the seismic data, W is the wavelet and R is the reflectivity. Therefore, we can derive reflectivity from the Equation (1-1). Since the acoustic impedance ( $Z_{pi}$ ) and zero-offset reflection coefficient of ith layer ( $R_{pi}$ ) are defined as:

$$Z_{pi} = \rho * V_{pi} \tag{1-2}$$

$$R_{pi} = \frac{Z_{i+1} - Z_i}{Z_{i+1} + Z_i} = \frac{1}{2} \frac{\Delta Z}{Z} \approx \frac{1}{2} \Delta \ln(Z) \quad (1-3)$$

where  $\rho$  is the density and  $Z_i$  is the impedance of the  $i$ th layer.

In a simple layered model, from Equation (1-1), (1-2) and (1-3), we can derive the impedance of a layer from the reflection coefficients and the impedance of the layer directly above it. However, band-limited and noisy seismic data makes this procedure nontrivial. Another pitfall of inversion is there are more than one possible geological models consistent with the seismic data. The way to choose among the possibilities is to combine other information other than seismic data such as initial guess model and constrains.

#### 1.3.4 AVO principles

Analysis of Amplitude Variation with Offset (AVO) is used to derive petrophysical properties within the depositional unit associated with the reservoir rocks (Yilmaz, 2001). When seismic waves travel in the earth and encounter layer boundaries having velocity and density contrasts, the energy of any incident wave is partitioned. The fraction of incident energy that is reflected depends on the angle of incidence. Analysis of reflection amplitudes as a function of incidence angle can be used to detect changes in elastic properties of reservoir rocks, and which may suggest the change in the ratio of P-wave velocity to S-wave velocity. The change of  $V_p/V_s$  can be an indicator of fluid saturation changes within the reservoir rocks. The fundamental value of AVO analysis is the fact that seismic amplitudes at the boundaries are affected by the variations of the physical properties just above and just below the reflectivity boundaries.

When a plane P-wave strikes an interface, some fraction of the incident P-wave is partially converted to an S-wave at the interface, and the reflection coefficients become a function of  $V_p$ ,  $V_s$  and density of each layer, as shown in Figure 1-2. The relationship of incident, reflected and transmitted rays at the boundary are described by Snell's law:

$$p = \frac{\sin \theta_1}{V_{P1}} = \frac{\sin \theta_2}{V_{P2}} = \frac{\sin \phi_1}{V_{S1}} = \frac{\sin \phi_2}{V_{S2}} \quad (1-4)$$

In this equation,  $\theta_1$  is the angle of the incident P-wave, it equals the reflection angle of the P-wave,  $\phi_1$  is the angles of reflection S-wave in medium 1. The angle  $\theta_2$  and  $\phi_2$  are the

transmission angles of the P- and S-waves in medium 2. The velocities of medium 1 are  $V_{P1}$  and  $V_{S1}$ , while the velocities of medium 2 are  $V_{P2}$  and  $V_{S2}$ .

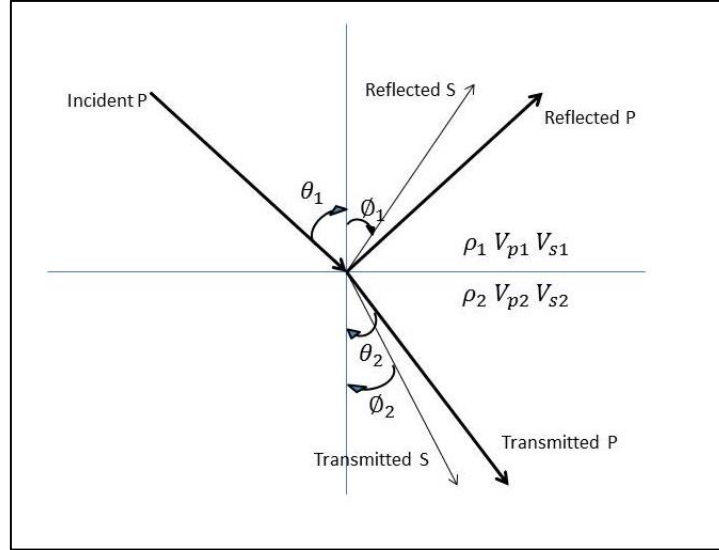


Figure 1-2. Reflection and transmission at an interface between two infinite elastic half-spaces for an incident P-wave (after Castagna and Backus, 1993)

Zoeppritz equations (1919) give the reflection and transmission coefficients for plane waves as a function of angle of incidence and six independent elastic parameters  $V_P$  and  $V_S$  and  $\rho$ , three on each side of the reflecting interface (Shuey, 1985). The equations are listed as follows:

$$\begin{bmatrix} R_P(\theta_1) \\ R_S(\theta_1) \\ T_P(\theta_1) \\ T_S(\theta_1) \end{bmatrix} = \begin{bmatrix} -\sin \theta_1 & -\cos \phi_1 & \sin \theta_2 & \cos \phi_2 \\ \cos \theta_1 & -\sin \phi_1 & \cos \theta_2 & -\sin \phi_2 \\ \sin 2\theta_1 & \frac{V_{P1}}{V_{S1}} \cos 2\phi_1 & \frac{\rho_2 V_{S2}^2 V_{P1}}{\rho_1 V_{S1}^2 V_{P2}} \cos 2\phi_1 & \frac{\rho_2 V_{S2} V_{P1}}{\rho_1 V_{S1}^2} \cos 2\phi_2 \\ -\cos 2\phi_1 & \frac{V_{S1}}{V_{P1}} \sin 2\phi_1 & \frac{\rho_2 V_{P2}}{\rho_1 V_{P1}} \cos 2\phi_2 & -\frac{\rho_2 V_{S2}}{\rho_1 V_{P1}} \sin 2\phi_2 \end{bmatrix}^{-1} \begin{bmatrix} \sin \theta_1 \\ \cos \theta_1 \\ \sin 2\theta_1 \\ \cos 2\phi_1 \end{bmatrix} \quad (1-5)$$

where  $R_P$ ,  $R_S$ ,  $T_P$ , and  $T_S$ , are the reflected P, reflected S, transmitted P, and transmitted S-wave amplitude coefficients respectively.

The zero angle reflection and transmission coefficients are:

$$R_S(0^0) = T_S(0^0) = 0, \quad R_P(0^0) = \frac{\rho_2 V_{P2} - \rho_1 V_{P1}}{\rho_2 V_{P2} + \rho_1 V_{P1}}, \quad T_P(0^0) = \frac{2\rho_1 V_{P1}}{\rho_2 V_{P2} + \rho_1 V_{P1}} = 1 - R_P(0^0) \quad (1-6)$$

Aki-Richards (1980) gave a linearized approximation to the Zoeppritz equations. The initial form separated the velocity and density terms. In practice, these equations are quite complex and are not generally used directly in seismic data analysis. Many approximations to Zoeppritz's equations allow AVO analysis to be applied without difficulty. A few approximations are introduced as follows:

The Aki and Richards (1980) approximation is given by:

$$R_p(\theta) \approx \frac{1}{2}(1 - 4V_s^2 p^2) \frac{\Delta\rho}{\rho} + \frac{1}{2 \cos^2 \theta} \frac{\Delta V_p}{V_p} - 4V_s^2 p^2 \frac{\Delta V_s}{V_s} \quad (1-7)$$

where  $R_p$  is offset dependent reflectivity,  $\Delta V_p = (V_{p2} - V_{p1})$ ,  $V_p = \frac{V_{p2} + V_{p1}}{2}$ ,  $\Delta V_s = (V_{s2} - V_{s1})$ ,  $V_s = \frac{V_{s2} + V_{s1}}{2}$ ,  $\Delta\rho = (\rho_2 - \rho_1)/2$ ,  $\rho = (\rho_1 + \rho_2)/2$ ,  $p$  is the raypath parameter and  $\theta$  is the average angle of the incident and transmitted P-wave angles.

The Aki and Richards approximation has following assumptions: (1) small relative changes in physical properties, (2) higher than second - order terms can be neglected, and (3) the incident angle does not approach the critical angle.

Wiggins et al. (1983) reformulated the form of the Aki-Richards equation. The equation was separated into three reflection terms, each weaker than the previous term:

$$R_p(\theta) = A + B \sin^2 \theta + C \tan^2 \theta \sin^2 \theta \quad (1-8)$$

where

$$A = \frac{1}{2} \left[ \frac{\Delta V_p}{V_p} + \frac{\Delta\rho}{\rho} \right], B = \frac{1}{2} \frac{\Delta V_p}{V_p} - 4 \left[ \frac{V_s}{V_p} \right]^2 \frac{\Delta V_s}{V_s} - 2 \left[ \frac{V_s}{V_p} \right]^2 \frac{\Delta\rho}{\rho}, C = \frac{1}{2} \frac{\Delta V_p}{V_p}$$

A is called the intercept, B the gradient, and C the curvature.

Shuey (1985) gave a further approximation of Zoeppritz equations. It is commonly used in AVO analysis because it gives a relatively simple relationship between rock properties (Poisson's ratio) and the variation in reflection coefficients. In addition to that, it expresses the reflection coefficient as a sum of three terms containing a normal-angle term, a near-angle term and a far-angle term.

$$R_p(\theta) \approx R_0 + \left[ A_0 R_0 + \frac{\Delta\sigma}{(1-\sigma)^2} \right] \sin^2 \theta + \frac{1}{2} \frac{\Delta V_p}{V_p} (\tan^2 \theta - \sin^2 \theta) \quad (1-9)$$

$R_0$  is the normal-incidence P-P reflection coefficient or “intercept”, and  $A_0$  is given by

$$A_0 = B_0 - 2(1 + B_0) \frac{1 - 2\sigma}{1 - \sigma} \quad (1-10)$$

and

$$B_0 = \frac{\Delta V_p / V_p}{\Delta V_p / V_p + \Delta \rho / \rho} \quad (1-11)$$

where  $\Delta\sigma = \sigma_2 - \sigma_1$  and  $\sigma = (\sigma_1 + \sigma_2)/2$

Hilterman (1989) simplified Shuey’s approximation by assuming that  $\frac{V_s}{V_p} = 0.5$  or  $\sigma = 0.33$  and  $\tan^2 \theta \cong \sin^2 \theta$ . Hilterman’s equation is given by

$$R_p(\theta) = R_0 \cos^2 \theta + \left[ \frac{\Delta\sigma}{(1-\sigma)^2} \right] \sin^2 \theta = R_0 \cos^2 \theta + 2.25 \Delta\sigma \sin^2 \theta \quad (1-12)$$

where  $R_0$  is normal-incidence reflection coefficient,  $\Delta\sigma$  is the difference of Poisson’s ratio between the lower and upper media, and the  $\theta$  is the angle of incidence. The  $[\Delta\sigma/(1 - \sigma^2)]$  is Poisson reflectivity (PR). The “normal - incidence” and “Poisson - reflectivity” terms in this equation can be used to predict lithology (Hilterman, 1989).

$V_p/V_s=2$  is a convenient approximation. The number has geological, physical and mathematical meanings. Geologically,  $V_p/V_s$  related to lithology and many of the lithologies show  $V_p/V_s$  is between 1.5 to 3.5. Physically, the  $V_p/V_s=2$  is connected the  $\sigma=0.3$ . In general, the Poisson’s ratios of sand and shale are around 0.2-0.45. Mathematically, the number can simplify the Shuey equation and make it easier to apply to real data studies.

AVO classes, as published, describe AVO responses only for single interface (e.g. Simm and Bacon, 2014). The classification works well for thick-bedded sand settings and becomes less useful in reservoir sections with multiple thin beds. Rutherford and Williams (1989) derived the following classification scheme for AVO anomalies, with further modifications by Ross and Kinman (1995) and Castagna (1997): Class 1: High impedance sand with decreasing AVO; Class 2: Near-zero impedance contrast; Class 2p: Same as 2, with polarity change; Class 3: Low impedance sand with increasing AVO; Class 4: Low impedance sand with decreasing AVO. The

classification is listed in Table 1-1 and the distribution of AVO anomalies on a Gradient-Intercept crossplot system is shown in Figure 1-3.

Coulombe et al. (1996) used VSP measurements to analyze AVO effects in carbonate strata. Their study showed that PP and PS AVO effects were in evidence and could be modeled. In this work, I will use 3C VSP data to examine AVO responses in a sand-shale sequence within a heavy oil reservoir.

Table 1-1. AVO classification

	Impedance compare to encasing shale	Amplitude vs offset
CLASS I	Higher impedance	Reduce
CLASS II	Similar but lower	Increase
CLASS IIp	Similar but higher	Increase
CLASS III	Lower	Increase
CLASS IV	Lower	Decrease

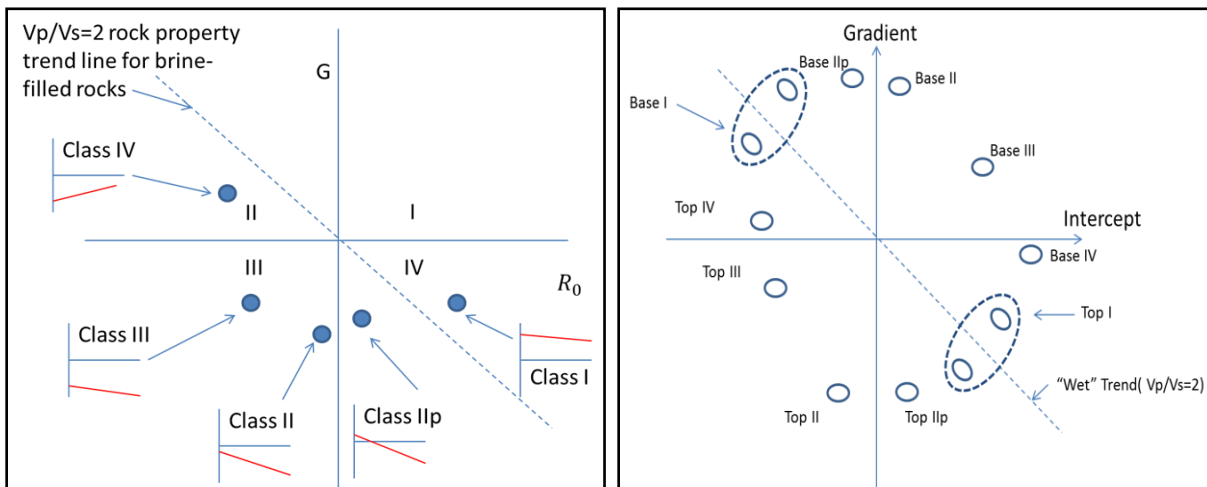


Figure 1-3. Top sand AVO responses on the crossplot (after Castagna et al., 1998).

## 1.4 Data used

In this study, a multicomponent walkaway VSP dataset from a heavy oil reservoir in Canada was used. The study area is currently under production by an anonymous company. CREWES

participated in the 2011 data acquisition. Two wells (A and B) close to the VSP borehole had log data that were used in creation of synthetic seismogram and for constraining inversions.

### **1.5 Hardware and software used**

The VSP seismic data were processed on VISTA processing system provided by GEDCO/Schlumberger. The synthetic seismogram was created by CREWES tool Syngram. Inversion and AVO analysis were conducted on Hampson-Russell software provided by Hampson-Russell/CGG.

## CHAPTER 2 DATA PROCESSING

### 2.1 Introduction

In a VSP survey, receivers are spaced down the borehole. This geometry produces a VSP wavefield different from that of a conventional seismic survey. Accordingly, special techniques are used in VSP data processing. Since a VSP survey records both downgoing and upgoing energy, separating the downgoing and upgoing wavefields, and identifying the primary events, are the most important steps in VSP processing. The downgoing wave of a VSP survey carries the source signature, which can be used to estimate the deconvolution operator and estimate the amplitude scalar. In this chapter, the major processing techniques of zero and offset VSPs will be discussed in detail. Then the processing of the data acquired from the study area introduced.

### 2.2 Processing techniques

#### 2.2.1 *Processing techniques of zero-offset shot*

For the zero-offset VSP shot, the major processing steps include first break picking, velocity computation, upgoing and downgoing wavefield separation, deconvolution, NMO, statics correction, and finally, the corridor stack.

#### First arrival picking and velocity computation

In practice, in order to minimize the picking errors, first arrivals are picked on a peak, trough or the zero-crossing. Based on the raw data, generally, the first arrivals are picked on raw data peaks for Vibroseis data and on troughs for dynamite data. Then the interval velocity is calculated, based on the picked times. Any picks causing anomalous velocity need to be corrected or deleted. If well logs are available, the sonic logs can be used to guide the velocity computation.

Offset VSP shots will use the calculated interval velocities to apply NMO corrections as well as ray tracing for time-variant polarization.

#### Upgoing and downgoing wavefield separation

Both downgoing and upgoing wavefields are recorded and the different wave types are separated by filtering. Many methods can serve this purpose. In this project, median filtering and Fourier wavenumber transform (F-K filtering) were applied.

Median filtering removes non-similar data within a window by sorting data according to size, and outputting the median (center) value. When the downgoing events are aligned, upgoing events will show up-to-the-right stepout. A median filter smoothed and accentuated the flattened downgoing events since the wave shapes remain reasonably constant. When the median filter passes through a non-horizontal event, the filter rejects the dipping events since that wave mode does not exhibit a uniform horizontal phase alignment. Then the trace window slides at constant time, the downgoing wavefields are accurately estimated, and the upgoing reflections can be acquired by subtracting the estimated downgoing events from the raw data. Median filters have the advantages of preserving edges and data characters.

In the time domain, upgoing and downgoing events always criss-cross one other, but they do not overlap in the frequency-wave number (F-K) domain. Raw data show a pie slice of energy in F-K domain. The flattened data show a narrow band along the  $K=0$  axis while other energy aliases between the wavenumber and frequency axes. It is easy to remove the artifacts by defining one or more polygons or fan zones, and zeroing them out. This separation of VSP modes in F-K space provides a convenient mean by which downgoing events can be attenuated without suppressing upgoing events. Upgoing events can be acquired by subtracting the downgoing waves from flattened raw data.

#### VSP deconvolution

The purpose of deconvolution is to remove the effect of the source wavelet to obtain a seismic reflectivity series which is generally considered to be white (Margrave, 2008). Since the downgoing direct wave represents the source signature, it is used to design the deconvolution operator. Another advantage of using the downgoing first arrival events to calculate the deconvolution operator is that the operator is determined from a wavefield whose signal/noise is greater than that of the usual case. The calculation is therefore based on the best possible description of the wide range of relationships that exist in the stratigraphic section near the VSP well, and where the influence of noise on the calculation is minimized. The operator thus obtained is applied to isolate upgoing waves.

#### NMO and statics correction

Since a VSP is not recorded in two-way traveltime, statics need to be applied to shift VSP data to two-way traveltime so as to be the same as surface seismic surveys. The downgoing and

upgoing raypaths recorded at geophone are shown in Figure 2-1. The true rays are vertical but they are shown as inclination (offset) in order to be seen in the figure. Following the nomenclature of Hardage (1983),  $T_a$ ,  $T_b$ , and  $T_g$  are the one-way vertical traveltimes to horizon A, horizon B, and the geophone. From Figure 2-1, the expressions for arrival times at the geophone for upgoing reflection A, B and multiple M are:

$$\tau_a = T_a + (T_a - T_g) = 2T_a - T_g \quad (2-1)$$

$$\tau_b = T_b + (T_b - T_g) = 2T_b - T_g \quad (2-2)$$

$$\tau_m = T_a + (T_a - T_g) + 2(T_a - T_b) = 2T_a + 2(T_a - T_b) - T_g \quad (2-3)$$

The form of each of these equations is the two-way traveltime of an event at the surface minus the one-way traveltime to the geophone (Lines and Newrick, 2004). Therefore, if the one-way traveltime to the geophone ( $T_g$ ) is added to each trace, the plot of record traces is referred to as a +TT plot and is comparable to surface seismic data. Conversely, for the downgoing wave (red ray in Figure 2-1), if the one-way traveltime to the geophone ( $T_g$ ) is subtracted for each trace, the plot of seismic, is flattened by first arrival time and is referred to as a -TT plot.

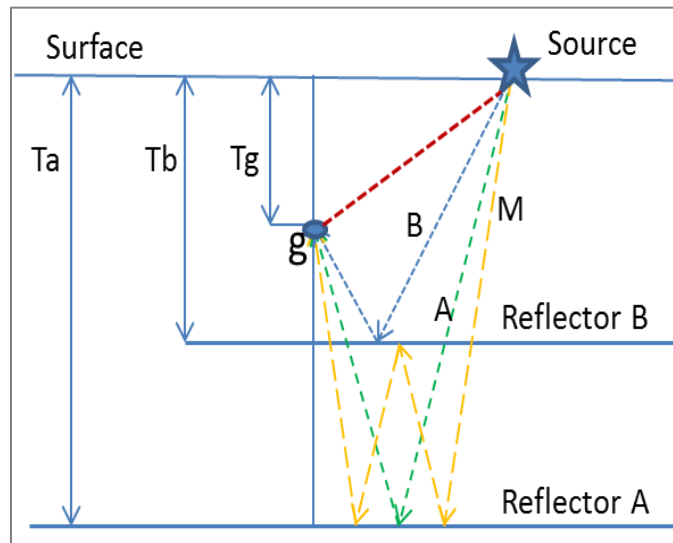


Figure 2-1. Raypaths describing the propagation of direct arrival (downgoing) and upgoing energy (after Lines and Newrick, 2004, and Hardage, 1983).

### Corridor mute and stack

In VSP data, the multiples mimic primaries but contain a time delay (Lines and Newrick, 2004), so multiple events can be identified as that they do not intersect the first breaks. If a mute

is applied to keep the primaries only outside the corridor line, a stack is obtained without any multiples. Following nomenclature of Hinds' (2007), it is called outside-corridor stack. On the other hand, the inside-corridor stack contains both primaries and multiples which can be used to determine the primary and multiples in surface seismic data. The schematic diagram of corridor mute and stack of zero-offset VSP is shown in Figure 2-2. Also, it is possible to get the stack of multiples only by subtracting the outside-corridor stack from inside-corridor stack.

In practice, before generating the corridor stack, preprocessing of the data is needed. An exponential gain is applied to correct the spherical spreading and transmission losses. Then NMO corrections are done by using the interval velocities calculated from zero-offset vertical component. After NMO, the data are converted to two-way traveltimes by adding the first arrival time. A F-K and a band-pass's filter are finally applied to the corrected data to enhance the signal to noise ratio before creating the corridor stack.

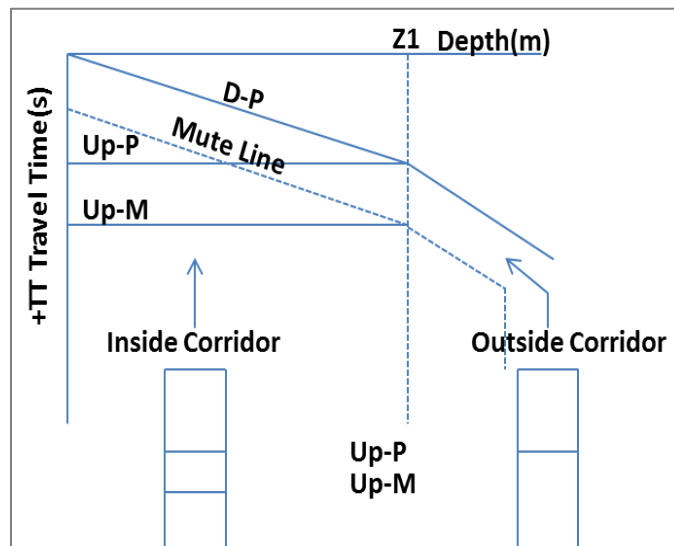


Figure 2-2. Schematic diagram of corridor mute and stack of zero-offset VSP shot (after Hinds et al., 1989).

### 2.2.2 Processing techniques of offset shots

Due to its geometry, offset VSP processing is more complicated than zero-offset VSP processing. Two hodogram-based rotations are implemented, the wavefields separation is then done on the rotated data. The downgoing P-waves are isolated to design the deconvolution operator while the upgoing waves go into a time-variant wavefield separation which isolates

reflected P, and S-waves based on the velocity model. Finally, a VSP-CDP mapping provides the image of subsurface reflections. These techniques will in the following section.

Far-offset VSP geometry and horizontal rotation

Since the sonde rotates in the borehole, which causes “spin” of the X and Y channels, two rotations are required for optimizing far-offset VSP processing through hodogram analysis. An assumption in the analysis is that the downgoing waves are perpendicular to the upgoing waves. In this thesis, all the different components before and after rotation are named following the processing software’s (VISTA) nomenclature. The first rotation is between two horizontal components, it is polarization of the X and Y data into Hmax and Hmin. The Hmax is the projection of X and Y into a plane defined by the well and source while the Hmin is normal to it. The second rotation is in the plane of the well and source using the horizontal component from the first rotation (Hmax) and vertical component (Z). It outputs one component polarizes along the source and receiver direction (Hmax’) and the other component polarizes perpendicular to it (Z’). After the second rotation, the Hmax’ component contains predominately downgoing P-wave energy along with upgoing SV while the downgoing SV is maximized on the Z’. Then the downgoing P will be separated from the Hmax’ component and be used to estimate deconvolution operator. Figure 2-3 schematically shows rotations between different axes. Both rotations are time-invariant and completed by hodogram analysis trace by trace.

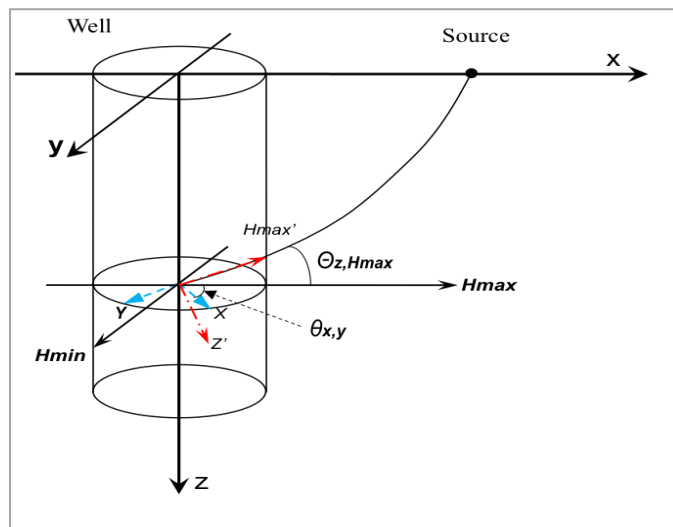


Figure 2-3. Schematic illustration of coordinate system of x, y, and z components at the local receiver depth along with the coordinate axis after rotation (after Hinds et al., 1989).

### Time-variant wavefield separation

As discussed above, wavefield separation of far-offset VSP is complicated due to its asymmetric ray path. Figure 2-4 shows that the incident angles decreases slowly with increasing depth below the geophones, and thus, the polarization angles change with time. So time-variant polarization analysis is required to achieve wavefield separation for far-offset VSP data. In practice, after two rotations, the time-invariant wavefield separation is firstly applied on Hmax' and Z' components to isolate an Hmax'up and Z'up by F-K or median filter. Then the inverse operation of the second rotation is applied on Hmax'up and Z'up to output the Hmaxup (derot) and Zup (derot). These derotated upgoing waves are the input of time-variant model based polarization. Using the velocity model obtained by ray tracing inversion from zero-offset VSP, the time-variant polarization calculates traveltimes and rotation angle trace by trace and output Z''up and Hmax''up. The Z''up is dominantly reflected P wave data and the Hmax''up is dominantly reflected shear wave modes. Both reflections can be used for interpretation.

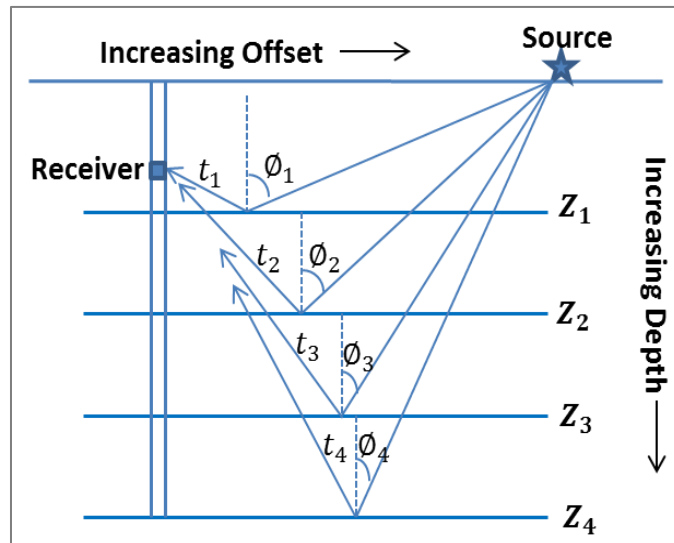


Figure 2-4. Schematic diagram of time-variant polarization (after Hinds et al., 2007)

### Deconvolution of upgoing P-wave data

Similar to zero-offset VSP processing, the deconvolution operator is obtained from the downgoing P-wave which is isolated from Hmax'. Then the operator is applied to upgoing P (Z''up) and upgoing S data (Hmax''up) which are derived from time-variant polarization

analysis. The far-offset VSP deconvolution will not be discussed in detail because the technique has been introduced in the zero-offset processing section.

#### VSP-CDP transform of upgoing P-wave data

VSP-CDP mapping is the most widely accepted method for offset VSP data imaging because it is based on velocity model of the structure that may incorporate information from other sources, for example, well logs and surface seismic data (Wiggins et al., 1986). The transformation is also useful because it requires relatively little computation.

Since the seismic source is off known distance from the borehole, the reflected waves received at the geophone originate from that reflection points are laterally offset from the borehole. In order to interpret this information, the reflection events must be placed in proper time and space positions. The VSP-CDP transform can serve this purpose. With the knowledge of the velocity field, VSP-CDP mapping can transform the VSP traces into their common reflection point positions on corresponding interfaces. The mapping is achieved by two major steps (shown in Figure 2-5):

- Find corresponding space and time position for each time sample  $T$  of the input traces by ray tracing.
- Assign each time sample  $T$  of the input traces to its proper time and spacial position which is commonly known as trace bending. The resulting traces are dynamically stretched in the 2D CDP-time domain, commonly called “bent traces”. After this processing, a bin interval is defined and all traces in the same bin are stacked.

The processing image is a map of reflectors. The VSP-CDP method provides both an offset-time or an offset-depth image then can be used for interpretation. In practice, processing is applied on the data before VSP-CDP mapping which includes spherical divergence correction, NMO and statics, median filtering and band-pass filtering.

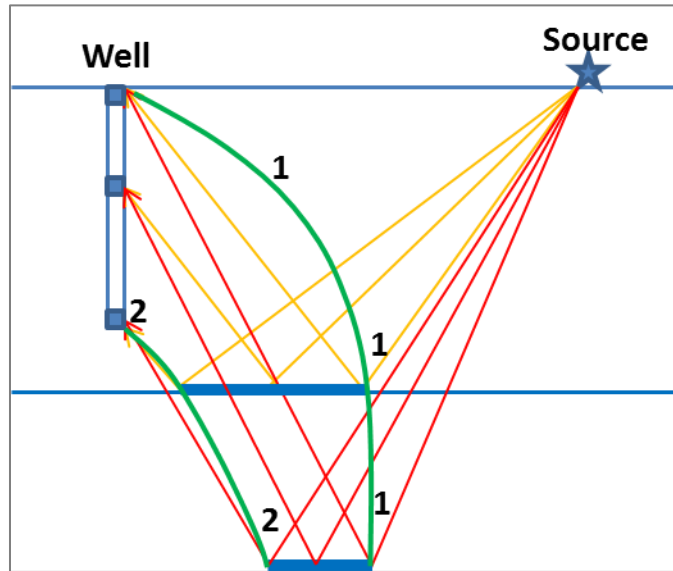


Figure 2-5. Schematic diagram of VSP-CDP transform. Curve 1: stretching of shallowest receiver's trace; curve 2: stretching of deepest receiver trace (after Hinds and Kuzmiski, 2001).

## 2.3 Field data processing

### 2.3.1 Acquisition parameters and raw shot records

The dataset used in this study is a walkaway vertical seismic profile (VSP) dataset acquired by CREWES in 2011. Both dynamite and the University of Calgary EnviroVibe were used as sources in this survey. The main acquisition parameters are shown in Table 2-1.

Table 2-1. Main parameters in walkaway VSP acquisition

	<b>Dynamite</b>	<b>Vibroseis</b>
<b>Charge (kg)/ Sweep</b>	0.125kg at 9m	10-300Hz over 20s
<b>Number of Shots</b>	14	14
<b>Receivers type</b>	VectorSeis	VectorSeis
<b>Number of receivers</b>	220	220
<b>Receiver spacing(m)</b>	2	2
<b>Receiver depth (m)</b>	55-507	55-507
<b>Sample rate (ms)</b>	1	1
<b>Record length (s)</b>	3	3
<b>Offset (m)</b>	11.5-1031	11.5-1031
<b>Source elevation (m)</b>	612-622	612-622
<b>Borehole</b>	562 m TD, Vertical, no fluids in borehole	

Figure 2-6 shows the vertical component of 5 shots at different offsets. Shot number and offset are shown on the top of the figure. Small offset shots show clear direct arrivals and strong reflections. The first arrival and reflections of large offset shots are interfered by other waves. Figure 2-7 shows 3 component of a shot (offset is 153m). Different wave types can be identified from the data. Small receiver interval (2m) in acquisition helped to record different wave modes.

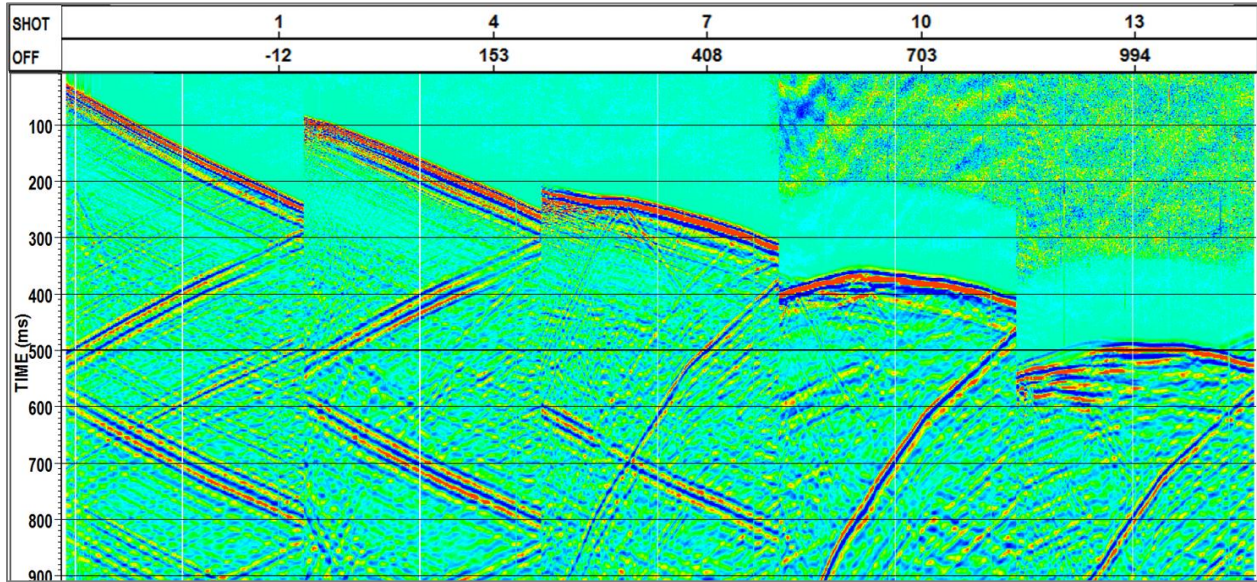


Figure 2-6. Shot records at different offsets (vertical component). The far-offset shots don't show clear direct arrival and reflection waves.

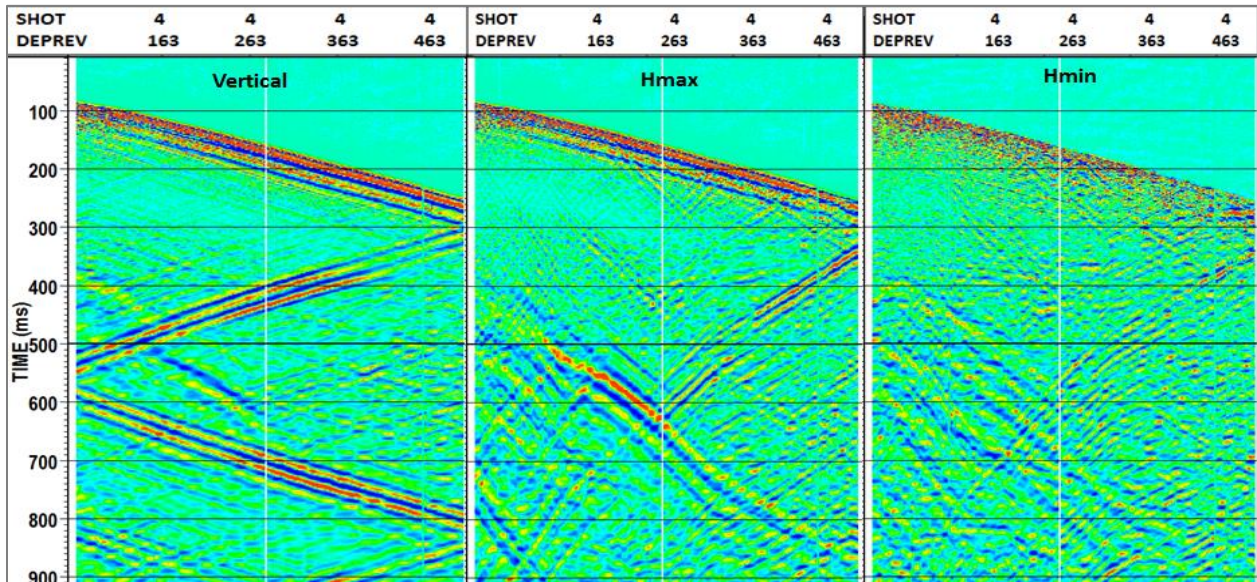


Figure 2-7. 3 component of a shot (offset is 153 m). Small receiver interval (2m) helped to record different wave modes.

### 2.3.2 Geometry setup and pre-processing of the VSP data

The zero-offset and far-offset shots were processed to corridor stack and VSP-CDP/CCP mapping stage separately. All the processing techniques discussed above were applied as follows.

Setting up VSP headers and geometry was the first step in processing. The TVD (total vertical depth) was calculated from measured receiver depth and datum or KB (kelly bushing) elevation. In this case, 620 m was used as elevation datum. The geometry of this walkaway VSP's survey was shown in Figure 2-8. The X and Y coordinates on the map are edited due to confidentiality. There were 14 shots recorded in both vibrator and dynamite surveys and each shot was processed separately. The first arrival was picked on vertical component (Z) and the picking values were transferred to the X and Y components. Some traces with abnormal amplitudes were killed and reverse polarity traces were corrected as well.

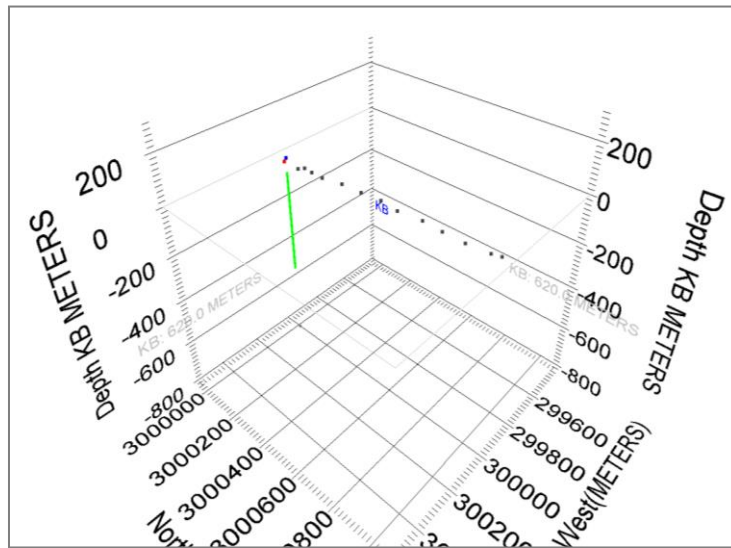


Figure 2-8. 3D geometry display of the VSP data. False X and Y coordinates are used in the figure due to confidentiality.

An example of the vertical component of the dynamite zero-offset shot is shown in Figure 2-9. Downgoing P (yellow), upgoing P (red) and downgoing S (pink) are identified on the raw record. Similar wave types are shown by the vertical component of a far-offset (153 m) shot (Figure 2-10). The figure shows a shot using the vibrator source which recorded stronger S-wave modes than the dynamite shots. It is noteworthy that the S-wave is much stronger on the far-offset shot than on the zero-offset shot due to the larger incident angle change.

During VSP data acquisition, the orientation of horizontal components especially will change from one receiver to another due to tool spin. For multicomponent VSP processing, horizontal rotation is required to correct these twirls. The original record X and Y were rotated to Hmax and Hmin. This rotation maximized energy on Hmax while minimized the energy on Hmin component. Figure 2-11 shows the Hmax component of the vibroseis shot4 (offset=153 m) after horizontal rotation. Comparing to the vertical component, the wavefield on Hmax component as shown is more complex. The yellow line marked downgoing P, pink line marked direct arrival of downgoing SV and blue line marked the converted S from downgoing P. The upgoing SV (converted PS) was marked by red line and the reflected SV wave (SS) was marked by green line. The wave types make the following wavefield separation difficult.

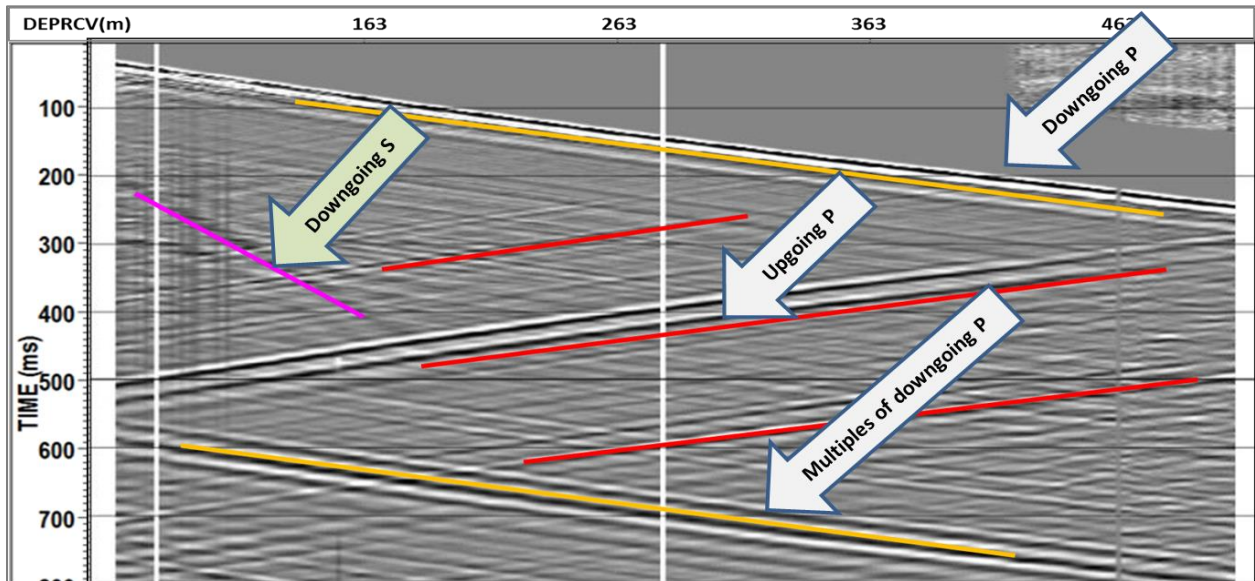


Figure 2-9. Dynamite zero-offset shot vertical component: downgoing P (yellow), upgoing P (red) and downgoing shear (pink) waves (display with AGC window=200 ms).

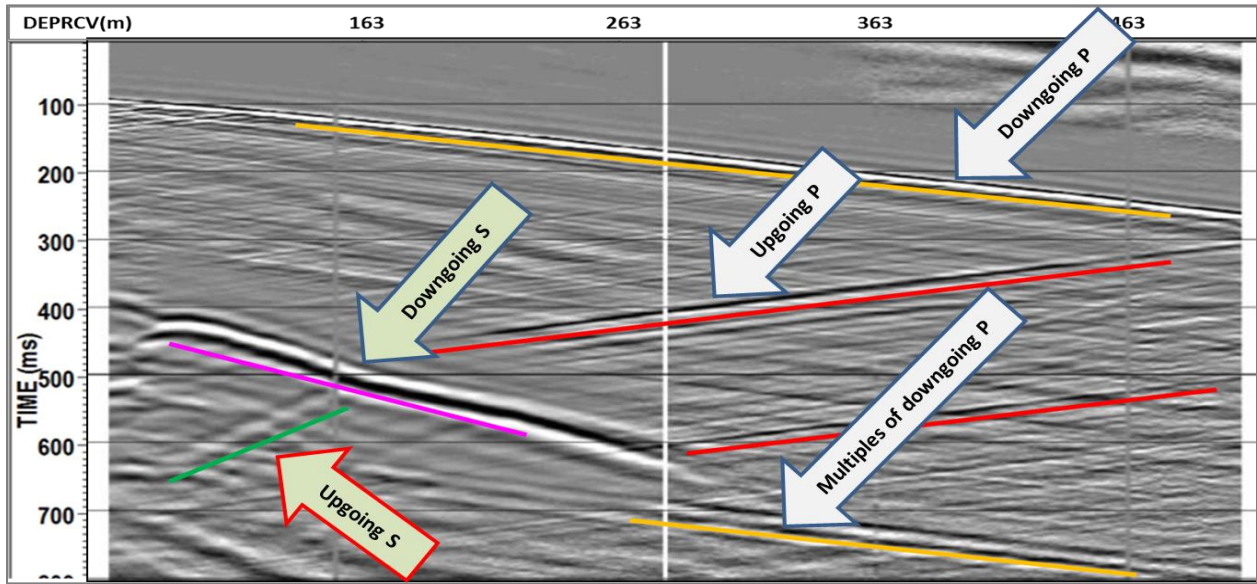


Figure 2-10. Vibroseis shot 4 (offset=153 m) vertical component: downgoing P (yellow), upgoing P (red), downgoing S (pink), and upgoing S (green, reflected shear) waves (display with AGC window=200 ms).

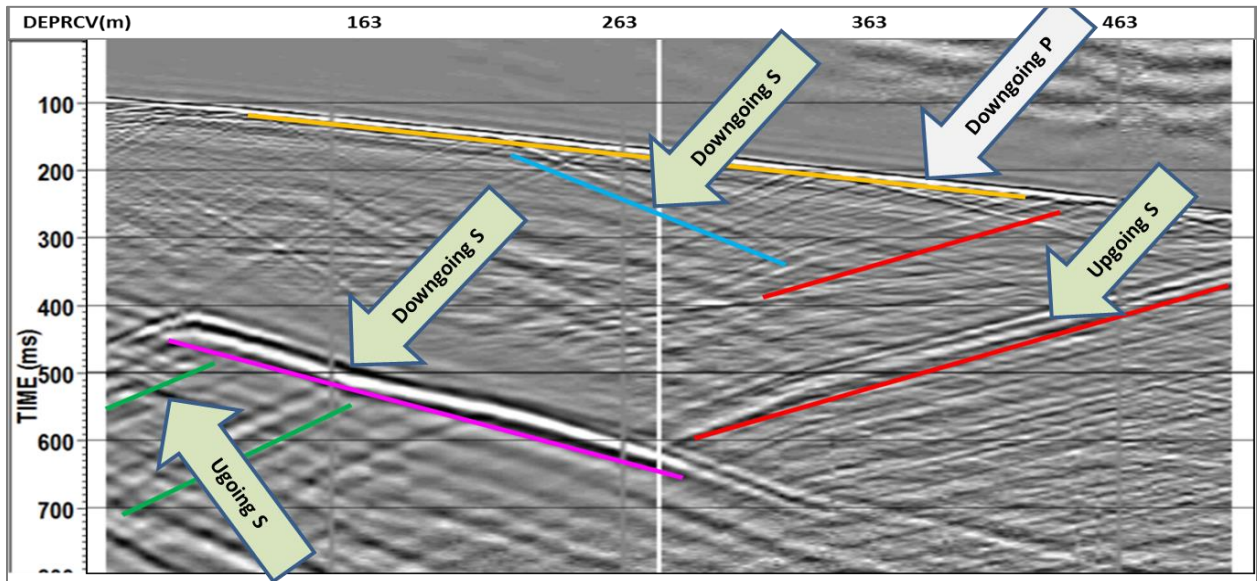


Figure 2-11. Vibroseis shot 4 (offset=153m) Hmax component. Different wave types were marked by color lines (display with AGC window=200 ms). Downgoing P was marked by a yellow line, downgoing SV (direct arrival) pink line, transmitted (downgoing) S blue line (converted from downgoing P), upgoing SV (converted from downgoing P) red line, and reflected SV wave (SS) the green line.

After preprocessing, the zero-offset and far-offset VSP data were processed separately. Referring to VSP processing course material (Hinds, 2007) and processing tutorials in the VISTA system, workflows for this VSP experiment were designed. Figure 2-12 shows the flow charts of

both zero-offset and far-offset VSP processing. The details of processing parameters and results are introduced in the following section.

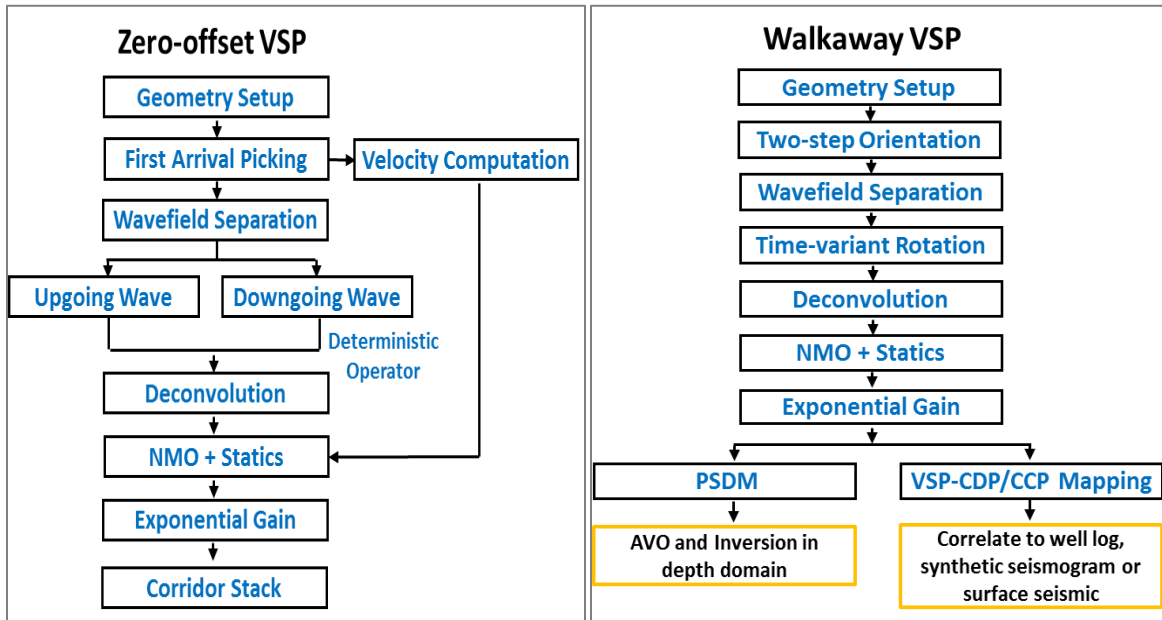


Figure 2-12. Zero-offset (left) and far-offset (right) VSP processing sequence.

### 2.3.3 Zero-offset VSP processing

The interval velocity profile was calculated from first arrival time of zero-offset VSP shot shown in Figure 2-13. Any anomalies of the velocity were recomputed after correcting the first arrival picking time or were deleted. The interval velocity range is from 1700 m/s to 2500 m/s. These velocities were used to compute the NMO correction, time-variant polarization of far-offset VSP data and calibration. These processes will be discussed in detail later.

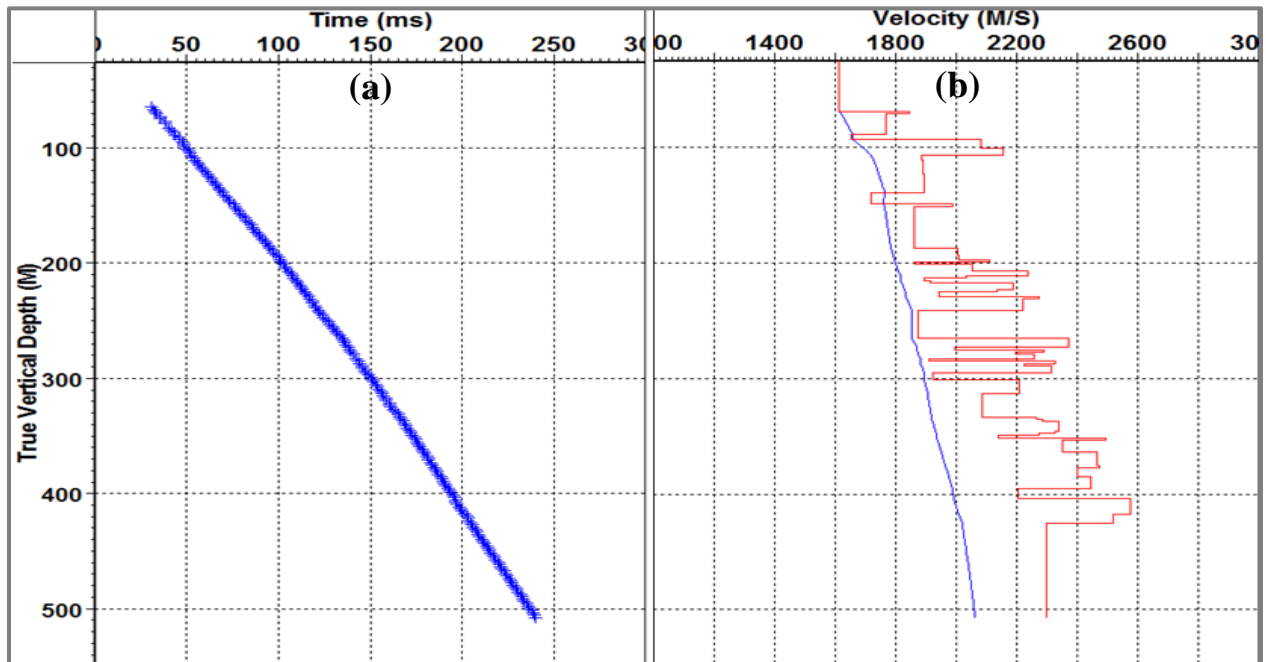


Figure 2-13. Velocity profile calculated from first arrival time of zero-offset VSP data. (a) First arrival picks, (b) calculated average velocities are in blue and interval velocities in red.

First arrivals were flattened to arbitrary time to align downgoing waves. Then median filtering was used to separate downgoing and upgoing wavefields. Different filter length (trace number), was tested from 11 to 21 traces. The results indicated that longer filter worked better to separate upgoing waves from downgoing waves. Thus a 19-trace median filter was chosen for the wavefield separation in this project. Figure 2-14 shows the Z component of shot 1 (offset =11 m) before (Figure 2-14a) and after median filter (Figure 2-14b and c). It can be seen that the upgoing wavefield (Figure 2-14b) contains a little downgoing SV wave contamination (200 – 500 ms of shallow receivers, highlighted by red ellipse). Downgoing multiples can be easily spotted on downgoing waves (Figure 2-14c) which need to be attenuated subsequently by deconvolution in the processing. Weak residue of strong reflected upgoing wave (reflected is at about 550 m depth, highlighted by red ellipse) also presents on downgoing wavefield after median filtering.

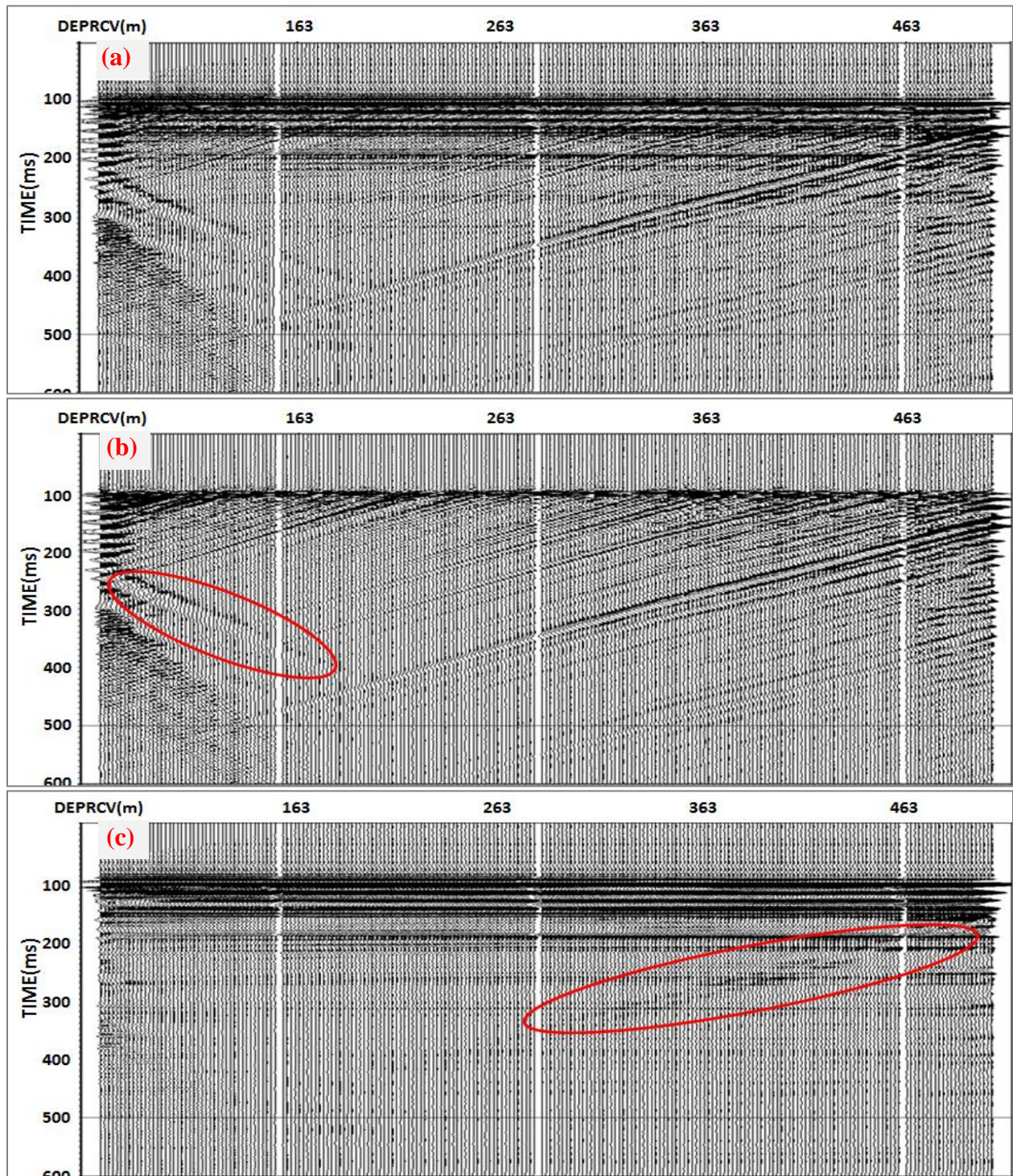


Figure 2-14. Raw vertical component of zero-offset shot before and after wavefield separation. (a) Raw shot; (b) separated upgoing waves; (c) downgoing waves were separated by a 19-trace median filter and displayed in  $-TT$  time (flattened on first arrivals). Red ellipses mark downgoing SV on separated upgoing wavefield and residual upgoing waves on the separated downgoing wavefield.

A deconvolution operator was designed on the downgoing wave within window from -50 ms to +250 ms from the first arrival time. Based on tests, the 300 ms operator length and 5% pre-whitening were applied. Figure 2-15 shows downgoing waves and their amplitude spectra before and after deconvolution. It can be observed that the downgoing multiples were greatly suppressed and the frequency spectra were whitened after deconvolution (Figure 2-15b). Furthermore, signal-to-noise ratio was also enhanced by deconvolution. This operator was then applied to the upgoing wavefield. Figure 2-16 shows the data before and after deconvolution. Both sharpness of events and signal-to-noise ratio are improved. The deconvolution also corrected output data to zero phase.

Amplitude loss was recovered by two procedures: (1) an amplitude scalar was calculated from downgoing wave (window= $\pm 10$  ms from first break time) and applied to the upgoing wave field to compensate amplitude loss along downgoing wave travel path; (2) exponential gain was then applied to account for amplitude loss (absorption as well) along upgoing wave path. In this case, parameter 1.6 was used to calculate gain value from first arrival time. Figure 2-17a shows the result of amplitude recovery. The amplitude is balanced well over depth and time.

NMO correction was then applied on the data before corridor stack. Since the zero-offset shot in a very small source-receiver distance (11 m), the NMO effect is not obvious (Figure 2-17b). However, it is still preferred to correct moveout caused by non-zero offset. Statics were applied on NMO-corrected upgoing waves (Figure 2-17c). After NMO and statics applied, all the reflections were flattened so that they can be stacked constructively.

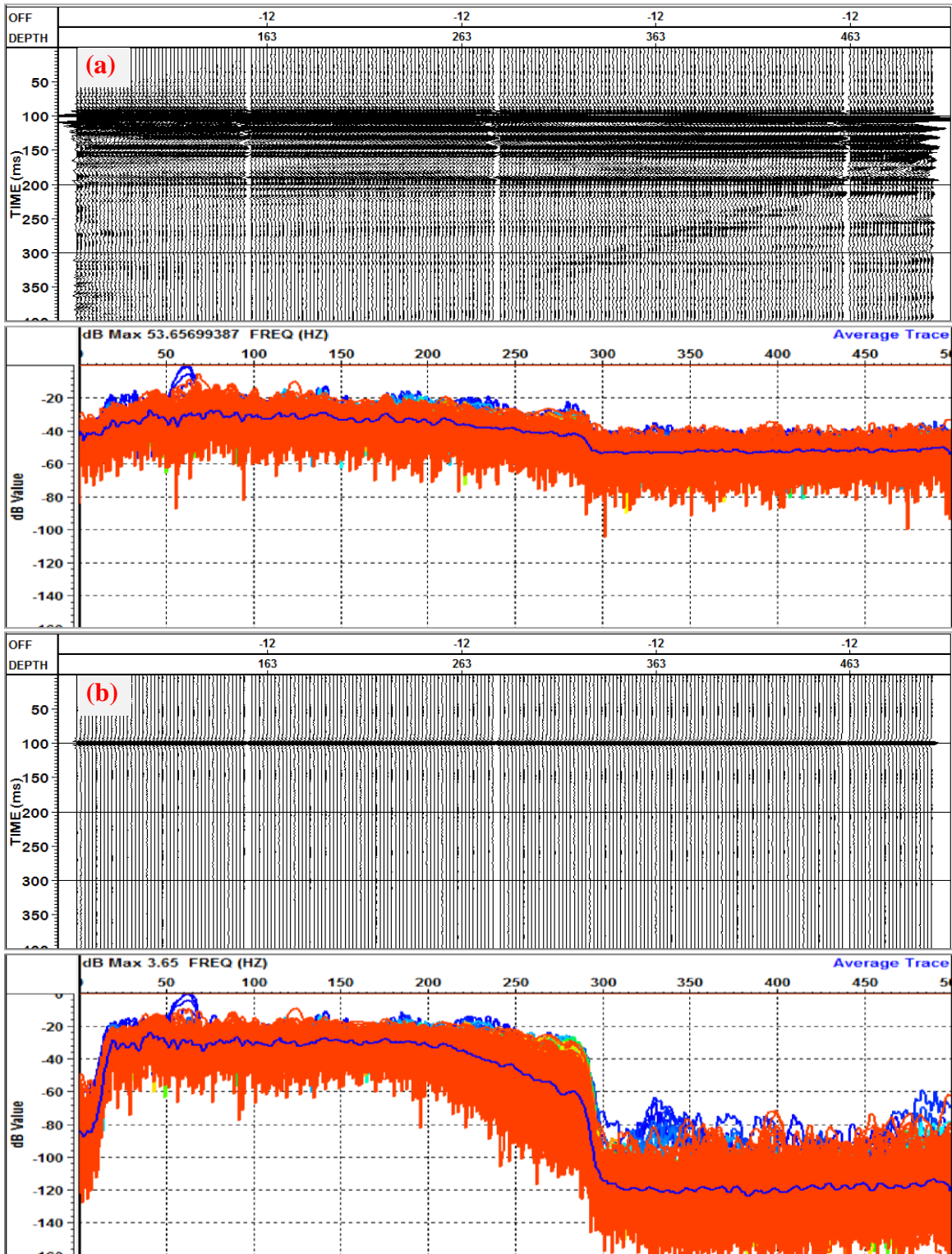


Figure 2-15. (a) Downgoing P wave (-TT time) and its amplitude spectrum before deconvolution. (b) Downgoing P wave (-TT time) and its amplitude spectrum after deconvolution. Average spectrum is displayed as a blue curve, and the color traces are spectra of individual traces.

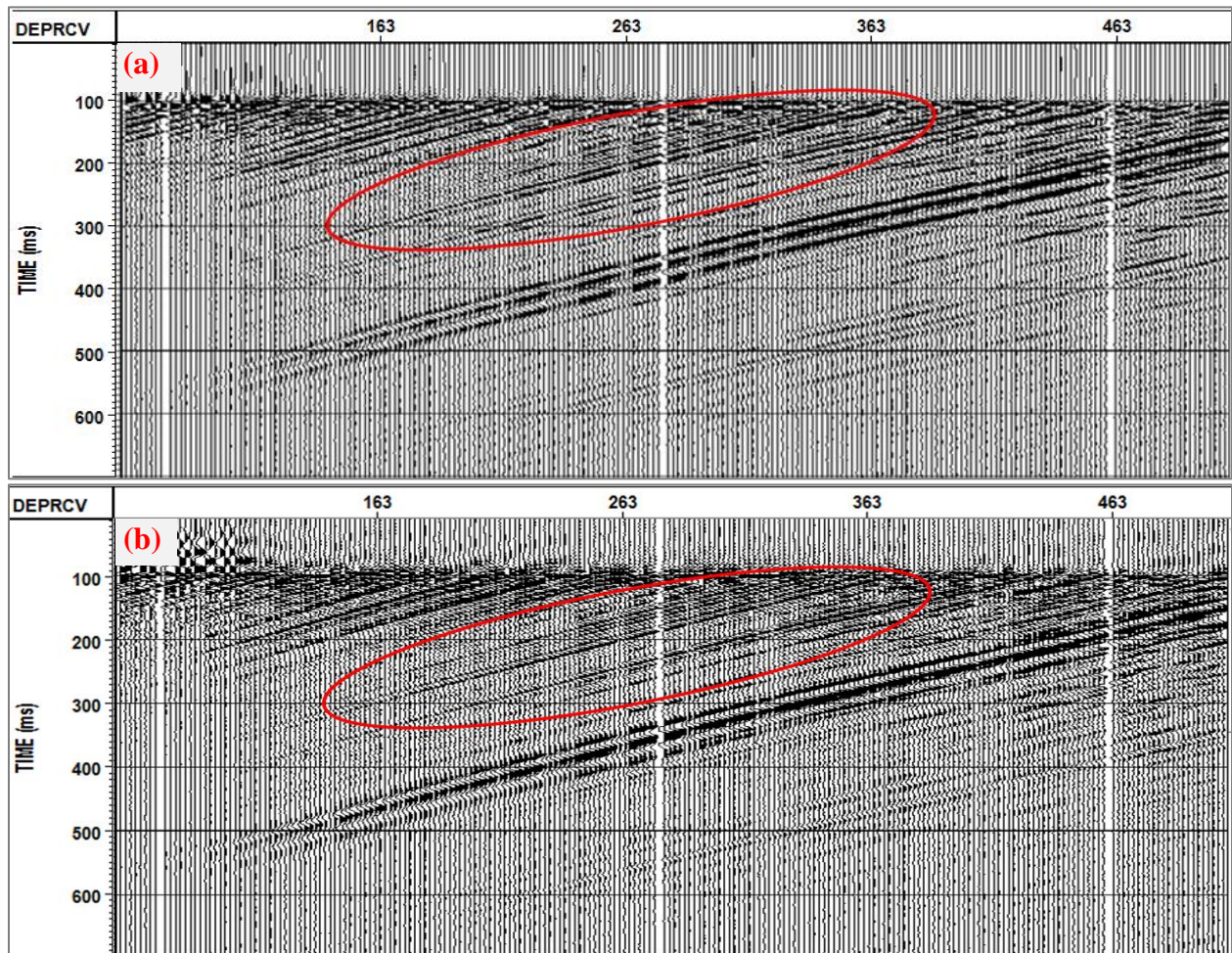


Figure 2-16. (a) Upgoing waves before deconvolution; (b) Upgoing waves after deconvolution. Both data displayed in -TT time. Red ellipses highlight the difference before and after deconvolution. After the deconvolution, events show higher resolution and better consistency.

Although noise attenuation was implemented with 5-trace median filter, SV wave contamination is still seen in the data (Figure 2-17c, highlighted by a red ellipse). Residual multiples are also expected to present. Since these were outside the defined corridor, they will not degrade the corridor stack. In this study, a 30 ms corridor mute was applied, based on the data. The corridor gather and stacks are shown in Figure 2-18. Comparing the corridor and full stacks, apparently, without contamination of multiples, corridor stack has higher resolution and signal-to-noise ratio than the full stack.

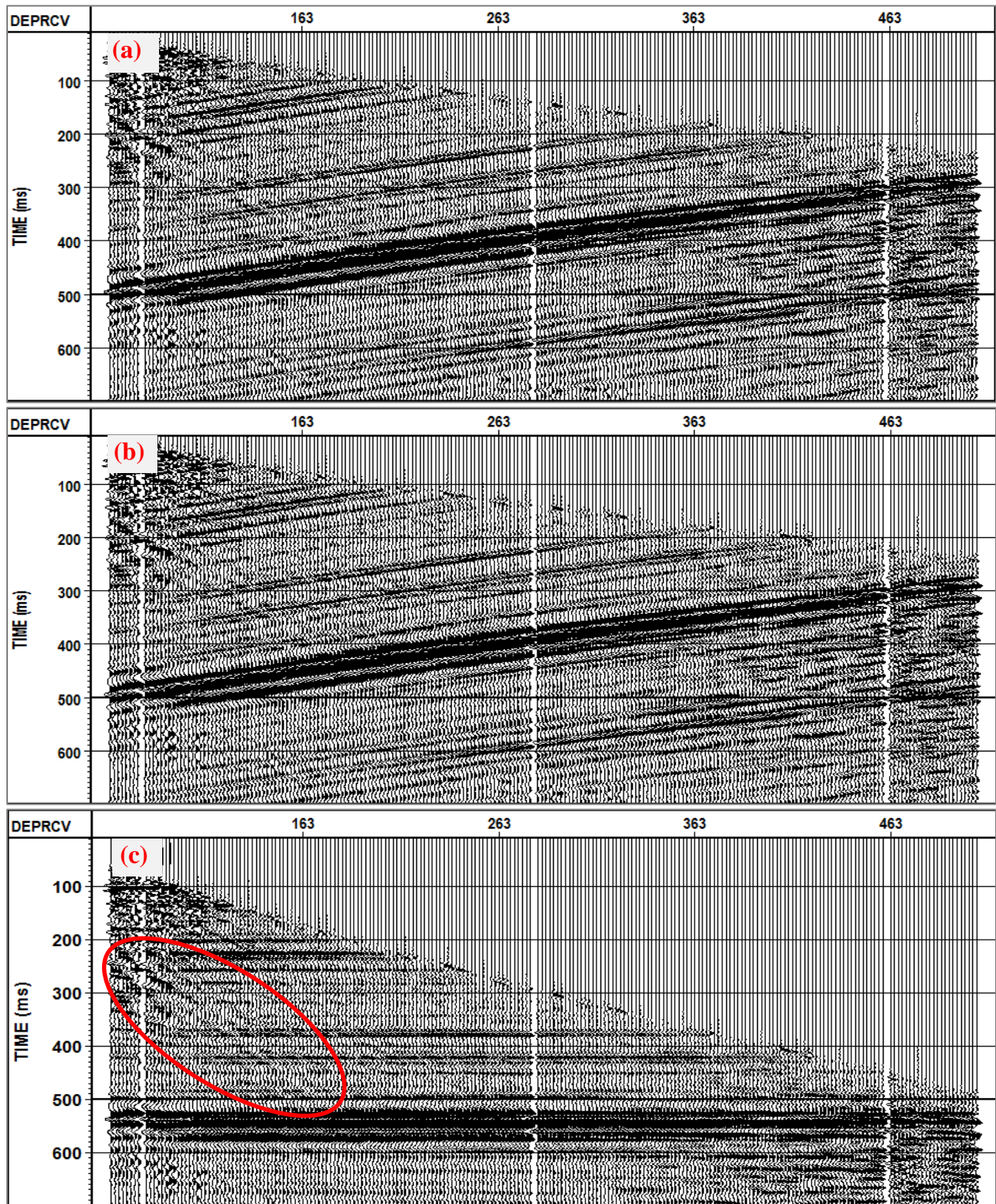


Figure 2-17. (a) Upgoing waves after exponential gain; (b) with NMO correction; (c) applied statics shifting. Red ellipse highlights SV wave contaminations.

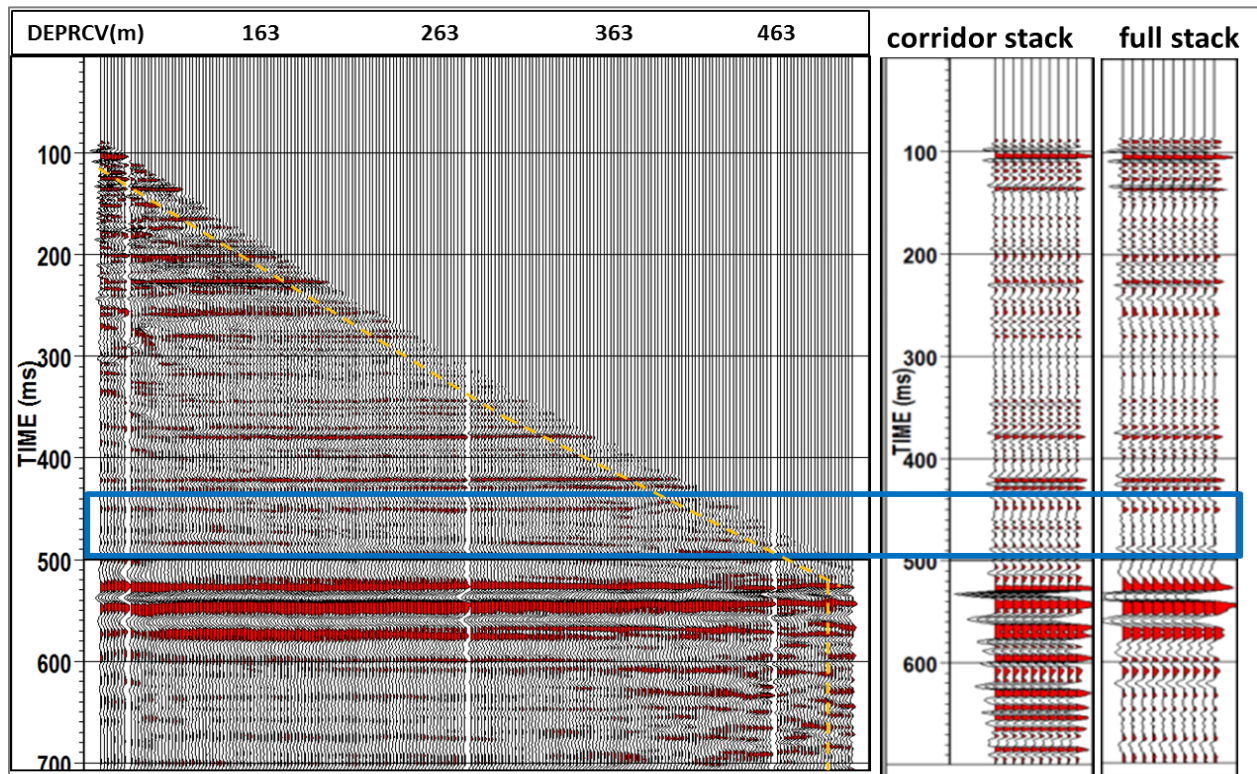


Figure 2-18. The processed upgoing P-wave gather with corridor mute (yellow dash line), 10 fold corridor and full stack. The reservoir zone is highlighted by the blue rectangle. The corridor stack shows better resolution than the full stack.

### 2.3.4 Offset VSP processing

In preprocessing, the X and Y components were already rotated into Hmax and Hmin. However, various wave types still appear on both Hmax and Hmin components. In particular, it is not possible to separate downgoing P from any single component, which is important for deconvolution operator design. So the second rotation is required to transform the vertical component Z and Hmax into Hmax' and Z'. Hmax' towards to source direction and Z' is perpendicular to it. Figure 2-19 shows the hodogram analysis of the second rotation. Hodogram is a crossplot of two components of particle motion over a time window. Hodograms are used in borehole seismology to determine arrival directions of waves and to detect shear-wave splitting. From the figure, it was seen that the rotation angle (angle between horizontal and source-receivers direction) increased with depth due to VSP geometry. Figure 2-20 shows the data before and after the second rotation. After rotation, it is assumed that only downgoing P and upgoing SV energy on Hmax', and upgoing P and downgoing SV waves dominates Z'. Although

the real data contain other types of modes, these assumptions benefit the subsequent wavefield separation and other processing.

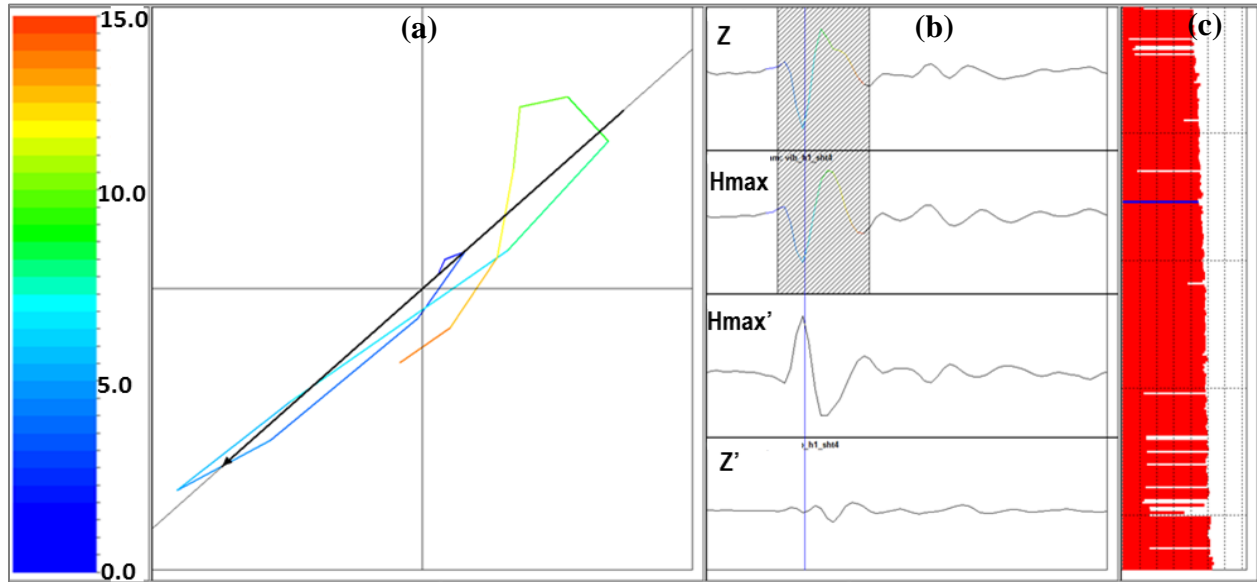


Figure 2-19. The second hodogram analysis of Vibroseis shot 4. (a) The hodogram plot of a trace (channel=270, colored by time), black line shows the picked polarization; (b) two input components (Z and Hmax) and output components (Hmax' and Z'); (c) rotation angles of all the receivers in the current shot.

Similar to the zero-offset VSP processing, the first arrivals were flattened to an arbitrary time to align downgoing wave of Hmax' and Z' components. Then a median filter was used to separate downgoing and upgoing wavefields. Different filter lengths (from 11 to 19 traces) were tested for this dataset (Figure 2-21). The results indicate that shorter filter preserves downgoing waves better but more upgoing waves remain on the downgoing wavefield, and vice versa. Finally, an optimized 15 trace median filter was applied for this shot.

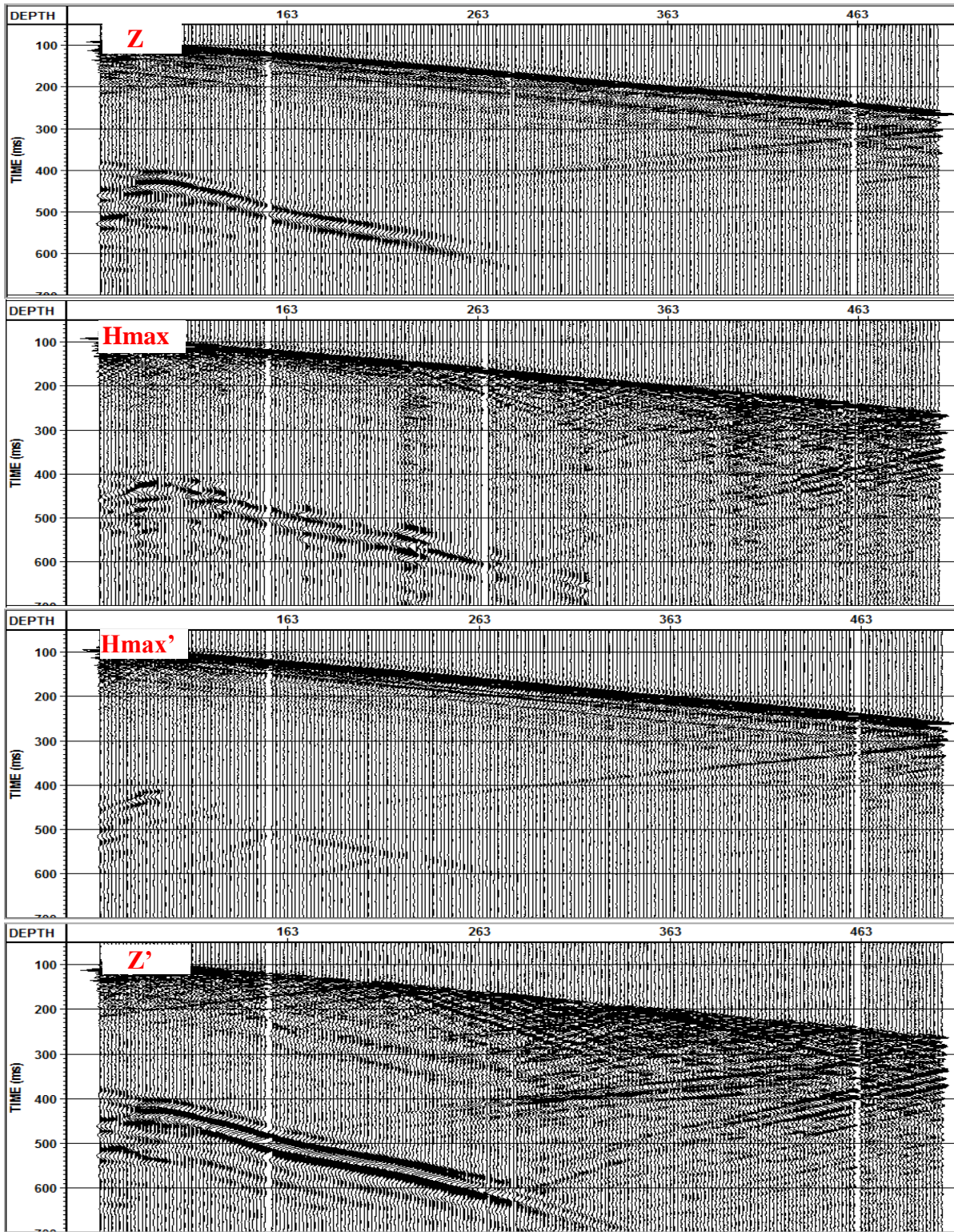


Figure 2-20. Rotation of Z and Hmax into Hmax' and Z'. After rotation, Hmax' is dominated by downgoing P-wave and upgoing SV wave energy, and Z' is dominated by upgoing P-wave and downgoing SV wave energy.

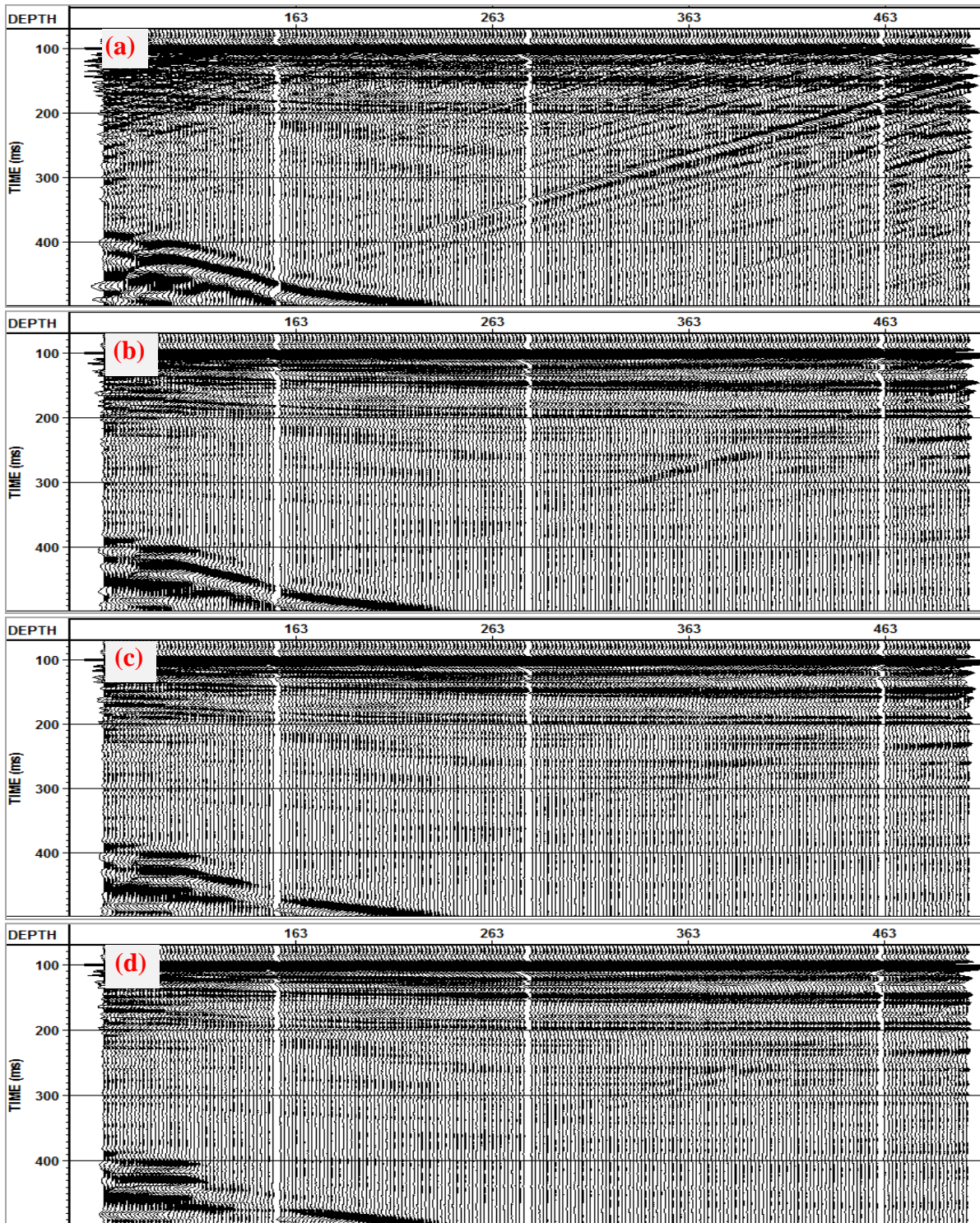


Figure 2-21. Median filter test on a shot (offset=153 m). (a) Raw Z component, (b) downgoing wave separated by 11 trace filter, (c) downgoing wave separated by 15 trace filter, (d) downgoing wave separated by 19 trace filter respectively.

As discussed in the techniques section, time-variant wavefield polarization should be applied in far-offset VSP processing due to incident angle variation with depth. In practice, the upgoing waves were separated from  $Z'$  and  $H_{max}'$  and derotated back to original  $Z$  and  $H_{max}$  directions. Then the upgoing P and SV waves were separated through time-variant polarization based on the velocity model.

Figure 2-22 shows the derotated components. One is dominated by upgoing S-waves and the other is dominated by upgoing P-waves. Figure 2-23 and Figure 2-24 are the demonstration of ray tracing and time-variant rotation outputs separately. Upgoing P and SV waves were successfully separated as shown in Figure 2-24. However, some downgoing waves also present on both components since it is difficult to remove them by median filter only when isolating the waves. They can be removed by FK filter before VSP-CDP mapping.

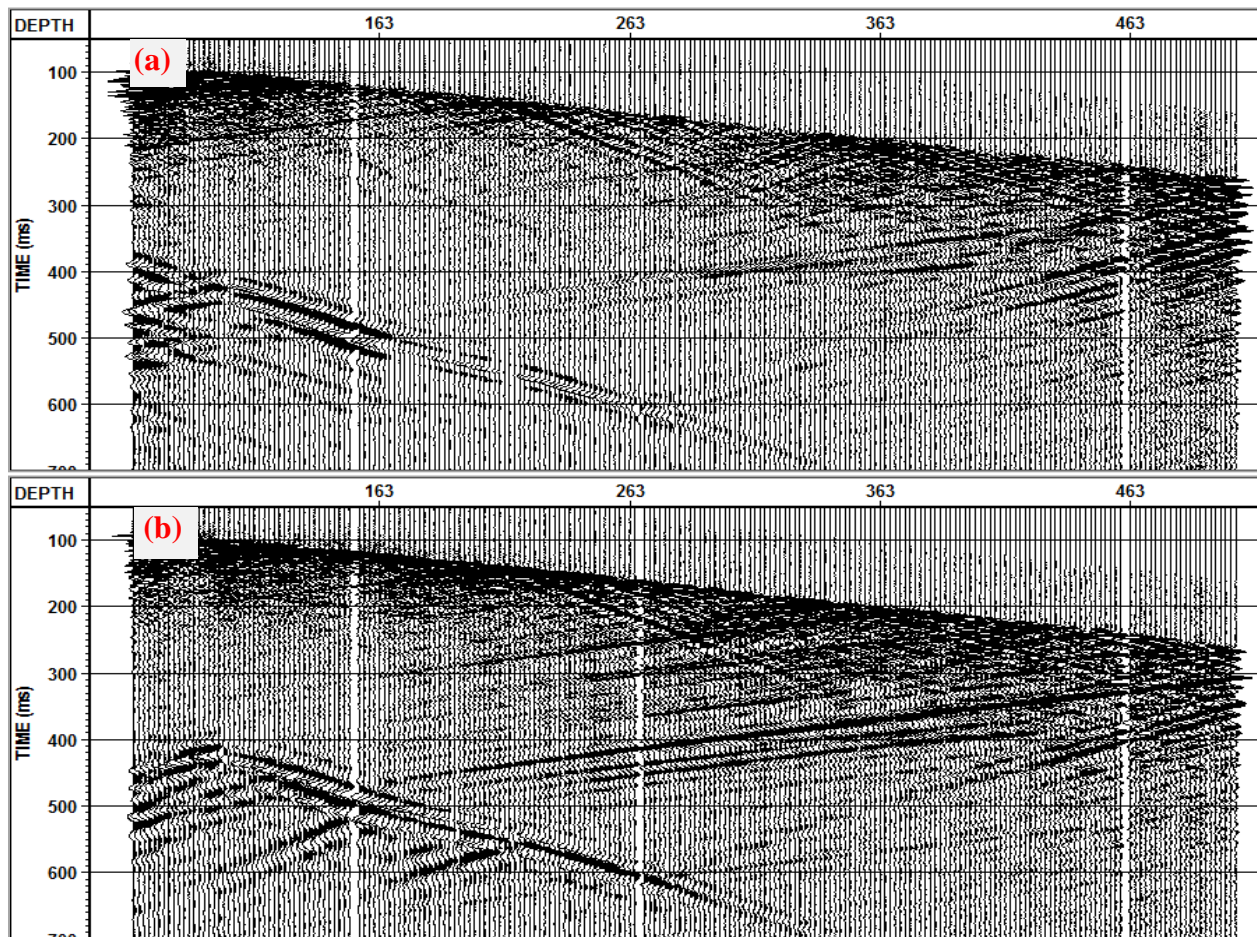


Figure 2-22. (a)  $H_{maxdero}$  component after derotation of  $H_{max}'$  and  $Z'$  upgoing wavefield. (b)  $Z_{dero}$  component after derotation.  $H_{maxdero}$  is dominated by upgoing S-waves while  $Z_{dero}$  is dominated by upgoing P-waves.

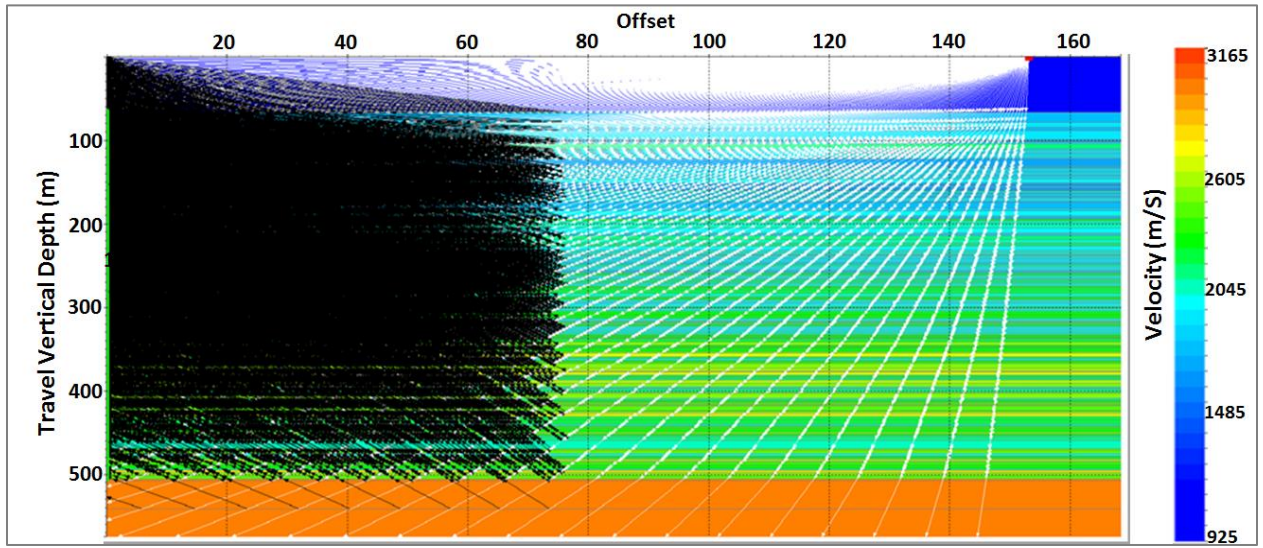


Figure 2-23. Ray tracing (200 rays were used for demonstration, 2000 rays for actual processing)

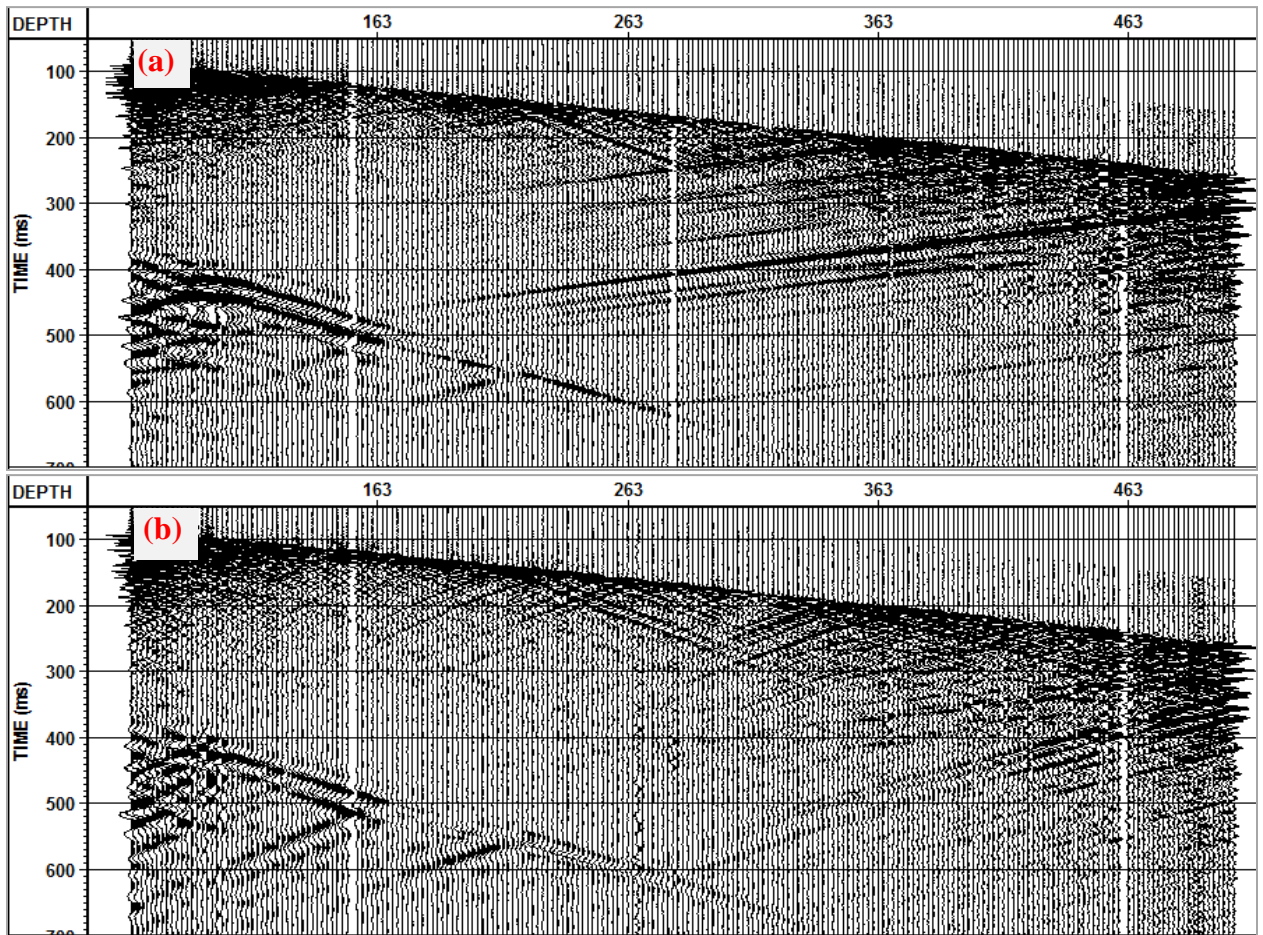


Figure 2-24. Time-variant rotation results. (a) The component contains upgoing P-waves; (b) the component contains upgoing SV waves. Note that each component contains some downgoing waves.

After the upgoing P and S-waves were isolated by time-variant polarization, a deconvolution operator, designed from the downgoing first arrivals waves, was applied to upgoing waves. Then exponential gain, VSP NMO, residual converted-wave or P-wave event attenuation by FK filter, signal enhancement by 5-trace median filter, and a band-pass filter were applied on the data. Finally, upgoing P-wave and converted-wave data were processed to the VSP-CDP or VSP-CCP mapping stage. Figure 2-25 shows the VSP-CDP mapping with 1 m to 3 m bin size. Considering the relatively small receiver interval in the well (2 m), 1 m bin size was chosen for the data.

Figure 2-26 shows images of P and converted-wave data. Only zero to middle offset shots were used in this study because the far offset data were noisy. The converted-wave images have less coverage than P-wave data but also have high signal-to-noise ratio and resolution than regular PS data. It was expected that the high quality PS image could benefit further interpretation, as will be discussed in chapter 4.

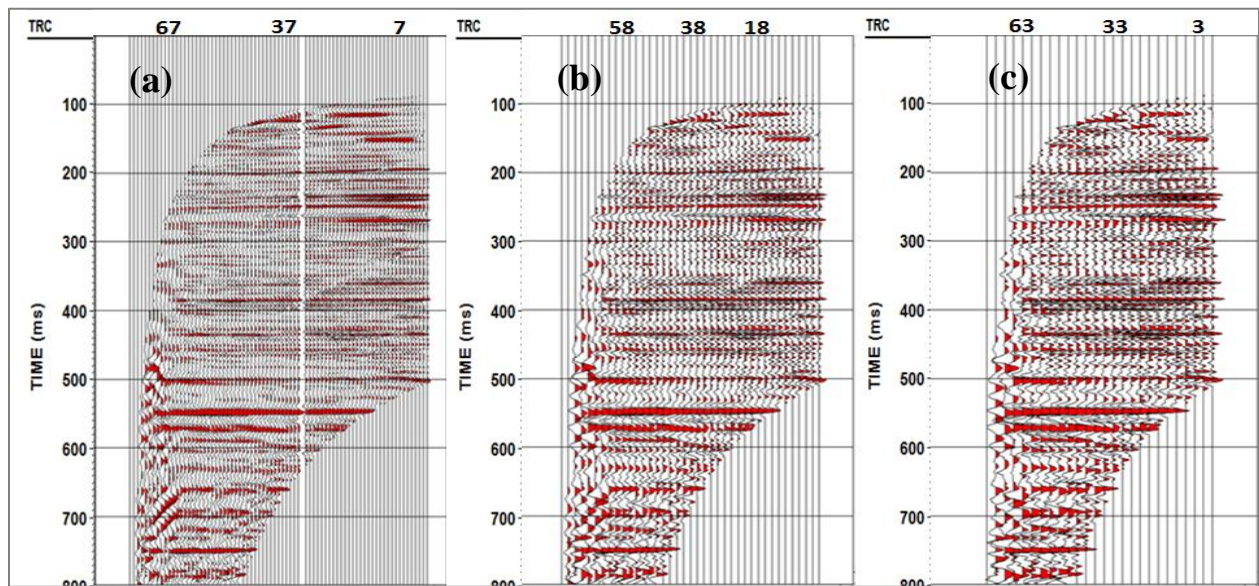


Figure 2-25. VSP-CDP stacked images of one shot example (offset =153 m). (a) Bin size=1 m, (b) bin size=2 m, and (c) bin size=3 m.

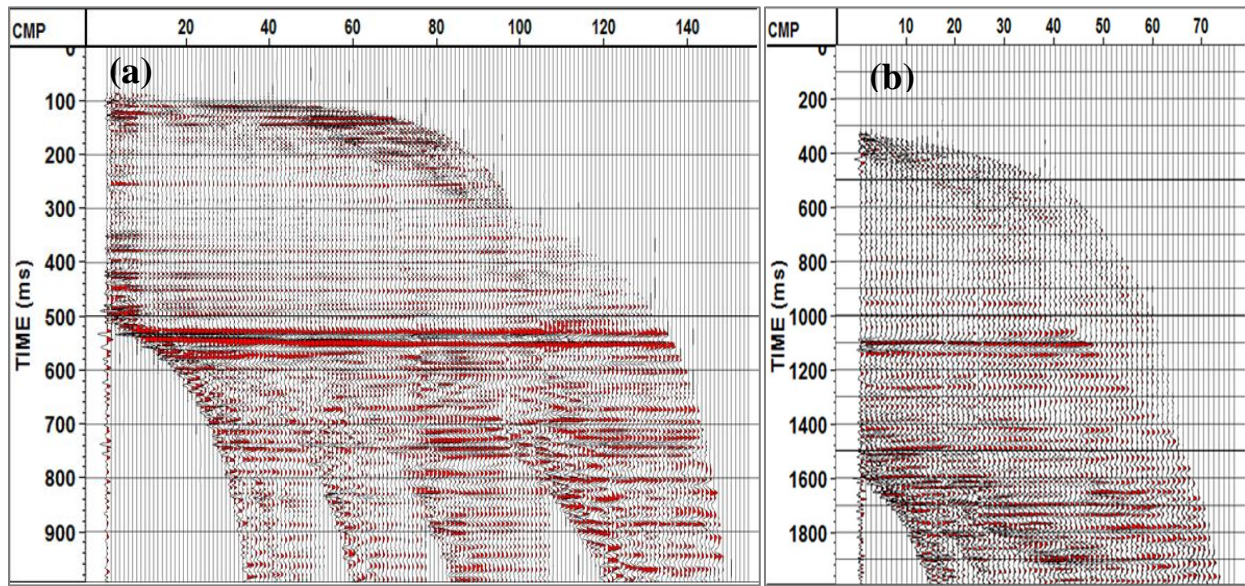


Figure 2-26. (a) VSP-CDP mapping of PP data and (b) VSP-CCP mapping of PS data. Both stacked images are merged traces from shot 1 to 6, offset from zero to 308 m, bin size=1 m.

## 2.4 Chapter summary

VSP processing techniques, and workflows of zero and offset VSP data, were introduced in this chapter, followed by real data examples from the reservoir studied. The small receiver interval in acquisition helped record different wave modes. Optimization of parameters in processing produced high resolution and good signal-to-noise ratio for PP and PS images. High quality PP-PS images promise to provide useful interpretations of the geology.

## CHAPTER 3 WALKAWAY VSP ANALYSIS

### 3.1 Introduction

The walkaway VSP data were processed following the workflows described in chapter 2. In order to obtain reliable interpretation, during the processing special attention was given to phase correction and true amplitude recovery. Amplitude recovery techniques include deterministic deconvolution, exponential gain and scaling calculated on the downgoing energy. In addition, well log calibration, correlation between synthetic seismogram and VSP data as well as PP-PS registration are all summarized in this chapter. Application of all these techniques prepared the input walkaway VSP data for inversion and AVO analysis.

### 3.2 Phases correction

Phase distortion and differences occur in data acquisition. Since two different type of sources, dynamite and vibrator, were used in data acquisition. For comparison, the phases of vibrator data were corrected to match the phase of the dynamite data by applying a match filter. Then, the phase rotation caused by receivers was corrected. The VectorSeis digital 3C sensor records acceleration, therefore the data show a phase shift of a minus 90 degrees compared to the data recorded by regular sensors which measure velocities. In order to compare to other surface seismic data (not available in this study) and to more accurately pick first break times, our VSP shots were corrected to minimum phase before processing. Figure 3-1 shows the horizontal component of dynamite shot 4 before and after phase correction.

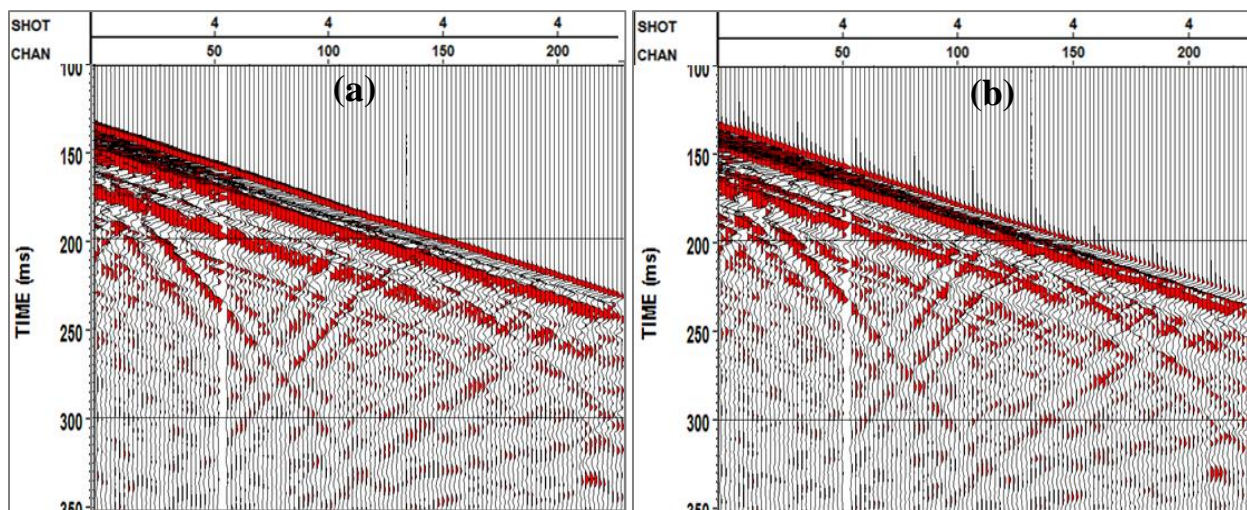


Figure 3-1 Horizontal component of dynamite shot 4 before and after a 90 degree phase rotation. (a) Before phase correction, (b) after phase correction, the data have minimum phase.

### 3.3 True amplitude recovery

One of the advantages of a VSP survey is that it makes it possible to apply a deterministic deconvolution. The deconvolution operator was estimated from the downgoing wave and applied to the upgoing wave. This processing compensates for the energy decay suffered during downward propagation. After deconvolution, the incident waves will have the same relative amplitude at each depth, and the downgoing wave is compressed in time to a zero-phase wavelet. Exponential gain was applied to correct the transmission loss from absorption. Details of these techniques and processing results were discussed in Chapter 2.

### 3.4 Correlation between VSP and synthetic seismogram

Accurate synthetic seismogram construction requires a dipole sonic and a counterpart density log. P-wave sonic and density logs from a nearby well (about 200 m away) are available in this area. Due to the difference in source frequency, a sonic log generally yield higher velocities than those from the VSP. Cumulatively, the VSP one-way P-wave travel time is about 8 ms longer than that calculated from the sonic log (Figure 3-2a and b). In order to tie a synthetic seismogram to the VSP data, the well logs were first calibrated to VSP velocities. The calibration of the sonic log is shown in Figure 3-2. After calibration, the drift between one-way P-wave travel time was corrected (Figure 3-2d).

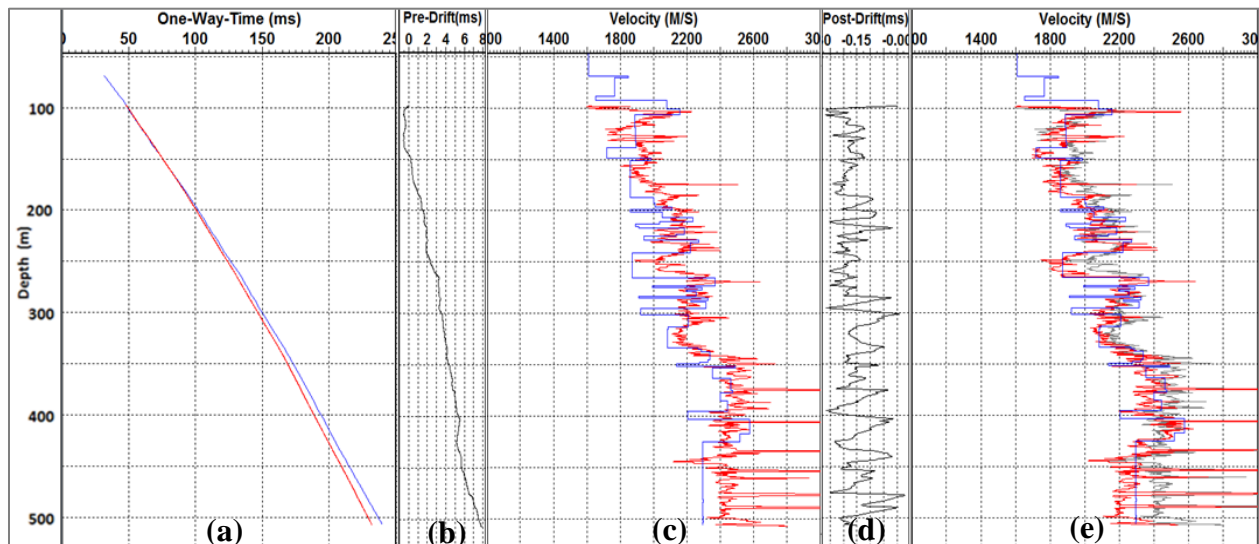


Figure 3-2. Sonic log calibration: (a) time-depth curves, VSP one-way P-wave travel time in blue, sonic log calculated one-way P-wave time in red, (b) time drift between VSP and well log before calibration, (c) comparison of VSP (blue) and sonic log (red) interval velocities before calibration, (d) time drift after calibration, (e) comparison of VSP (blue) and sonic log (red) interval velocities after calibration. The original sonic logs are plotted in grey.

A PP synthetic seismogram was generated by the calibrated sonic log using CREWES software Syngram. For fair comparison, a 60 Hz Ricker wavelet (Figure 3-3a) was used based on the VSP data frequency content (Figure 3-3b). The sonic log was blocked to 2 ms and the synthetic offset gather is shown in Figure 3-4. The reservoir zone is highlighted by a yellow rectangle.

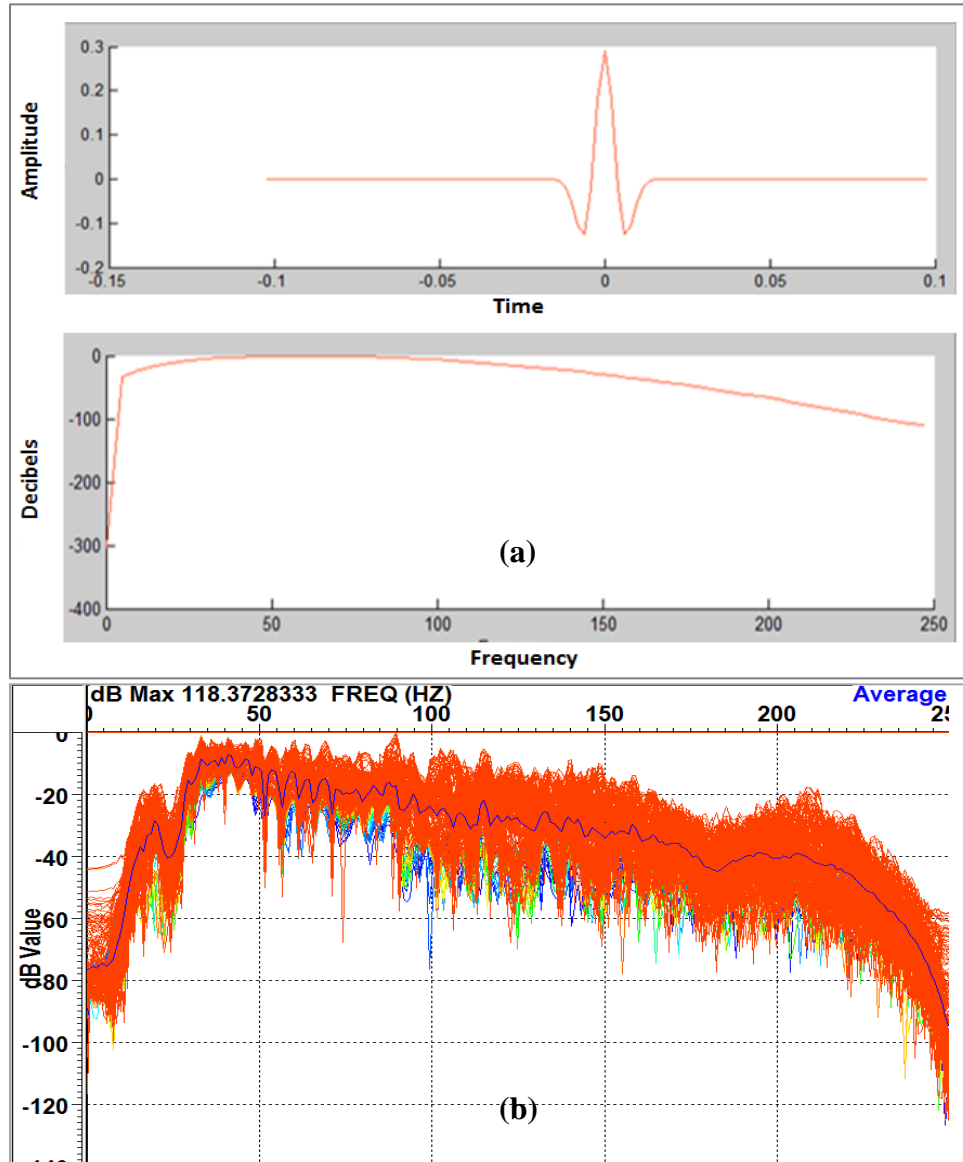


Figure 3-3. Input wavelet of synthetic seismogram and spectrum analysis of the VSP data. (a) The 60 Hz Ricker wavelet; (b) spectrum of the VSP data (P-wave). The Ricker wavelet and the VSP data have similar spectra.

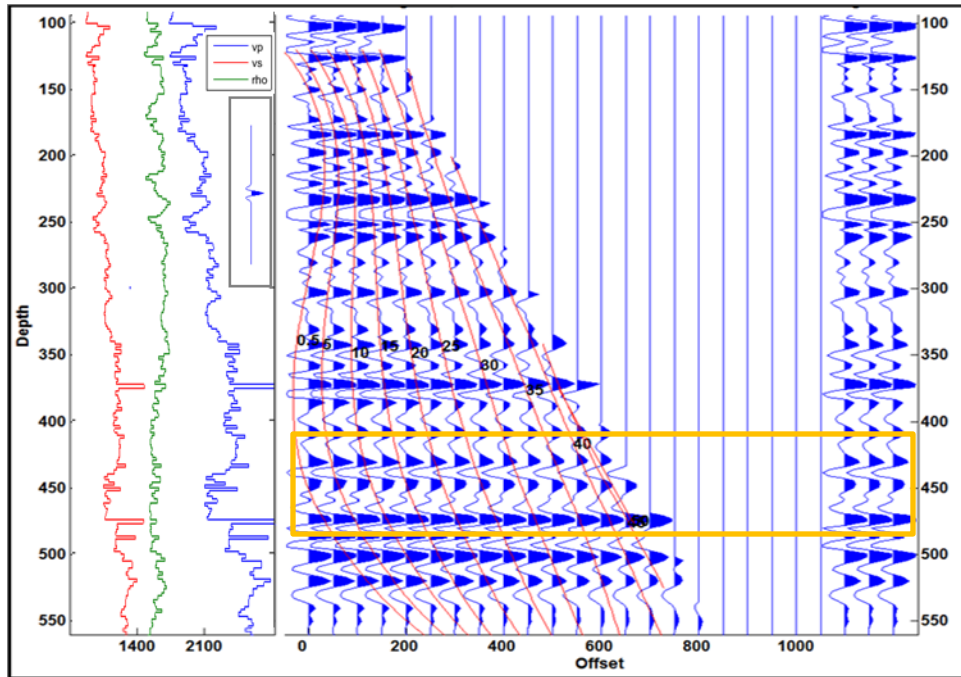


Figure 3-4. Synthetic offset traces gather and stacked traces of the gather (3 fold). Red curves are the incident angles. The reservoir zone is highlighted by the yellow rectangle.

The composite plot (Figure 3-5) shows the detailed correlation between sonic log, VSP-CDP mapping of the upgoing P-wave data from an offset VSP shot (offset=153 m), processed upgoing P-wave gather (zero-offset shot), corridor and full stack of the zero-offset VSP shot, plus a synthetic seismogram. Overall, geological markers in this area show a good correlation between VSP and synthetic seismograms. However, few strong reflections on the synthetic seismograms are not seen on the VSP data. The reason is that thin high velocity layers yield strong reflections on the synthetic seismic might be too thin to be resolved in the VSP data.

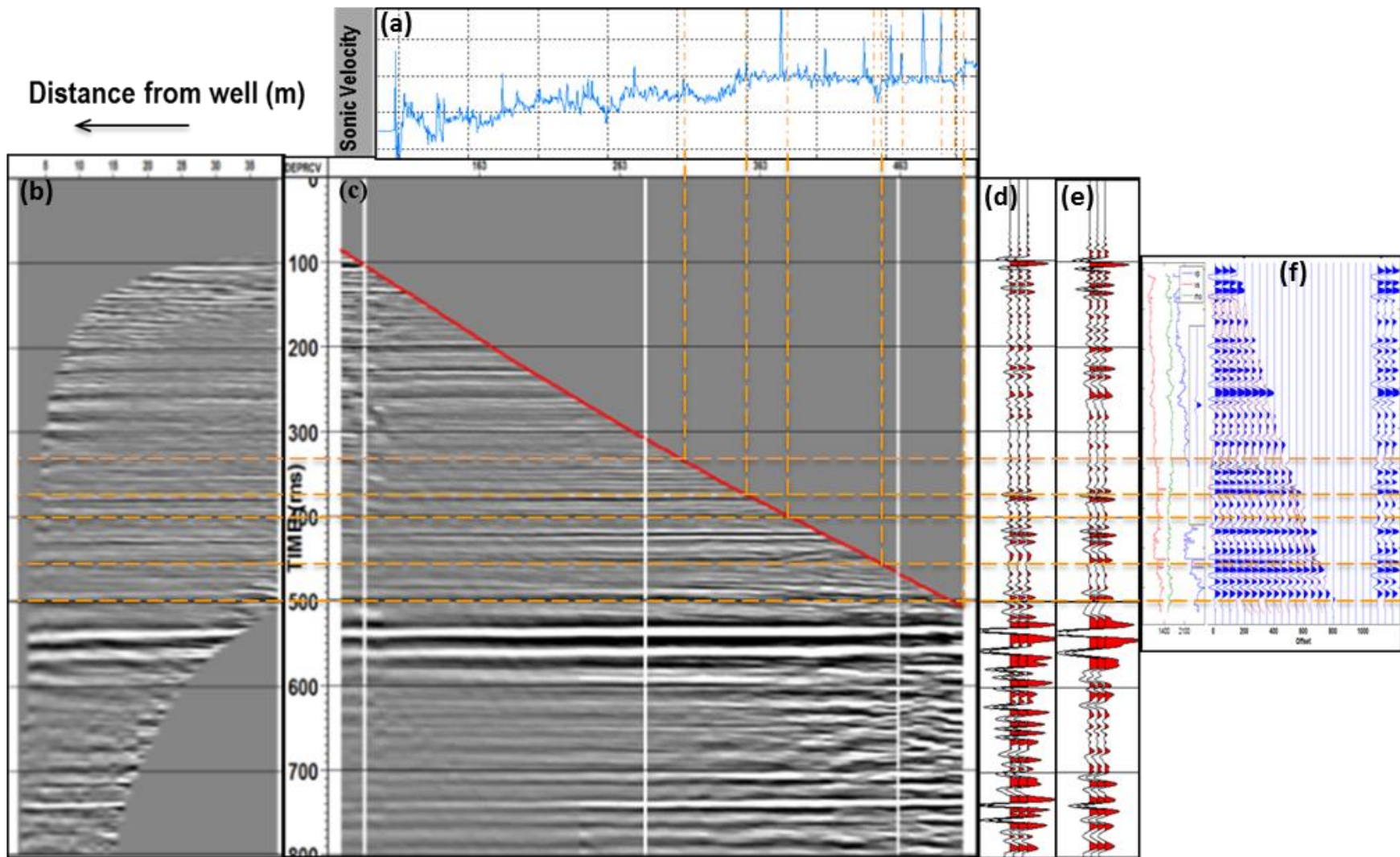


Figure 3-5. Composite plot of the sonic log, VSP data and synthetic seismogram. (a) Sonic log, (b) VSP-CDP mapping of an offset shot (offset=153 m), (c) processed upgoing P-wave gather of the zero-offset shot, (d) corridor stack and (e) full stack of the zero-offset shot, (f) synthetic offset seismic gather and its stacked traces (3 fold). Dash lines highlight geological markers in this area.

### 3.5 Registration of PP and PS data

In order to interpret multicomponent data, registration of PP and PS data must be performed. Success in PP-PS registration depends on the ability to identify the same reflectors on PP and PS sections. Most of methods for PP-PS registration are based on the assumption that the PP and PS wavelets reflected from same boundary are similar in shape, polarity and strength (Zou et al., 2006). However, in practice, several intrinsic problems make the assumption not always valid, and make picking the same reflectors on PP and PS sections quite challenging. The problems may include: (1) the reflection responses of PP and PS data from the same rock may be different; (2) in many environments,  $Q$  in the shallowest weathering layers may be very low so PS-wave data tends have lower dominant frequencies than the P-wave data; (3) the processing procedure also brings artifacts to the final image.

In addition, a few other factors make the PP and PS registration more complicated. When PS events are recorded near their point of origin (the conversion point), they will have same temporal frequency as the P-waves. Hence, the PS events often have significantly higher resolution or apparently shorter wavelengths than the P-waves. Compressing the PS section to PP time also improves the apparent vertical resolution, which makes registration more challenging.

In this study, the VSP acquisition pattern helps solve many noise problems, and increases the PS signal bandwidth. Also the VSP survey records both receiver depth and time, which make the picking of major events in the target area from PP and PS data easier than from surface seismic data.

With an accurate velocity field or time-depth relationship, pre-stack depth migration could be applied to both PP and PS data volumes and results in direct ties in depth. In practice, it is not difficult to obtain P-wave velocities by picking direct arrivals from the zero-offset shot, but it is not easy to pick first arrivals of converted-waves. Alternatively, in this study, the S-wave velocities were obtained by velocity scan.

Figure 3-6 shows the flattened PS gather by estimated velocities. Flattened events indicate accurate S-wave velocity. But this manual velocity scan method has limited resolution.

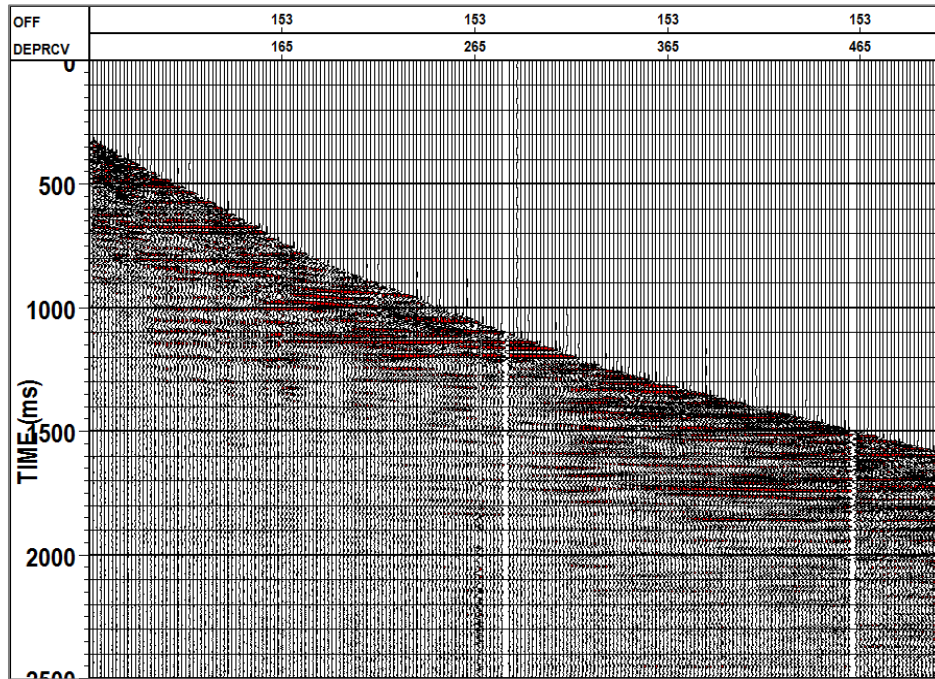


Figure 3-6. A processed converted-wave gather flattened by estimated S-wave velocity. Flatten events indicate good estimation of S-wave velocities.

Garotta provided a method to calculate  $V_p/V_s$  by following relationship (Garotta, 1987):

$$\frac{V_p}{V_s} = \frac{(2\Delta T_{ps} - \Delta T_{pp})}{\Delta T_{pp}} \quad (3-1)$$

where,  $V_p$ ,  $V_s$  are the P-wave and S-wave velocities and  $\Delta T_{pp}$  and  $\Delta T_{ps}$  represent the isochron value across the same depth intervals for both PP and PS sections.

Based on the Garotta's function, a few horizons are picked on both PP and PS data, and calculated results are listed in Table 3-1. The calculated  $V_p/V_s$  shows good consistency with results of the velocity scan on the seismic data but it shows larger error compared to nearby well logs. The closest well with shear wave velocity log is about 500 m away. The distance may be the main reason for the error.

Table 3-1. Comparison of calculated Vp/Vs from Garotta method, velocity scanning on seismic and measurements from nearby well log

Trace number	MD	Tpp	Tps	$\Delta T_{pp}$	$\Delta T_{ps}$	Vp/Vs	Seismic Vp/Vs	Log Vp/Vs
19	100	63	101					
65	193	162	335	99	234	3.73	3.8	3.8
104	271	241	510	79	175	3.43	3.4	4.7
152	367	330	680	89	170	2.82	2.6	2.7
184	431	372	760	42	80	2.81	2.6	3.3
222	507	488	944	116	184	2.24	2.1	2.6

From the P-wave and estimated S-wave velocities, pre-stack depth migration was conducted to obtain the images shown in Figure 3-7. In the figure, the PP and PS volumes show similar signatures, but due to aforementioned reasons, it is still hard to identify the same reflectors. Furthermore, the limited accuracy of the S-wave velocity and small aperture of the VSP survey degraded the reliability of PSDM migration and PP-PS registration in the depth domain. Therefore, in this study, I focused on time domain analysis. Figure 3-8 shows the PP-PS registration results. PS data had been transformed to PP time by picking the corresponding horizons on both datasets.

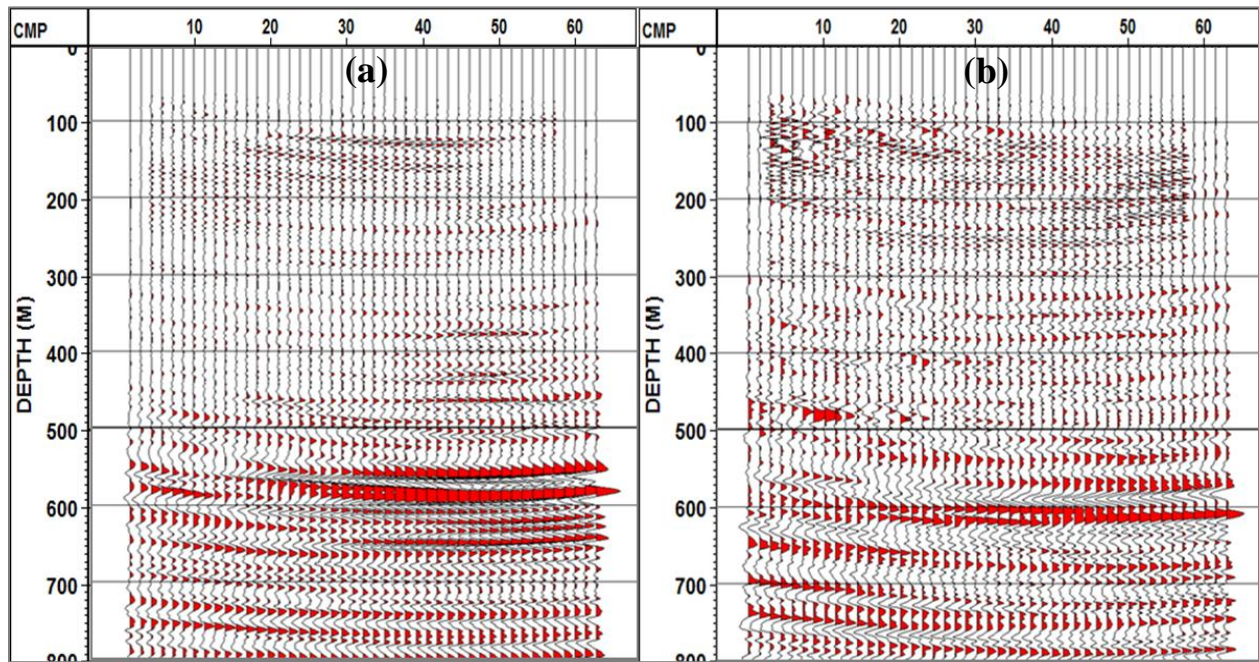


Figure 3-7 Prestack depth migration of P-wave (a) and converted-wave data (b). Poor tie of PP and PS images result from errors in shear-wave velocities and the small aperture of the VSP survey.

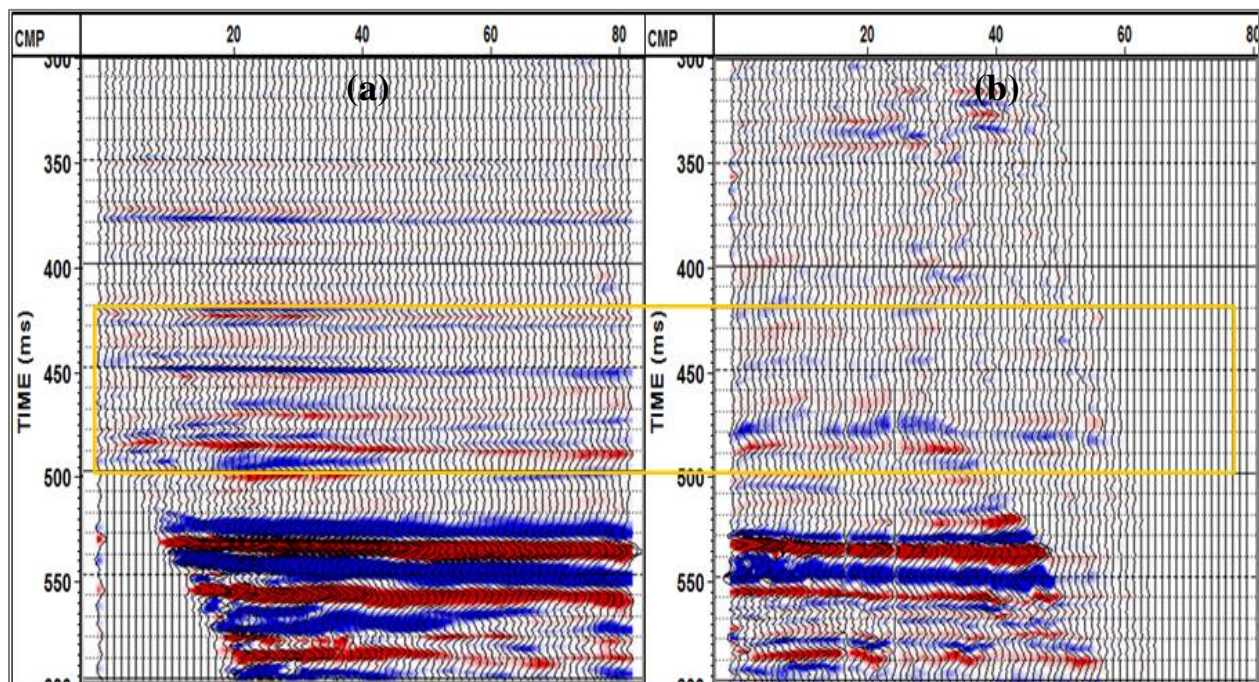


Figure 3-8. Registration of PP (a) and PS data (b). PS data have been transformed to PP time. The yellow rectangle highlights the reservoir zone.

### **3.6 Chapter summary**

In this chapter, data preparation for continued interpretation was introduced. Firstly, techniques for true amplitude recovery in processing were summarized. Secondly, the well log was calibrated to VSP velocity then was used to create a synthetic seismogram. Next, the processed VSP data were correlated to the synthetic seismogram. In order to interpret the converted-wave data, a PP-PS registration was also conducted. With proper preparation, the data were then ready for inversion and AVO analysis. All the analyses are based on the assumption that the dataset has been processed optimally to remove the spatial variations, and it is also time invariant.

## CHAPTER 4 INVERSION AND AVO ANALYSIS

### 4.1 AVO attributes

AVO is an adaptive technique. The most common method of AVO analysis for fluid and rock properties from seismic data is the use of two-term approximations. The linear combination of intercept and gradient is the basis of fluid and rock discrimination from seismic. AVO fundamentals were introduced in Chapter 1. In this work, the popular attributes applied in industry were applied in the target reservoir analysis and are listed in Table 4-1. The principles of each attribute are briefly introduced as follows.

Table 4-1. AVO attributes studied in this work

	Two-term Aki-Richards	Two-term Fatti method
)Attributes	Intercept A	Rp(0°)
	Gradient B	Rs(0°)
Derived attributes	AVO product: A*B	Fluid Factor
	Change of Poisson's Ratio: A+B	Lambda-Mu-Rho
	Shear wave reflectivity: A-B	

#### 4.1.1 Intercept A, Gradient B, and AVO product A\*B

Wiggins form (1983) of the two-term Aki-Richard equation is:

$$R_{\theta} = A + B \sin^2 \theta \quad (4-1)$$

where:

$$A = \left[ \frac{\Delta V_p}{2V_p} + \frac{\Delta \rho}{2\rho} \right] \quad \text{and} \quad B = \frac{\Delta V_p}{2V_p} - 4 \left[ \frac{V_s}{V_p} \right]^2 \frac{\Delta V_s}{V_s} - 2 \left[ \frac{V_s}{V_p} \right]^2 \frac{\Delta \rho}{\rho}$$

A is the intercept, B is the gradient, and A\*B is the AVO product.

#### 4.1.2 Poisson's Ratio change: A+B

Shuey (1985) proposed the equation:

$$B = A \left[ D - 2(1 + D) \frac{1 - 2\sigma}{1 - \sigma} \right] + \frac{\Delta\sigma}{(1 - \sigma)^2} \quad (4-2)$$

where:

$$D = \frac{\Delta V_p / V_p}{\Delta V_p / V_p + \Delta \rho / \rho}, \sigma = \frac{\sigma_2 + \sigma_1}{2}, \text{ and } \Delta\sigma = \sigma_2 - \sigma_1$$

The equation can be simplified by assuming  $\sigma = 1/3$ :

$$B = 2.25\Delta\sigma - A \quad (4-3)$$

or

$$A + B = 2.25\Delta\sigma \quad (4-4)$$

Therefore, the sum A+B is proportional to the change in Poisson's Ratio.

#### 4.1.3 Shear reflectivity: A-B

From Equation (4-1), if we assume  $\frac{V_s}{V_p} = \frac{1}{2}$  (Hilterman, 1989), then:

$$B = \frac{\Delta V_p}{2V_p} - \frac{\Delta V_s}{V_s} - \frac{\Delta \rho}{2\rho} = R_p(0^0) - 2R_s(0^0) \quad (4-5)$$

where :

$$R_p(0^0) = A = \left[ \frac{\Delta V_p}{2V_p} + \frac{\Delta \rho}{2\rho} \right] \text{ and } R_s(0^0) = \left[ \frac{\Delta V_s}{V_s} + \frac{\Delta \rho}{\rho} \right]$$

or:

$$R_s = 0.5(A - B) \quad (4-6)$$

Therefore, the difference A-B is proportional to the shear reflectivity.

#### 4.1.4 Zero angle P and S-wave reflection coefficients

Fatti et al. (1994) remake the two-term Aki-Richards equation as:

$$R_p(\theta) = c_1 R_p(0^0) + c_2 R_s(0^0) \quad (4-7)$$

where:

$$R_p(0^0) = \frac{1}{2} \left[ \frac{\Delta V_p}{V_p} + \frac{\Delta \rho}{\rho} \right] \text{ and } R_s(0^0) = \frac{1}{2} \left[ \frac{\Delta V_s}{V_s} + \frac{\Delta \rho}{\rho} \right]$$

Which gives us a way to calculate P and S-wave reflectivity at zero incident angle -  $R_p(0^0)$  and  $R_s(0^0)$  from seismic data.

#### 4.1.5 Fluid factor

The Castagna (1993) mudrock equation was assumed to be true for non-hydrocarbon filled layers, which is:  $V_p = 1.16V_s + 1360m/s$ .

Smith and Gidlow (1987) and Fatti et al. (1994) derived a fluid factor attribute  $\Delta F$ , based on the above equation, resulting in:

$$\Delta F = \frac{\Delta V_p}{V_p} - 1.16 \left( \frac{V_s}{V_p} \right) \frac{\Delta V_s}{V_s}, \quad \text{or} \quad \Delta F = R_p - 1.16 \left( \frac{V_s}{V_p} \right) R_s \quad (4-8)$$

The fluid factor highlights layers where Castagna's equation is less exact, such as potential hydrocarbon zones.

#### 4.1.6 Lambda-Mu-Rho (LMR)

Goodway et al. (1997) proposed a new approach to AVO inversion based on the Lamé parameters  $\lambda$  and  $\mu$ , and density  $\rho$ , or Lambda-Mu-Rho (LMR).

From 
$$V_s = \sqrt{\frac{\mu}{\rho}} \quad (4-9)$$

and

$$V_p = \sqrt{\frac{\lambda + 2\mu}{\rho}} \quad (4-10)$$

we can derive:

$$\begin{aligned} \mu\rho &= Z_s^2 \\ \lambda\rho &= Z_p^2 - 2Z_s^2 \end{aligned} \quad (4-11)$$

where:  $Z_p$  is P-wave impedance and  $Z_s$  is the S-wave impedance.

Therefore, a cross-plot  $\lambda\rho$  vs  $\mu\rho$  can minimize the effects of density and help to interpret the  $\lambda$  and  $\mu$  attributes; the  $\lambda$  term (incompressibility) is sensitive to pore fluid, whereas the  $\mu$  term (rigidity) is sensitive to the rock matrix.

#### 4.1.7 Theory of AVO modeling

AVO modeling was undertaken to identify the scenarios which generate AVO responses including the seismic velocities, density of the reservoir and pore fluids. The principle of AVO modeling is Gassmann's equations (Gassmann, 1951) which relate the bulk modulus of a rock to its pore, frame, and fluid properties. The equation is given as:

$$K_{sat} = K_{frame} + \frac{\left(1 - \frac{K_{frame}}{K_{matrix}}\right)^2}{\frac{\phi}{K_{fluid}} + \frac{(1-\phi)K_{frame}}{K_{matrix}^2}} \quad (4-12)$$

where,  $K_{sat}$ ,  $K_{frame}$ ,  $K_{matrix}$ , and  $K_{fluid}$  are the bulk moduli of the saturated rock, porous rock frame, mineral matrix, and pore fluid, respectively and  $\phi$  is porosity. In this equation, the shear modulus is independent of pore fluid and held constant during the fluid substitutions.

For not extremely heavy oil, at seismic frequencies and at +20 °C, the shear modulus of heavy oil is negligible and heavy oil acts still like a liquid, In this case, Gassmann's equation can still help us understand the response of heavy oil reservoir (Zhang and Lines, 2007).

The bulk modulus ( $K_{sat}$ ) and shear modulus ( $\mu$ ) at in-situ condition can be estimated from well logs following formula:

$$K_{sat} = \rho(V_p^2 - \frac{4}{3}V_s^2) \quad (4-13)$$

and

$$\mu = \rho V_s^2 \quad (4-14)$$

If there is no  $V_s$  log, the shear velocities can be estimated from the Castagna assumption.

From the mineral composition of the rock, we can calculate the modulus of the mineral matrix. Similarly, we can obtain the bulk modulus and density of the pore fluid. Then,  $K_{frame}$  can be estimated from Equation (4-12). Therefore, if we change the fluid content of the reservoir and estimate the bulk modulus and density of desired fluid, we can substitute these values into Equation (4-12) and calculate the new bulk modulus and velocities of the saturated rock after fluid substitution.

## 4.2 Field data inversion and AVO attributes analysis

### 4.2.1 Geological background of studied area

The formation studied is a heavy oil reservoir in Canada. It was deposited as prograding tide-dominated deltas and composed of 3 stacked incised valleys. These incised valleys lie encased within more regional deltaic, shoreface sands and marine muds. Total thickness of the formation is 50-75 meters (Hein et al., 2007) and it is an important resource of 9-10 API bitumen. The field is actively produced by steam assistant gravity drainage (SAGD).

The well logs in this area are shown in Figure 4-1. Figure 4-1a shows logs from the studied well which is 200 m away from the VSP borehole. In the reservoir zone, the gamma ray values are low which indicates clean sand deposits. High porosity and low density in these zones also indicate a good hydrocarbon reservoir. Figure 4-1b shows the resistivity logs from a nearby well which is about 500 m away from the VSP borehole. High resistivity values between 440 – 480 m indicate bitumen zone while lower values of resistivity below the bitumen zone indicate bottom water. The oil water contact is recongized around 480 m.

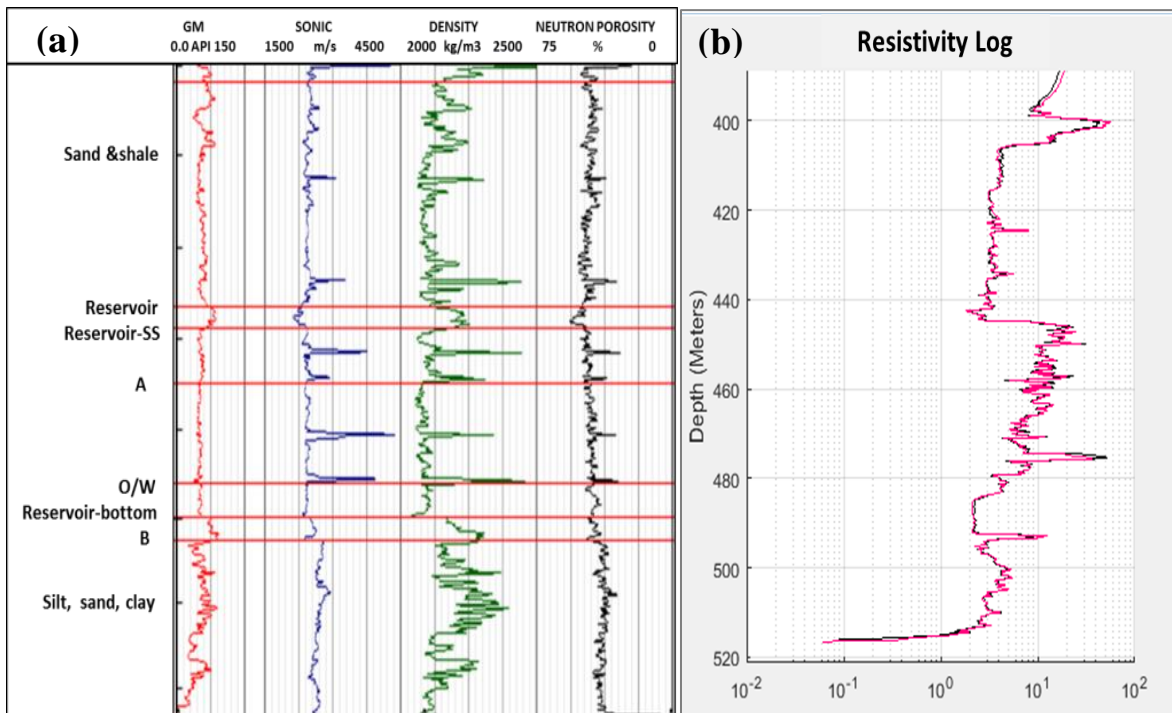


Figure 4-1. (a) Logs from the target reservoir. From left to right, the logs are gamma ray, sonic, density and neutron porosity respectively. (b) Resistivity logs from a nearby well. Red curve is the shallow induction resistivity log (10 inch) and black curve is the deep induction resistivity log (90 inch). Decreased resistivity around depth 485 m indicates oil water contact.

#### 4.2.2 Inversion analysis

Figure 4-2 shows a statistical wavelet extracted from processed VSP data and Figure 4-3 shows correlation of VSP trace with the synthetic seismogram. In Figure 4-3, the correlation analysis window is in the reservoir zone (430-510 ms); the red traces are VSP data close to the well location and the blue traces are the synthetic seismogram. The VSP and synthetics show excellent alignment. Figure 4-4 shows poststack inversion analysis. From left to right, the columns are impedance log, statistical wavelet, synthetic and seismic traces, followed by the error between the synthetic seismogram and the seismic data. Small errors indicate reliable inversion result. Figure 4-5 shows inverted P-impedance. The reservoir is highlighted by a blue rectangle. The shale/sand contact at the reservoir top (around 440 ms) shows high impedance whereas inside the reservoir, the impedance is lower. The base of reservoir (490 ms) shows decreasing impedance while further below the base of the reservoir, the impedance is higher.

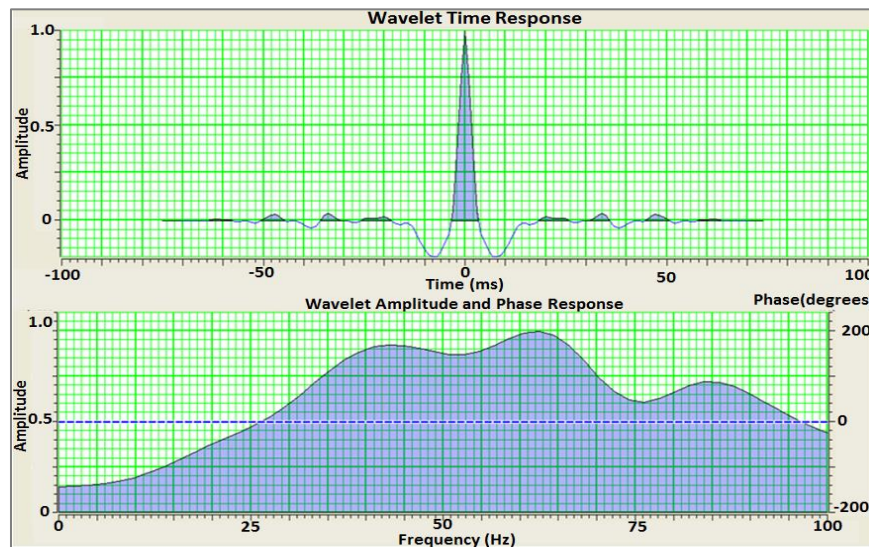


Figure 4-2. Statistical wavelet extracted from processed VSP data.

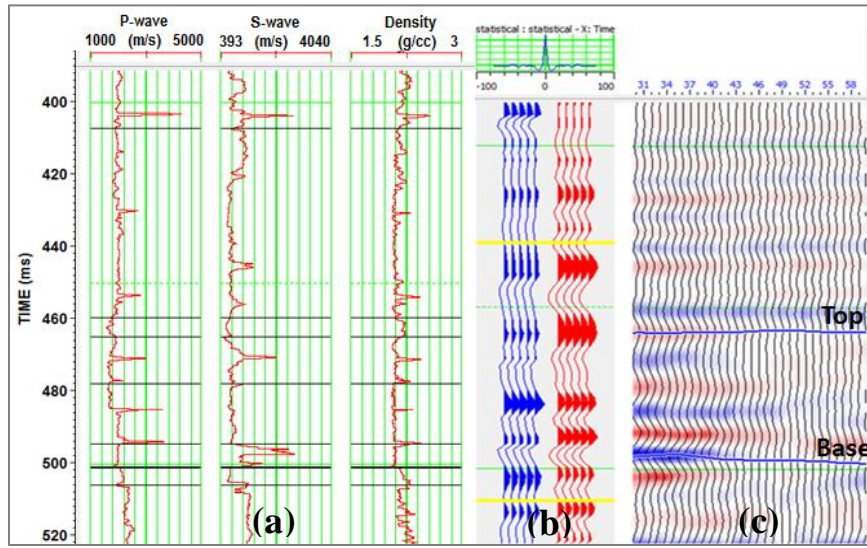


Figure 4-3. Correlation between VSP trace and synthetic seismogram. (a) P-wave, S-wave velocity and density logs, (b) synthetic traces (blue) and VSP traces (red) at well location, (c) VSP data.

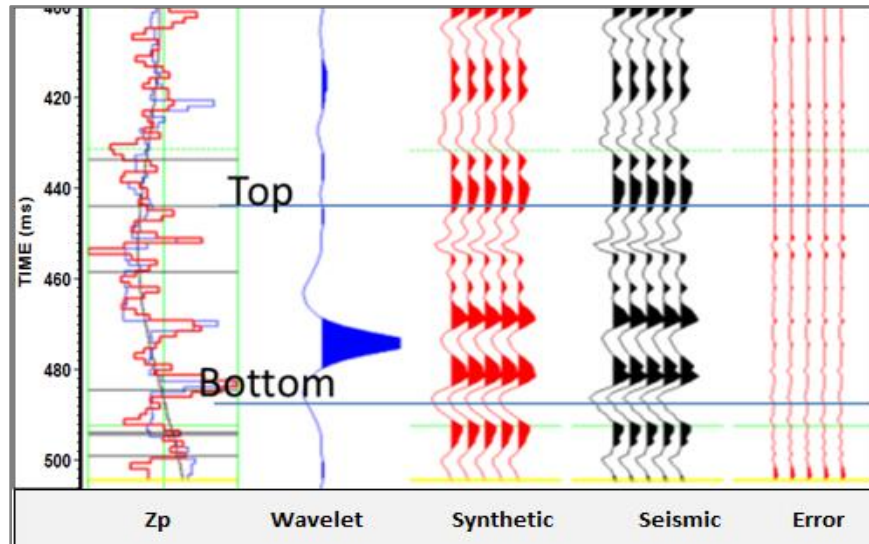


Figure 4-4. Inversion analysis. From left to right, are impedance log, statistical wavelet, synthetic and seismic traces, and the error between synthetic and seismic. For the impedance logs, the blue curve is impedance from original P-wave velocity and density log, the black curve is the original model, and the red is impedance log from the inversion.

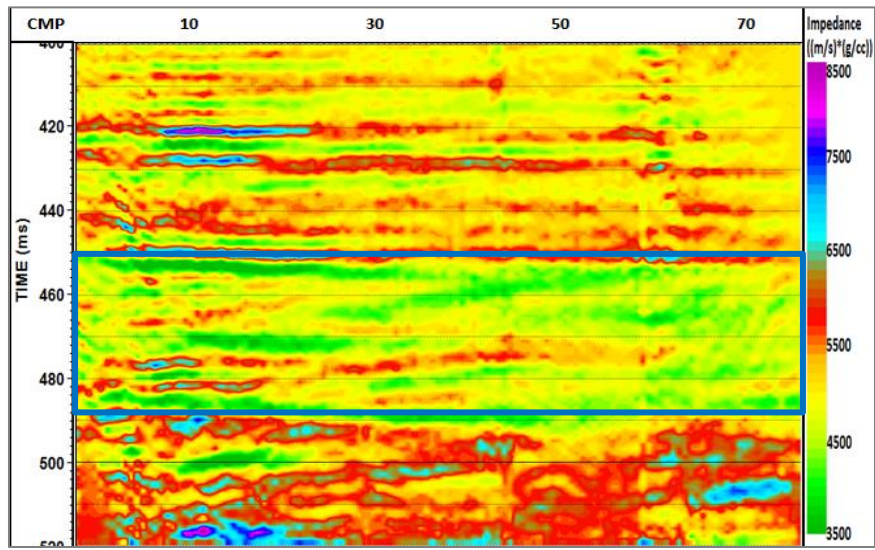


Figure 4-5. Inverted P-impedance. Reservoir is highlighted by the blue rectangle.

Pre-stack inversion is a generally non-unique process. This means there are many geological solutions consistent with the input seismic data. To reduce the non-uniqueness, the inversion software (Hampson - Russell was used in this study) provides a background trend relating the variables  $Z_p$ ,  $Z_s$ , and density derived from the well logs. In the absence of hydrocarbons, there is an approximately linear relationship between these variables. The inversion then looks for deviations from these linear trends. Figure 4-6 show the  $Z_s$  vs  $Z_p$  and density vs  $Z_p$  crossplot on the log-log scale.

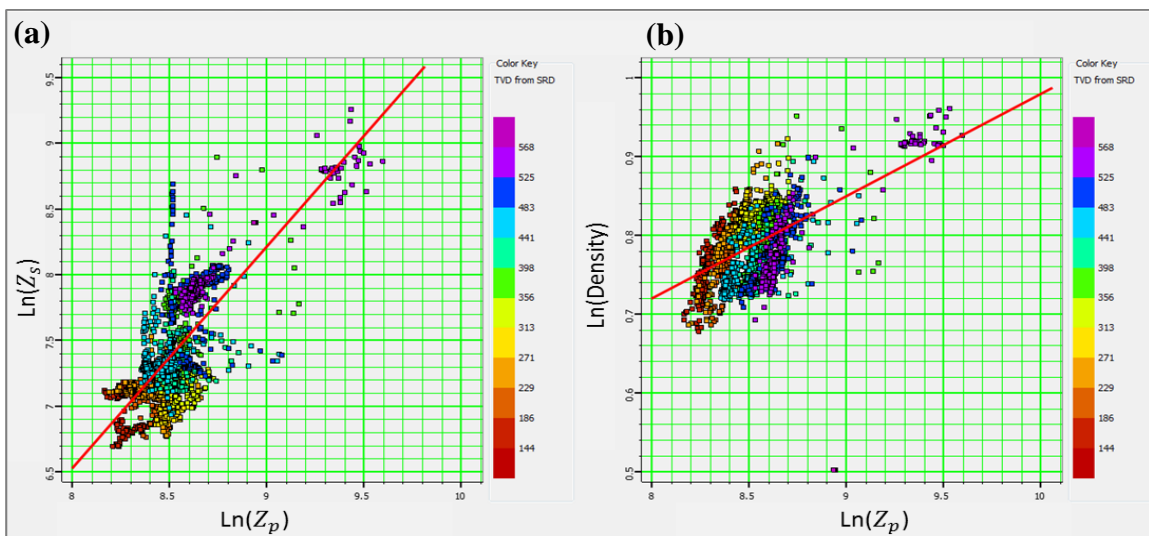


Figure 4-6. (a) Plots of  $Z_s$  vs  $Z_p$  and (b) density vs  $Z_p$  on a log-log scale. The red lines indicate the current linear trend.

Figure 4-7 shows the pre-stack inversion analysis result. Figure 4-7a shows the inversion results (in red) of  $Z_p$ ,  $Z_s$ , Density,  $V_p/V_s$  separately overlaying the original logs from the well (in blue), and the black curves are original models. Figure 4-7b is the input wavelet. Figure 4-7c to Figure 4-7e are synthetic traces calculated from this inversion (in red), followed by the original VSP angle gather (in black), and errors between the synthetic seismogram from the inversion and the seismic data respectively. Comparing to post-stack inversion analysis, the error in pre-stack inversion is larger. This may due to errors in estimated S-wave velocities. The well logs used in inversion were logged in the 1980's without any S-wave velocity. Alternatively, in this work, the S-wave velocity was calculated by using the  $V_p/V_s$  from a nearby well which is 500 m away from the VSP borehole. Figure 4-8 shows the inverted P and S-impedance. P-impedance is close to the post stack inversion result while S-wave impedance doesn't show obvious changes at the top of reservoir due to small changes of density and shear wave velocity, but it shows increasing of S-impedance at bottom of the studied interval.

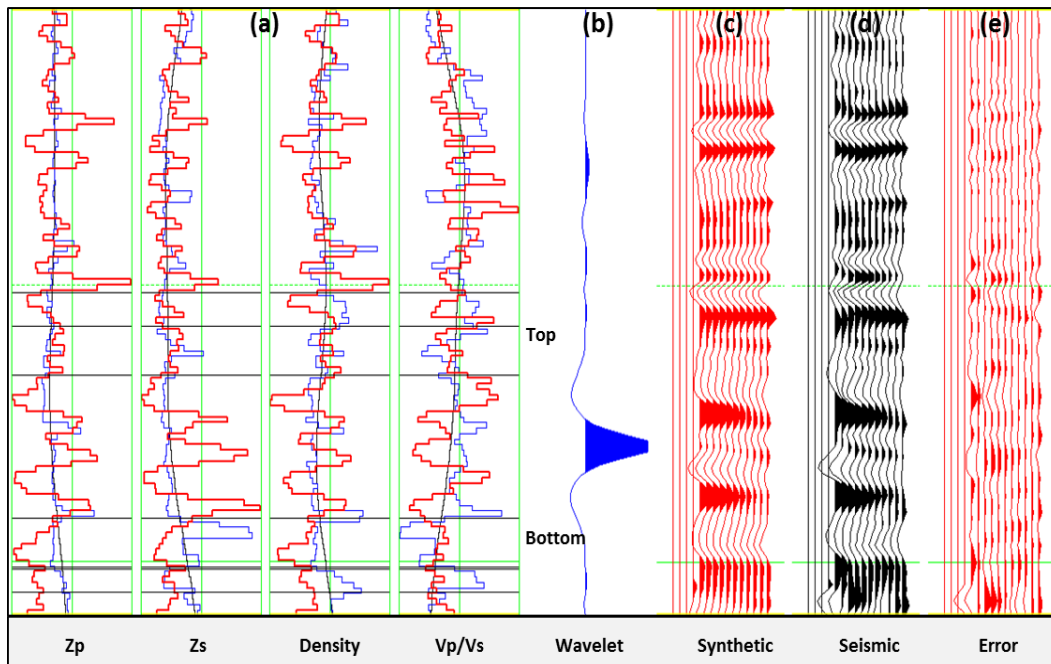


Figure 4-7. Prestack inversion analysis. (a) The inversion results (in red)  $Z_p$ ,  $Z_s$ , Density,  $V_p/V_s$  separately overlaying the original logs from the well (blue), black curves are original models; (b) statistic wavelet; (c) synthetic traces; (d) VSP angle gather; (e) errors between inverted synthetic and seismic.

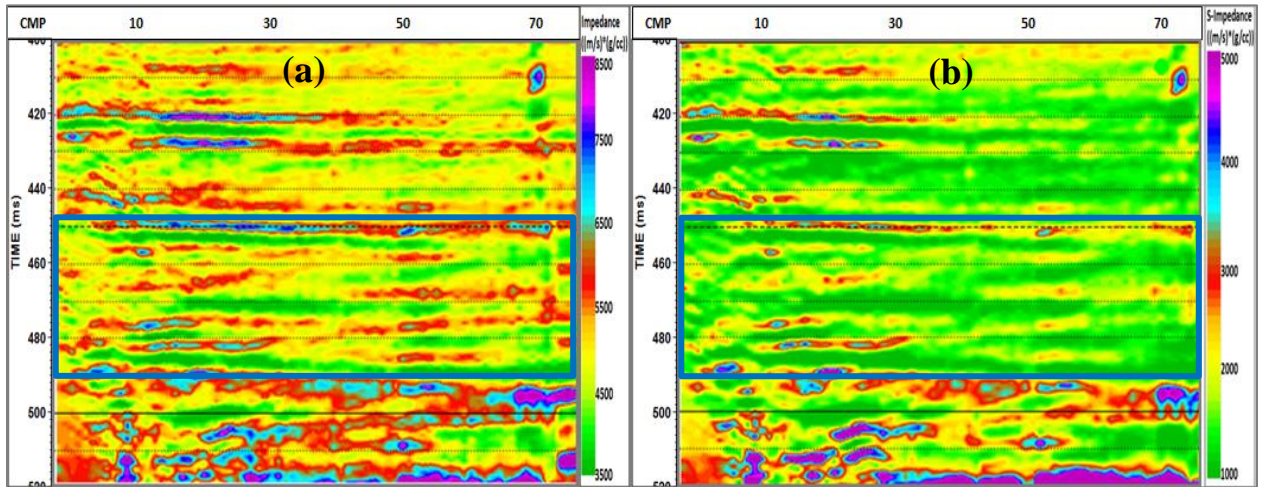


Figure 4-8. (a) Inverted P-wave impedance and (b) S-wave impedance. Reservoir is highlighted by the blue rectangle.

Figure 4-9 is S-impedance vs P-impedance crossplot. The samples from the reservoir top are highlighted by a red ellipse while the samples from the bottom of the reservoir are highlighted by a yellow ellipse. Apparently, the reservoir bottom has higher  $Z_s/Z_p$ . The crossplot canceled out the effect of density (assume density has negligible changes) therefore, it is reciprocal of  $V_p/V_s$  which is higher at top of reservoir and lower at bottom of reservoir and they both follow an approximately linear trend. The decrease in  $V_p/V_s$  indicates possible saturation of hydrocarbon. Figure 4-10 shows the inverted density and  $V_p/V_s$ . Density doesn't show much variation inside the reservoir whereas  $V_p/V_s$  does. Above and at the top of reservoir (450 ms), the  $V_p/V_s$  values are relatively high (blue) while at the base of reservoir, the  $V_p/V_s$  values are low (yellow). The results are consistent with observations of  $Z_s$  vs  $Z_p$  crossplot (Figure 4-9).

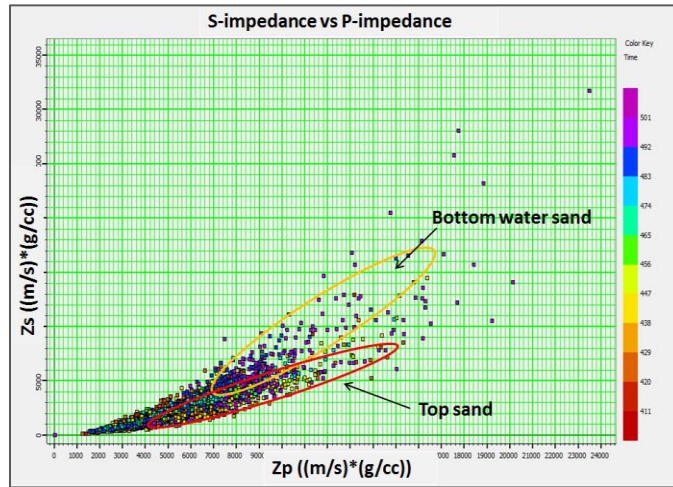


Figure 4-9. S-impedance vs P-impedance crossplot.

$V_p/V_s$  is also a good indicator of the sand and shale distribution. Based on the Greenberg and Castagna (1992) definition of  $V_p/V_s$  for commonly occurring lithologies, sand has a slightly lower  $V_p/V_s$  than shale. Therefore, the entire reservoir zone (sand, 450-500 ms) shows lower values of  $V_p/V_s$  which indicates a lithology change (shale to sand). With the presence of water or oil, the  $V_p/V_s$  decreases. The bottom of reservoir shows the lowest value of  $V_p/V_s$ . If gas is present, the  $V_p/V_s$  is even lower than for wet sands. We need to combine other information to eliminate the ambiguities and obtain a valid prediction. In Figure 4-10, the density section doesn't show obvious lateral variations but  $V_p/V_s$  does which indicates a lateral change of reservoir lithology or fluid.

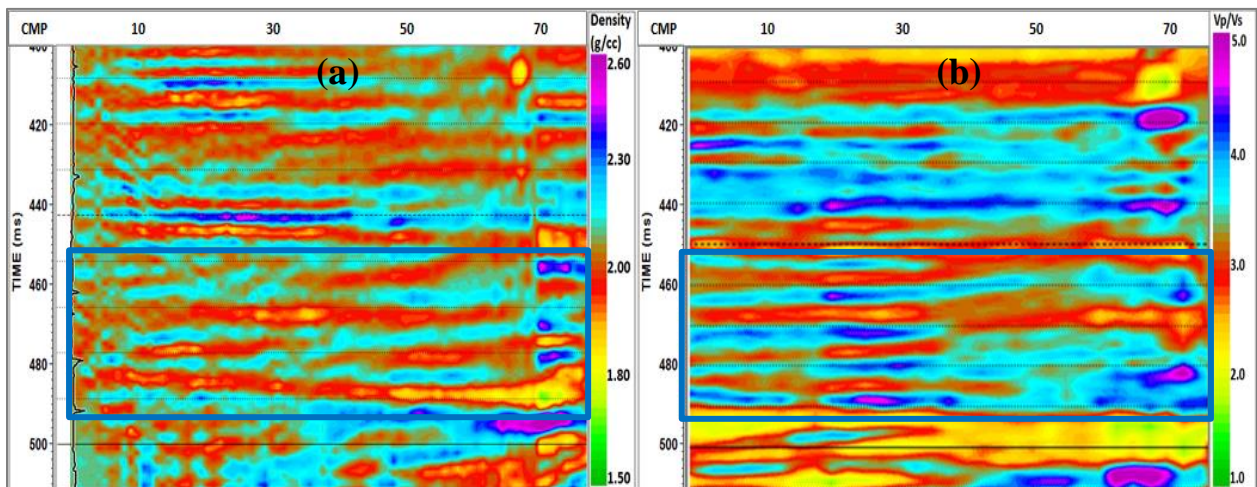


Figure 4-10. (a) Inverted density and (b)  $V_p/V_s$ . The reservoir is highlighted by the blue rectangle.

P-wave impedance vs Vp/Vs crossplot (Figure 4-11) shows the top and bottom trend of the studied reservoir. Most of the values from the reservoir top (shale-sand contact, yellow and orange dots) are located in the low impedance but high Vp/Vs zone while the bottom of reservoir (sand-shale contact, purple dots) shows high P-impedance but low Vp/Vs. The analysis is also consistent with observations discussed above (Figure 4-8 to Figure 4-10). The crossplot also makes easier for us to identify the gas effects. If there is a gas effect, it should compose to low P-wave impedance and low Vp/Vs zone (left bottom corner, marked by blue circle). Apparently, in our target reservoir, does not show gas effects.

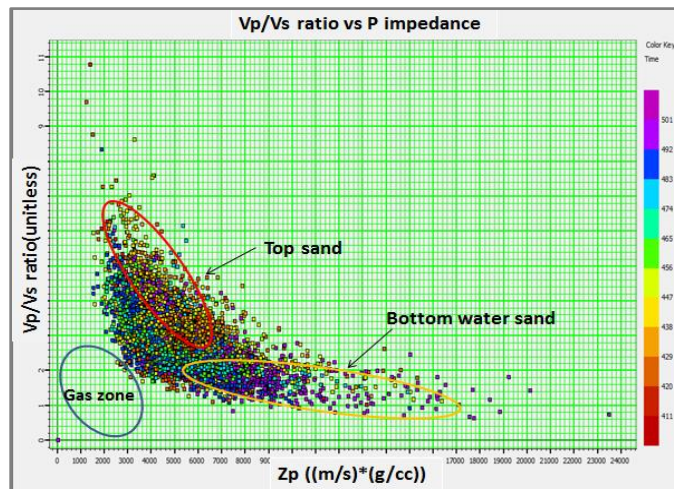


Figure 4-11. P-wave impedance vs Vp/Vs crossplot.

#### 4.2.3 AVO analysis

As introduced in Chapter 2, the processed far offset shots were used to create a gather for inversion. A reflectivity gather was also produced for AVO analysis. The workflow is shown in Figure 4-12. Firstly, a scalar was calculated from downgoing waves and applied to upgoing waves. Next, the upgoing wave amplitude is divided by the downgoing wave amplitude to obtain the reflectivity. Then, the entire gather was stacked into one trace. In order to improve the signal-to-noise ratio and obtain a more accurate reflectivity, a corridor mute (30 ms window) was applied to the shot gather before stacking. Then all of the shot stack traces were merged to obtain an offset reflectivity gather for AVO analysis.

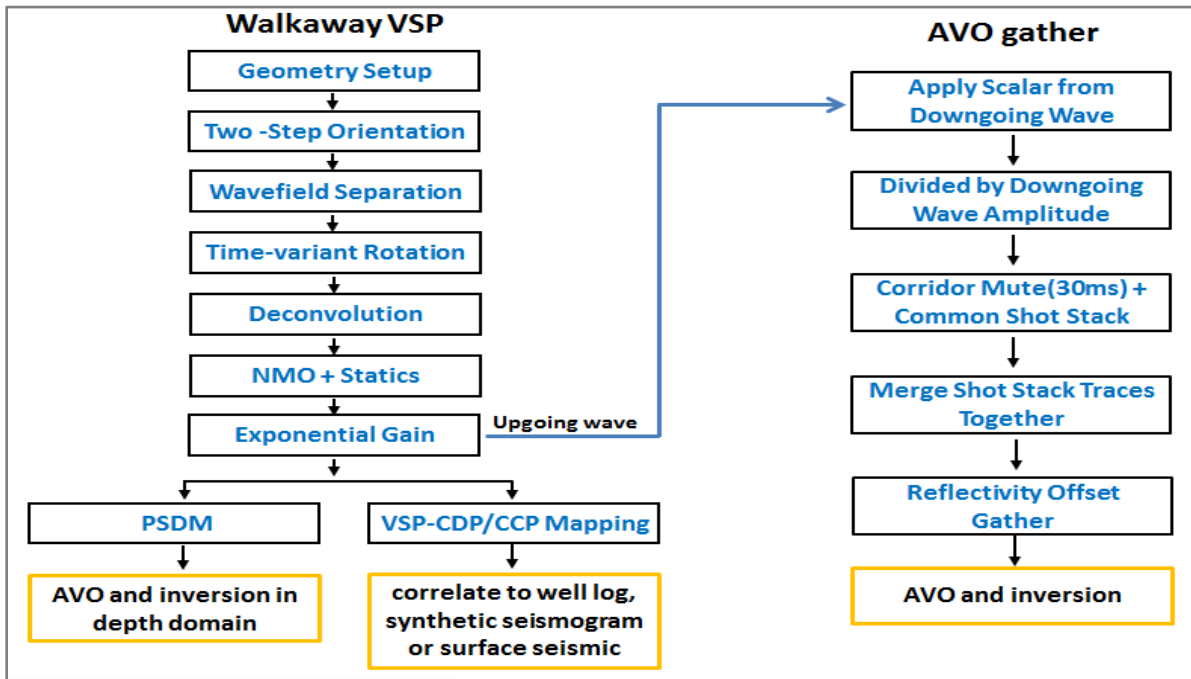


Figure 4-12 Workflow to produce offset reflectivity gather for AVO analysis.

Figure 4-13a shows the correlation between the reflectivity gather and the synthetic seismogram around the reservoir zone. The seismogram was created using the CREWES tool Syngam. The top and bottom of the target reservoir show good correlation while, inside the reservoir, the amplitude and phases of the VSP data show some differences from the synthetic seismogram. The distance between logged well and VSP borehole is one of the possible reasons for this mis-tie. In addition, the well was logged in the 1980's before steam injection, therefore, we expect to see reservoir changes after steaming and production. The AVO responses of the target reservoir are shown in Figure 4-13b. Overall, the amplitudes picked from the VSP and the synthetic seismogram at the top and bottom of the reservoir display a similar trend within an offset range of 0 to 600 m. At the top, the amplitudes are positive and decrease with offset, whereas at the bottom, the amplitudes are negative but also decrease with offset.

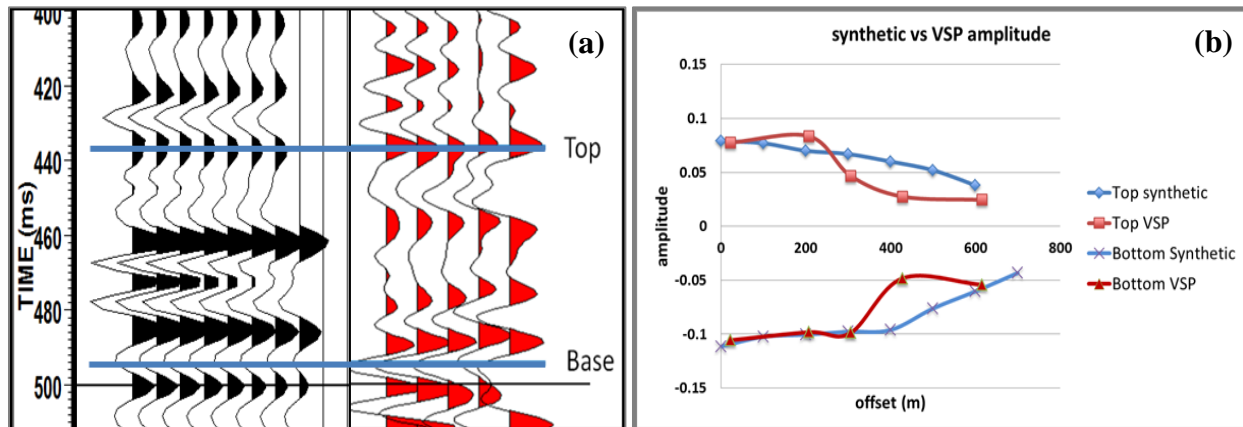


Figure 4-13. (a) Tie of synthetic offset gather (shown in black) and reflectivity gather (shown in red). Top and bottom of the target reservoir are picked and highlighted by blue lines. (b) AVO responses at top and base of the studied reservoir. Red lines are amplitudes from the VSP and blue lines are amplitudes from the synthetic seismicogram.

Next the AVO gather was transformed to angle gather to do AVO attributes analysis in Hampson-Russell software (Figure 4-14). Red squares are amplitudes extracted from VSP angle gather and solid lines are plots of Aki-Richard two-term equation. The fit of the AVO curves is very good. At the top and bottom of the reservoir, amplitudes of the VSP data decrease with incident angle which is the same trend as seen in synthetic seismic data. The top interface falls into Class I AVO response while the base falls into Class IV responses.

Figure 4-15 shows AVO attributes derived from the angle gather at the VSP well location based on two-term Aki-Richards equation. It shows the intercept A (Figure 4-15a), gradient B (Figure 4-15b), AVO product A\*B (Figure 4-15c), scaled Poisson's ratio change (Figure 4-15d), and scaled S-wave reflectivity (Figure 4-15e) separately. At the top of reservoir (440 ms, Sand), the intercept is positive while at the bottom of reservoir (495 ms), the intercept is negative. The gradient value is small in the entire study zone. The AVO product is “dim” or “negative” responses (or close to zero values). The scaled Poisson's ratio change is negative (green) at top which indicates a drop in Poisson's ratio and positive (yellow) at the bottom of the reservoir, indicating an increase in Poisson's ratio. The scaled S-wave reflectivity is positive at the top but negative at the bottom of the reservoir. All of those properties help to identify the AVO classes and potential gas anomalies.

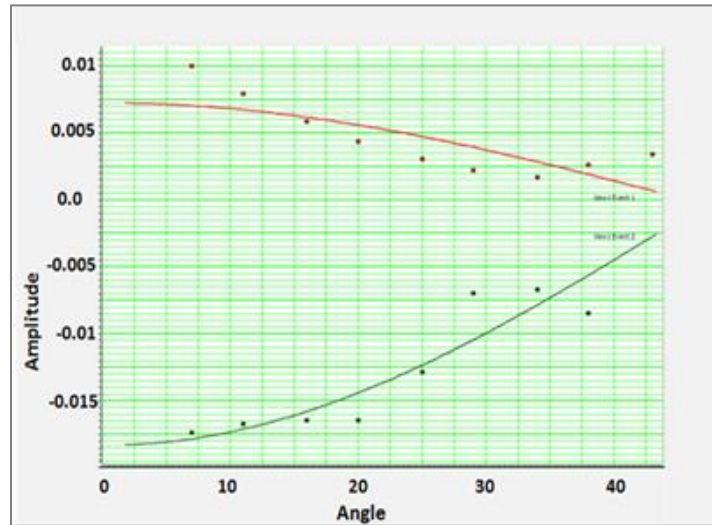


Figure 4-14. Gradient curve. Dots curves are amplitudes measured from VSP gather and solid lines are amplitudes measured from synthetic seismogram. Red curve and dots are from the top of the reservoir and green curves and dots are from the bottom of the reservoir.

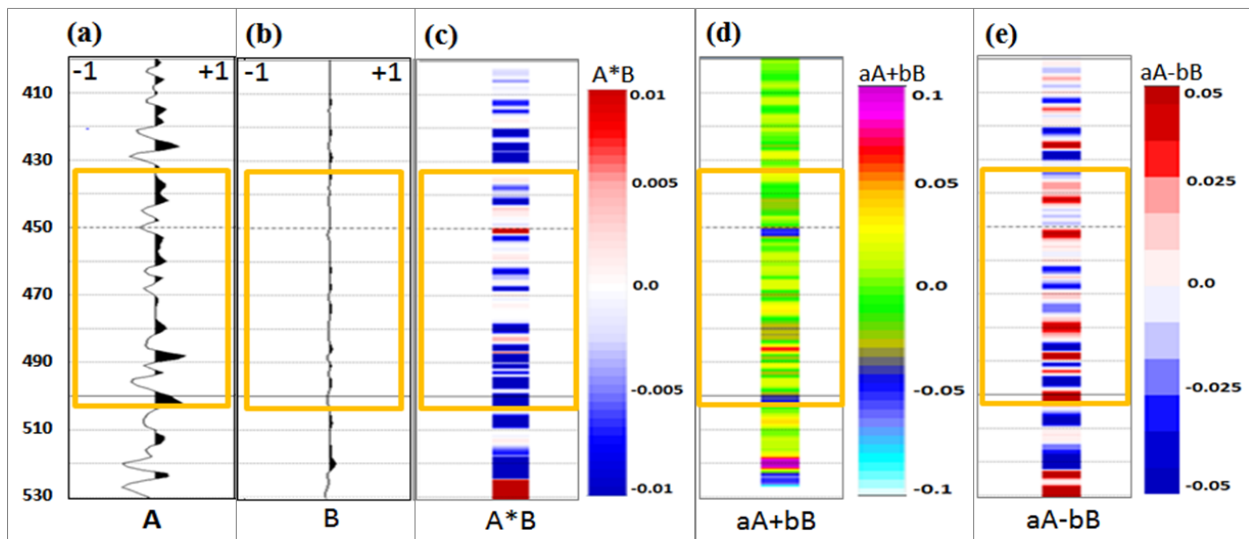


Figure 4-15. AVO attributes derived from the angle gather at the VSP well location from the two-term Aki-Richards method (angle gather is up to 42 degree). (a) Intercept A, (b) gradient B, (c) AVO product  $A*B$ , (d) scaled Poisson's ratio change ( $aA+bB$ ), and (e) scaled S-wave reflectivity ( $aA-bB$ ). Reservoir is highlighted by the yellow rectangle.

The two-term Fatti equation yields other attributes and a more accurate S-wave reflectivity which is shown in Figure 4-16. Both  $R_{p0}$  and  $R_{s0}$  are positive at the top of reservoir and negative at the base of reservoir. Inside the reservoir, I observe large decrease in P-wave reflectivity while less change of S-wave reflectivity. Low values (anomalies) of fluid factor show small deviation

from the mudrock trend at the top and bottom of reservoir (close to zero). It indicates no gas effects at the well location.

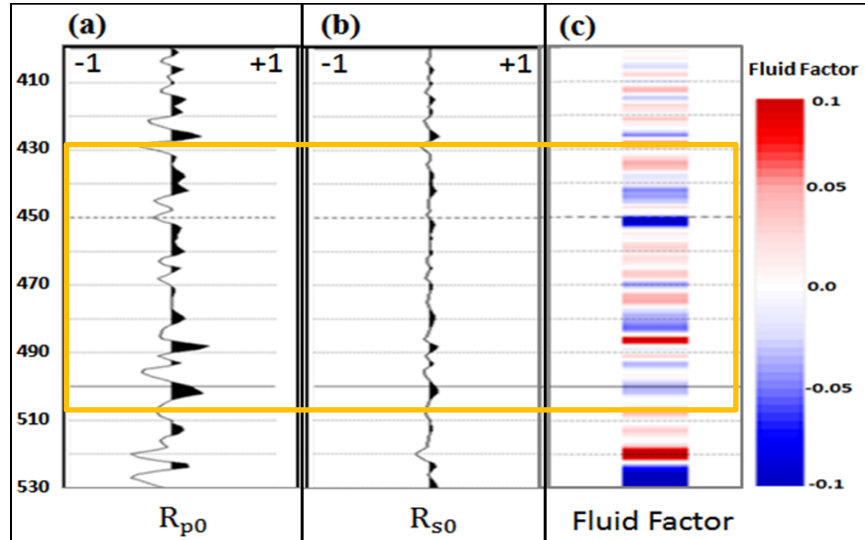


Figure 4-16. (a) P-wave reflectivity  $R_{p0}$ , (b) S-wave reflectivity  $R_{s0}$  from two-term Fatti's method, and (c) derived fluid factor at  $V_p/V_s=2.0$ . Reservoir is highlighted by the yellow rectangle.

From the analysis above, in the studied reservoir, the shale-sand interface has a positive impedance change and negative Poisson's ratio change, which giving a negative AVO gradient (class I response). At the base of the reservoir, the impedance decreases but Poisson's ratio is increasing due to existence of water in pore space (Carcione and Cavallini, 2002), which is a Class IV AVO response. All the parameters are summarized and listed in Table 4-2.

Table 4-2. Properties of studied reservoir

Reservoir	Top	Base
Interface	shale-sand	sand-shale
Impedance change	+ve	-ve
Amplitude	+ve	-ve
Amplitude change	Decreases with offset	Decreases with offset
Poisson's ratio change	Decrease	Increase
AVO classification	I	IV
	Wet sand, no gas response	

Similarly, I derived AVO attributes from the CMP gathers of the entire VSP survey and they are shown in Figure 4-17 to Figure 4-23. All the attributes show similar signatures at the well location as the attributes from single CMP discussed above but they also display lateral variations along the shot was away from the well.

In the studied reservoir, at the top, the intercept A represents zero-offset reflection coefficient shown in Figure 4-17a. It is positive (red) at top and negative (blue) at bottom (blue). While gradient B (Figure 4-17b) is negative (blue) at top but positive (red) bottom. The A vs B crossplot (Figure 4-18) shows all the samples inside the reservoir are distributed along the linear wet trend ( $V_p/V_s=2.0$ ) which indicates no gas anomaly.

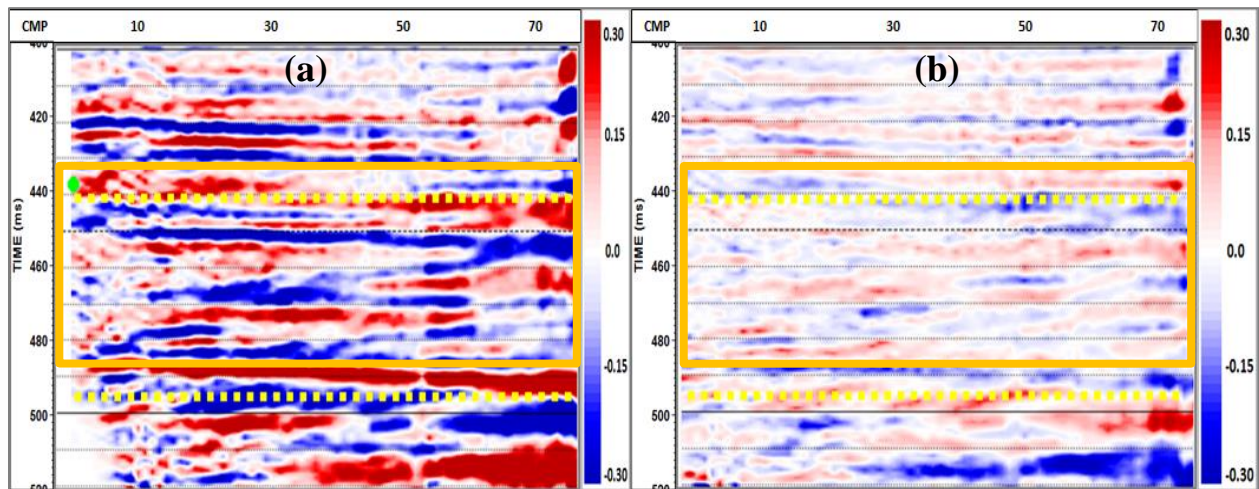


Figure 4-17. (a) Intercept A and (b) gradient B from Aki- Richards equation. The reservoir zone is highlighted by the yellow rectangle.

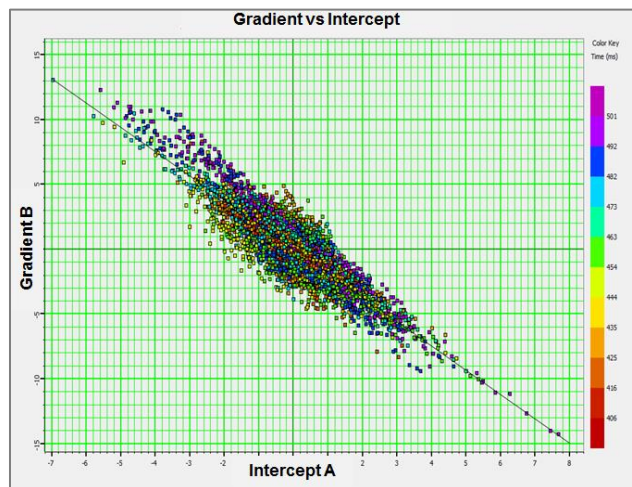


Figure 4-18. A vs B crossplot. Small deviation from wet trend line ( $V_p/V_s=2.0$ ) indicates no gas anomaly.

Figure 4-19a shows the AVO product  $A*B$ . Negative AVO product values indicate decreasing amplitude with offset, which is a Class I or Class IV response. Around the CDP 30, between 450-460 ms and the CDP 70, between 470-490 ms, the weak red colour zones (highlighted by red ellipses) indicate potential thin Class II or Class III AVO effects which both show increasing amplitude with offset. The positive AVO product can be a soft marker for hydrocarbons. Figure 4-19b shows a decreasing trend in Poisson's ratio change (green to orange) at the top of reservoir while increasing in Poisson's ratio change at the bottom of reservoir. Responses from both top and base of the reservoir are highlighted by pink dotted lines.

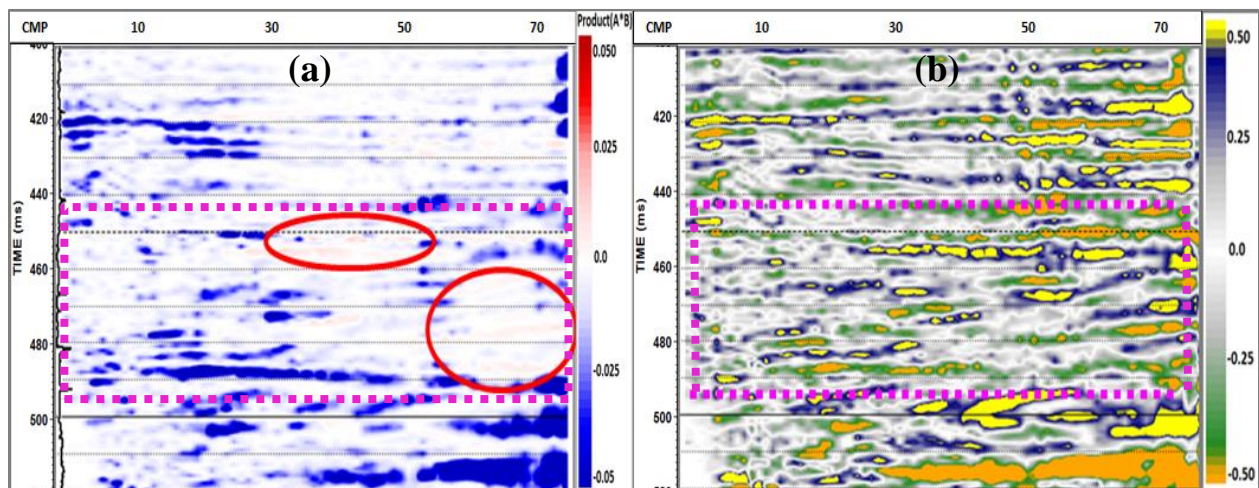


Figure 4-19. (a) AVO product  $A*B$  and (b) scaled Poisson's ratio change. The target reservoir is highlighted by a rectangle.

Figure 4-20 shows an  $R_p$  vs  $R_s$  crossplot which is derived from the Fatti equation. It is seen that samples from the reservoir follow similar trends but show a small difference in slope. The two trends are highlighted by the red and yellow dotted lines. Samples along red line are mostly from the top of reservoir and samples along yellow line are mostly from the bottom of the reservoir. The different slopes indicate the top has lower  $R_p/R_s$  than the bottom of the reservoir.

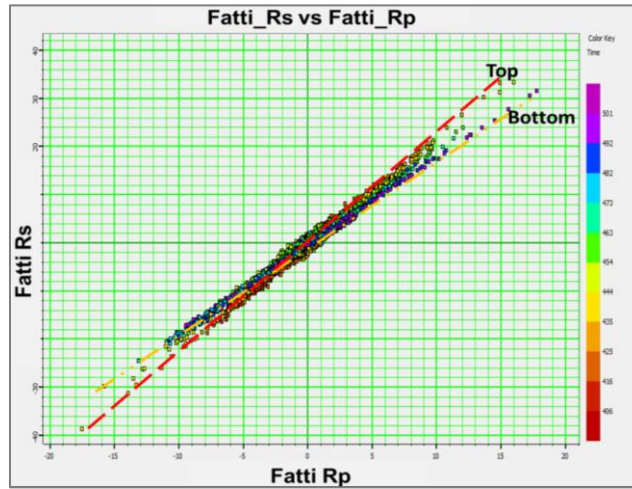


Figure 4-20. Rp vs Rs crossplot. Samples from the reservoir top show lower Rp/Rs than the samples from the bottom of the reservoir.

As inputs of poststack inversion,  $Z_p$  and  $Z_s$  can be derived from  $R_p$  and  $R_s$  which are shown in Figure 4-21. The inverted impedances show similar signatures as the post-stack and pre-stack inversion results (Figure 4-5 and Figure 4-8). Figure 4-21a shows inverted  $Z_p$ . Inside the reservoir, P-impedance is lower than overlying and overlain layers. Figure 4-21b shows the inverted S-impedance. At the top of the reservoir, there is not a big difference in S-impedance above and below the shale-sand interface. But at the bottom of the reservoir, the sand-shale contact shows as obvious increase of S-impedance. Figure 4-22 is  $Z_s$  vs  $Z_p$  crossplot. The crossplot shows that the top sand has higher  $Z_p/Z_s$  and bottom water sand has lower  $Z_p/Z_s$ . Inside the reservoir, sand samples show both low  $Z_p$  and  $Z_s$ .

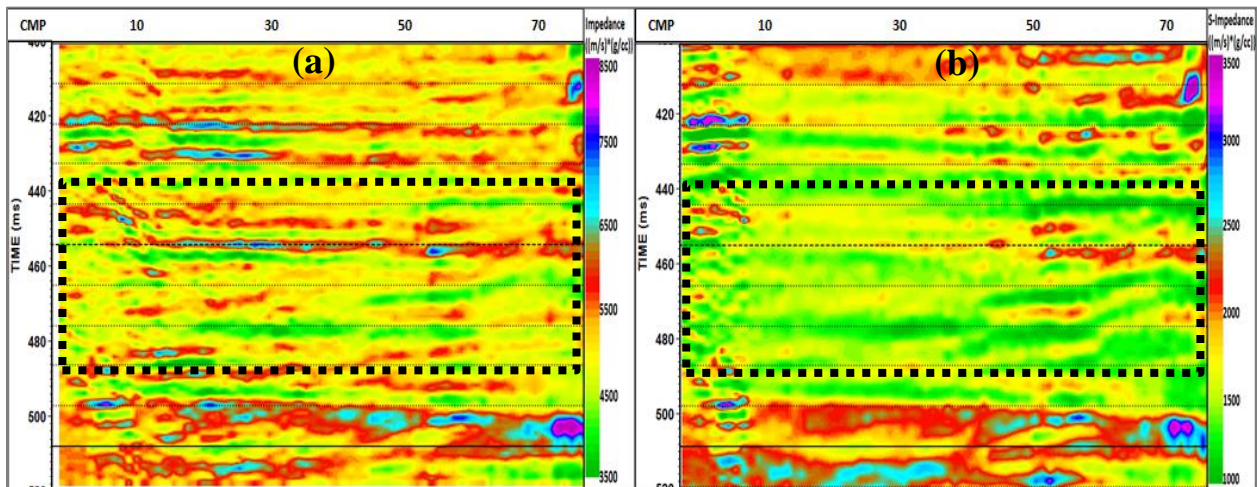


Figure 4-21. (a) Inverted  $Z_p$  and (b)  $Z_s$  from  $R_p$  and  $R_s$ . The reservoir zone is highlighted by a rectangle.

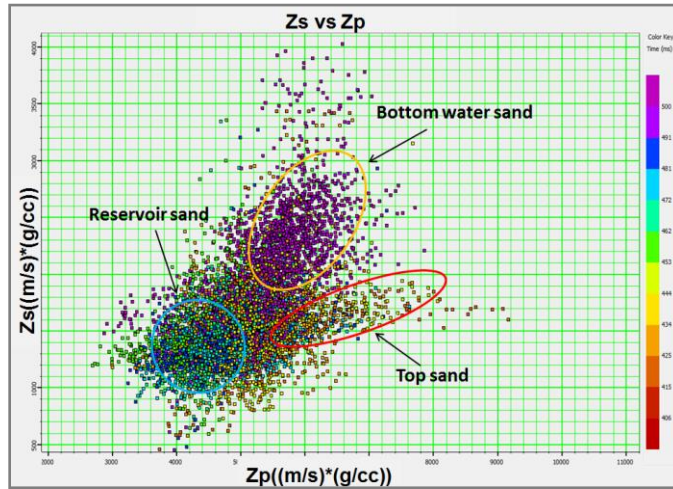


Figure 4-22. Inverted  $Z_p$  vs  $Z_s$  crossplot. The top sand has higher  $Z_p/Z_s$  than the bottom water sand. Inside the reservoir, sand samples show both low  $Z_p$  and  $Z_s$ .

Figure 4-23 shows samples of the VSP angle gather and the fluid factor inverted from the gather. Those angle gathers are at CDP 35 to 41 and the incident angles are from 0 to 42 degree (Figure 4-23a). The fluid factor shows near to zero values at the well location but increasing deviation along the increasing distance from the VSP borehole. This may indicate potential hydrocarbon in far offset locations (Figure 4-23b).

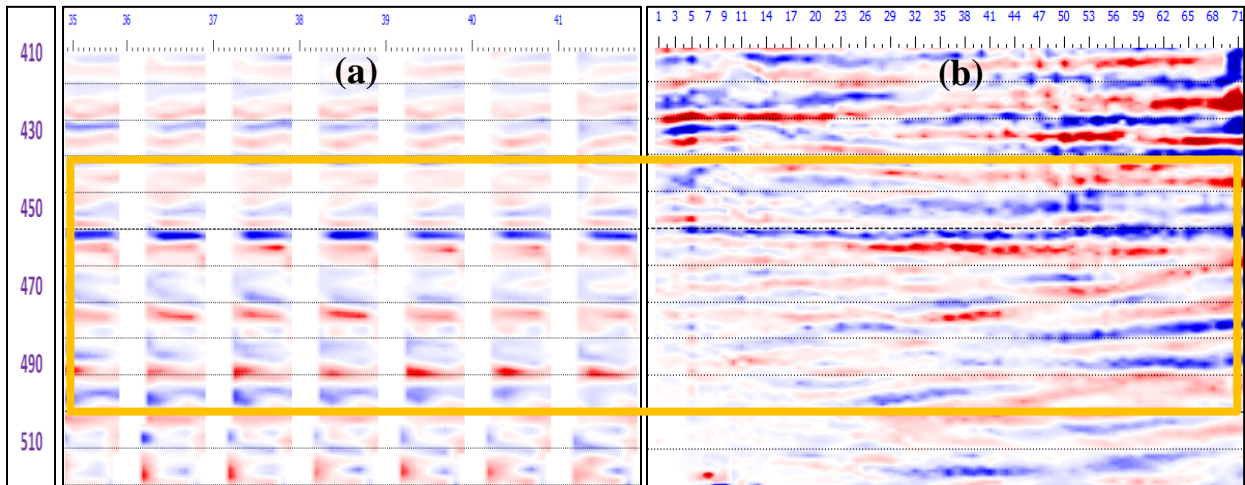


Figure 4-23. (a) Angle gathers at CDP 35 to 41. Incident angles are from 0 to 42 degree. (b) Fluid factor ( $V_p/V_s=2.0$ ) inverted from the two-term Fatti equation. The reservoir is highlighted by a yellow rectangle.

#### 4.2.4 AVO LMR analysis

Inverting the  $R_p$  and  $R_s$ , the Lambda Rho (LR) and Mu Rho (MR) can be obtained which are shown in Figure 4-24. If there is gas effect, we expect to see a significant decrease in LR volume and a slight increase in MR volume. Figure 4-24 doesn't indicate gas presents.

Crossplot of LR and MR (Figure 4-25) can minimize the effects of density and help to interpret the  $\lambda$  and  $\mu$  attributes: the  $\lambda$  term (incompressibility) is sensitive to pore fluid, therefore is an indicator of water vs gas saturation; whereas the  $\mu$  term (rigidity) is sensitive to rock matrix and is used to help pure rock fabric or lithology (Chopra, et al., 2003). In Figure 4-25, the samples highlighted by the yellow rectangle have negative  $\lambda\rho$  value which is caused by noise. The red rectangle zone could be potential gas zone with low  $\lambda$  but high  $\mu$ . Since there are only few samples in this area, it appears that there are no gas effects in the reservoir. However, convincing cluster patterns can be seen in this crossplot. For example, samples from the overlying shale are highlighted by grey circle with low compressibility and low rigidity; samples from the top of reservoir (sand) are highlighted by the red ellipse show slightly higher incompressibility and rigidity; samples from the reservoir sand are highlighted by blue ellipse which show very low incompressibility and rigidity; samples from the bottom water sand are highlighted by yellow circle which show similar incompressibility as top reservoir but slightly higher rigidity. This example demonstrated that the LMR is an effective tool to predict lithology and fluid in the reservoir.

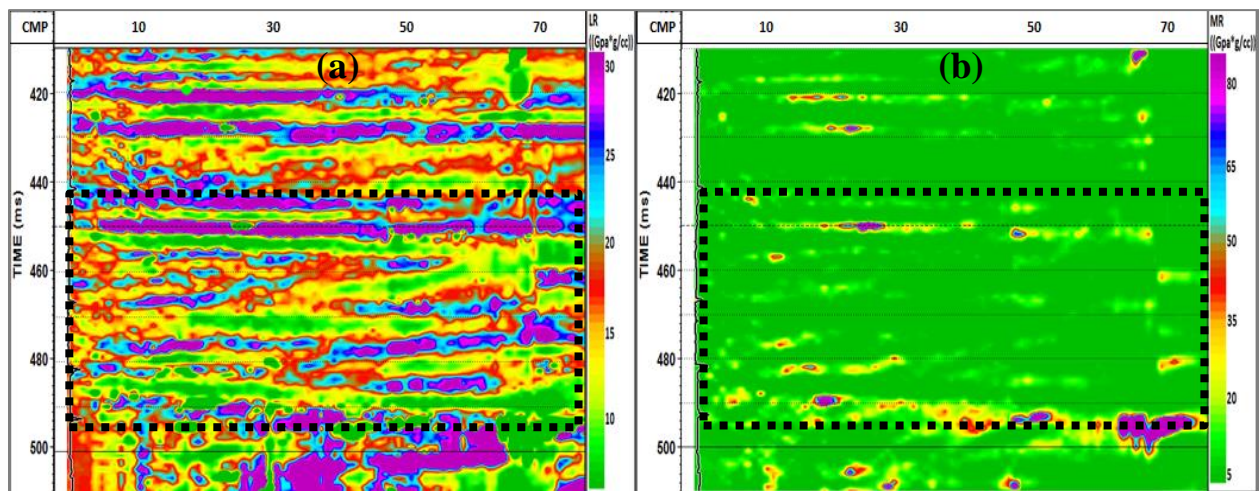


Figure 4-24. (a) Inverted Lambda Rho and (b) Mu Rho. The reservoir is highlighted by a rectangle.

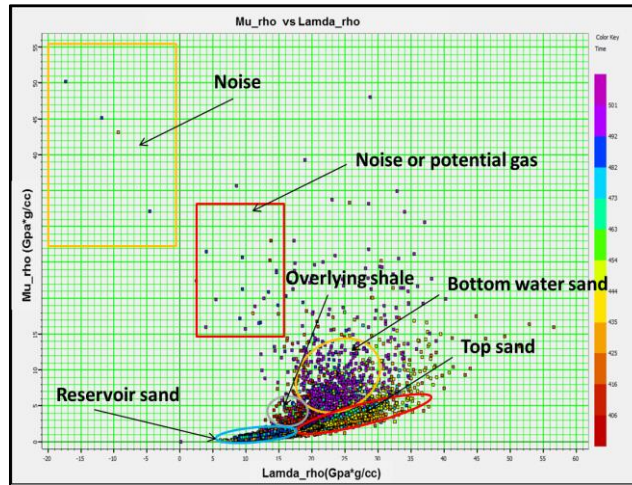


Figure 4-25. Mu-rho vs Lambda-rho crossplot. Lithology and fluid changes in the target reservoir were identified through the LMR analysis.

#### 4.2.5 AVO modeling

As I introduced before, the  $V_p/V_s$  data were taken from an adjacent well which is approximately 500 m away from the VSP well. Then S-wave velocities and Poisson's ratio were calculated based on the  $V_p/V_s$  from this other well. Also, the S-wave velocity and Poisson's ratio were estimated by AVO modeling and compared to calculated values. The two methods gave consistent results.

I modeled different fluid combinations based on the Biot-Gassmann's equation. Figure 4-26 and Figure 4-27 show AVO modeling results. Figure 4-26 shows modeled logs. Logs in different colours were estimated from different scenarios. Blue curves represent pure brine, pink curves represent pure oil and yellow curves represent pure gas scenario. Black curves are from 80% brine, 15% oil and 5% gas scenario. Pure oil responses (pink) are very close to pure brine (blue) and original logs (red). With pure gas (yellow curves), P-wave, density and Poisson's ratio all show huge deviation from original logs. In addition, the modeled mixed gas scenario (black) also shows dramatically decrease of P-wave velocity and big change of Poisson's ratio even if only 5% of gas was saturated with the reservoir. The modeling result verified that there is no gas in the reservoir.

The observation was also validated by the synthetic gathers which is shown in Figure 4-27. The gathers from the pure gas and mix of 5% gas scenario show very high amplitudes and they increase with offset. The synthetic gather also indicates there is no gas in the target reservoir.

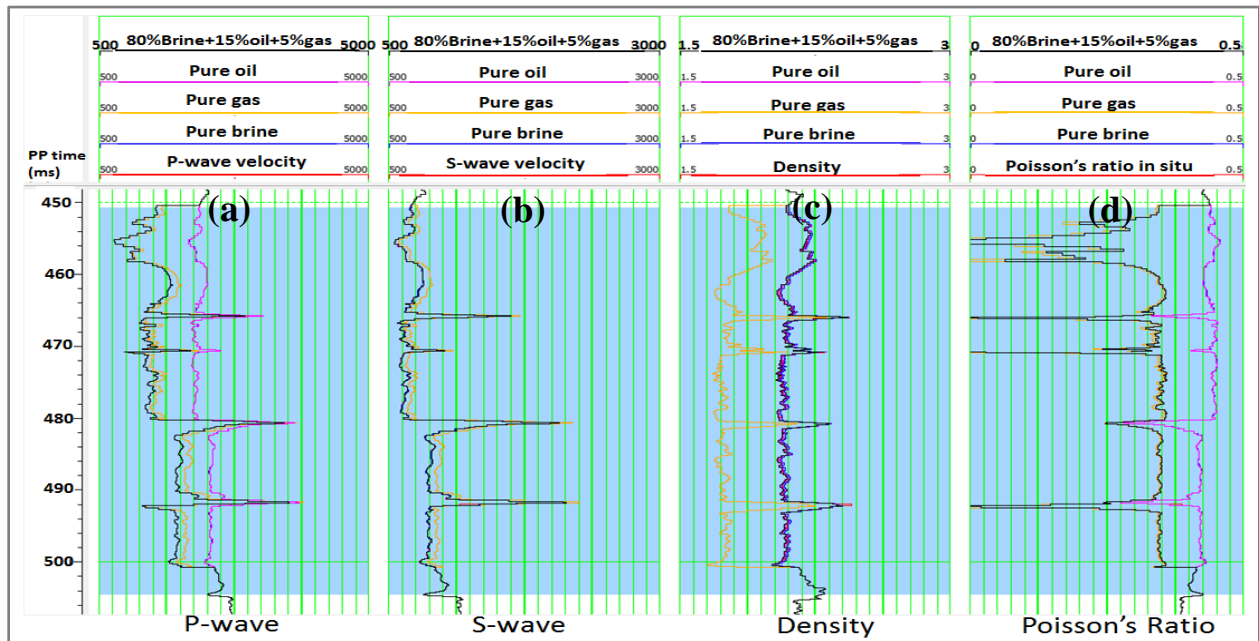


Figure 4-26. Estimated logs from AVO modeling. (a) P-wave, (b) shear-wave, (c) density and (d) Poisson's ratio logs. The reservoir is highlighted by the blue color.

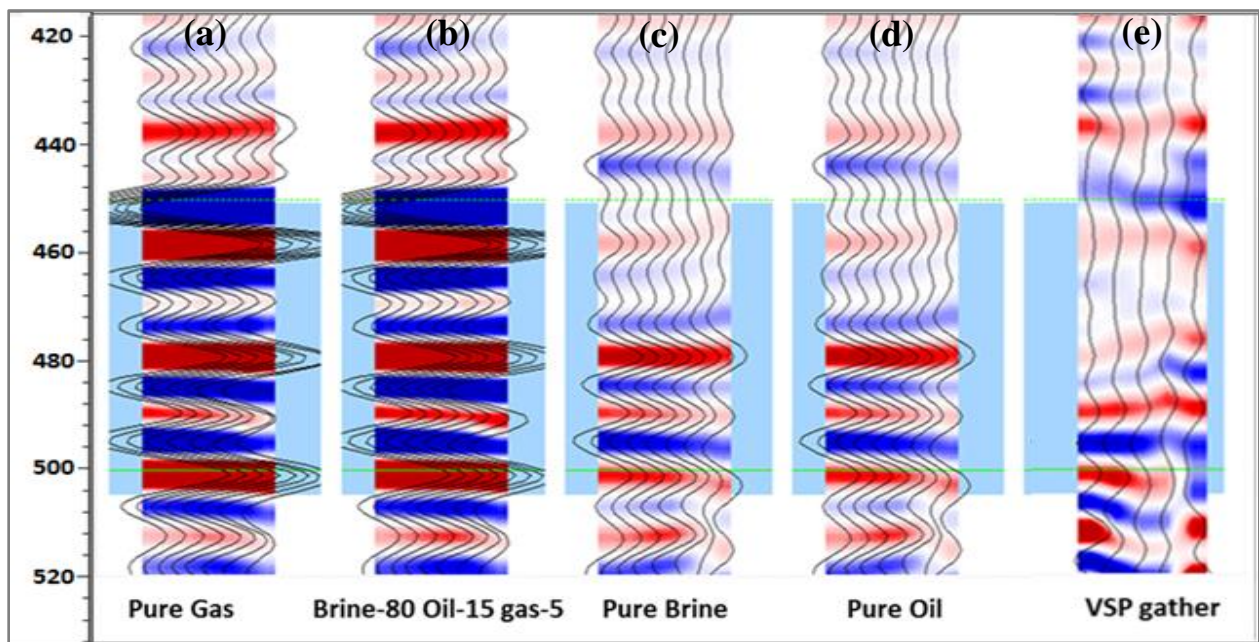


Figure 4-27. Comparison of synthetics created in different scenarios in AVO modeling and VSP gather. Reservoir zone is highlighted by the blue color. (a) Synthetic from pure gas, (b) 80% brine with 15% oil and 5% gas, (c) pure brine, (d) pure oil, and (e) VSP data.

Estimation from AVO modeling is compared to the production data which are listed in Table 4-3. The values in the table show, from 1984 to 1985, the total production of gas is 8 c<sup>3</sup>m<sup>3</sup>, it is only about 0.05% of total production. The production data confirmed the AVO modeling results.

Table 4-3. Production of the well A, target formation

	Gas (c <sup>3</sup> m <sup>3</sup> )	Oil (m <sup>3</sup> )	Water (m <sup>3</sup> )	Gas%	Oil%	Water%
<b>F12 Mo Prod</b>	0	434	7443	0%	5.5%	94.5%
<b>L12 Mo Prod</b>	8	641	7267	0.1%	8.1%	91.8%
<b>Cumulative Prod</b>	8	1075	14710	0.05%	6.81%	93.14%

Since the 9-10 API bitumen shows similar attributes with water, from AVO modeling, it is hard to estimate the portion of water and oil contents. I need to combine other information to predict the production but there are a few considerations regarding the estimation. The well used in interpretation was logged in 1981 which is before the steam injection and production, the oil is likely to be over estimated and water is likely to be underestimated. The study well was injected with steam of 13994 m<sup>3</sup> from 1984/02 to 1985/12. The errors of estimated fluid may also occur from cooling down of injected steam, which could become water. In addition to that, the oil volume may shrink when the dissolved gas comes out. Taking into account all the aspects can improve the accuracy of our predictions.

#### 4.2.6 PP-PS joint inversion

Joint PP-PS inversion can provide additional value and reduce risk or uncertainty in fluid/lithology discrimination and reservoir characterization. The challenges encountered in PP-PS registration and techniques applied in this work were discussed in Chapter 3.

Figure 4-28 shows PP-PS joint inversion results. In general, the joint inversion results show lower resolution compared with P-wave only inversion. Due to the lower resolution of PS image. The low resolution also degraded reliability of the joint inversion results. Comparing impedance from the joint inversion to previous inversion results, they show similar characteristics. All the P-impedance sections show lower P-impedance values inside the reservoir while the S-impedance does not change very much. It indicates that the S-wave velocities have little or no changes

when the reservoir is saturated with fluid. It also implies that the reservoir has no gas effects. Stable density and decreasing  $V_p/V_s$  also validated the interpretations.

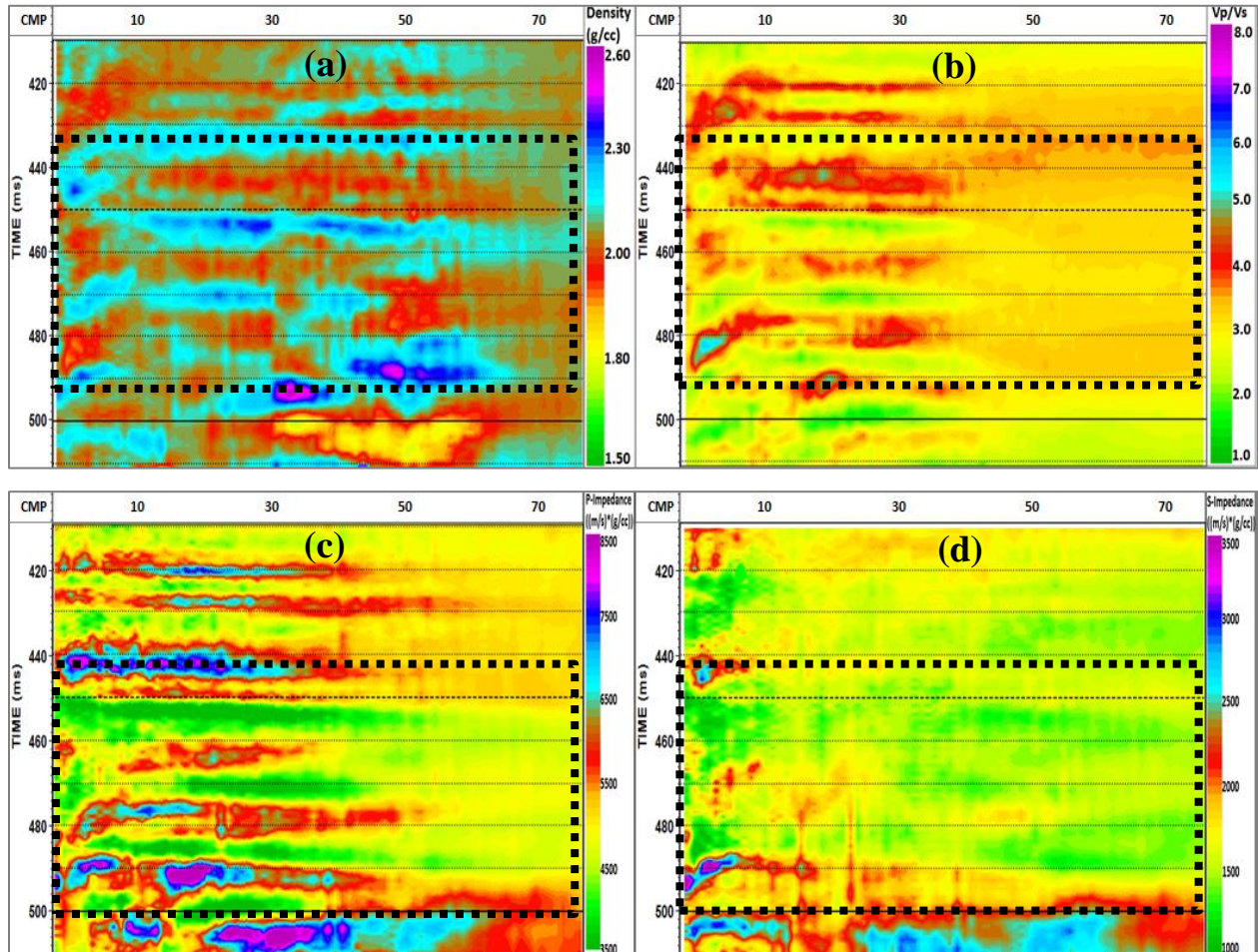


Figure 4-28. Inverted (a) density, (b)  $V_p/V_s$ , (c)  $Z_p$ , (d)  $Z_s$  from PP-PS joint inversion. The reservoir is highlighted by a rectangle.

Figure 4-29 shows crossplots of S-impedance vs P-impedance and S-impedance vs  $V_p/V_s$  from the PP-PS joint inversion. Compared with the P-wave only inversion result (Figure 4-22), these crossplots show the overlying shale, the top sand and the bottom water sand are in different locations. This distribution is another indicator of lithologies and hydrocarbons. The overlying shale shows high  $Z_s/Z_p$  and low  $V_p/V_s$ , and the top sand shows low  $Z_s/Z_p$  but higher  $V_p/V_s$ . Compare to the top sand, the bottom reservoir sand shows increasing  $Z_s/Z_p$  and decreasing  $V_p/V_s$  which may be caused by oil and water. These crossplots confirmed that the PP-PS joint inversion added additional value to interpretations from P-wave data only.

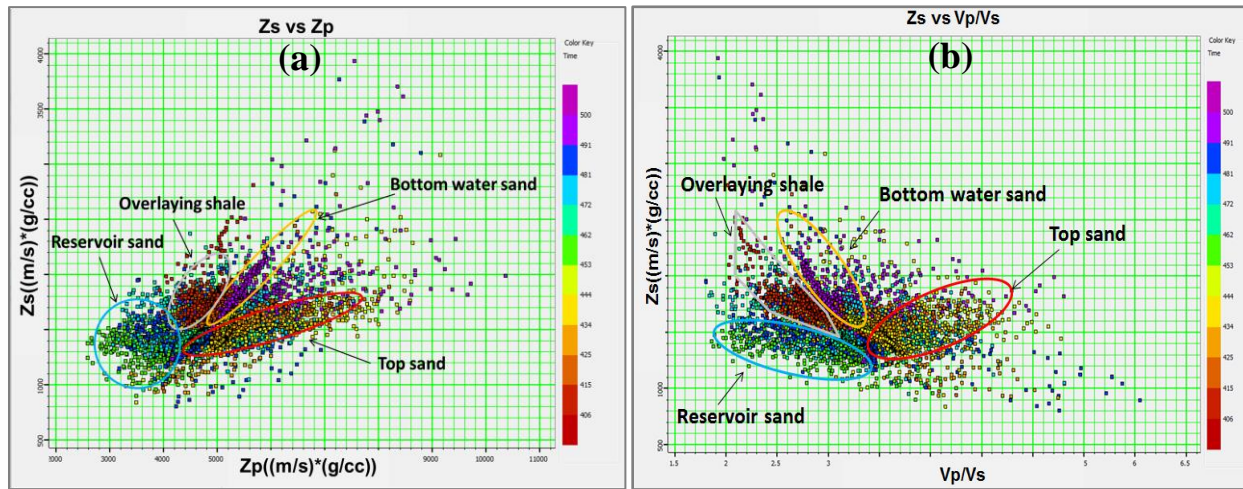


Figure 4-29. (a) Crossplot of S-impedance vs P-impedance from PP-PS joint inversion. (b) Crossplot of S-impedance vs  $V_p/V_s$  inverted from PP-PS joint inversion.

### 4.3 Chapter summary

Due to the advantages of VSP geometry, the hydrocarbon effects may be more visible on VSP than surface seismic sections. In this work, a VSP dataset from a heavy oil reservoir was used to predict rock properties and monitor production. P and S-wave impedance, reflectivity,  $V_p/V_s$  and density were inverted from post-stack and pre-stack inversion. Those properties are related to changes in the sedimentary environment and control the AVO responses. AVO analysis and modeling show no obvious gas effects in the study interval which was validated by production data. PP-PS joint inversion added value to P-wave only interpretations. Inverted rock properties and their crossplots, AVO Lambda-mu-rho analysis are effective tools to predict lithologies and hydrocarbon in the studied reservoir. However, the lower resolution of shear wave image and the distance of studied well and VSP borehole as well as absence of S-wave log may degrade the reliability of the detailed interpretation.

## **CHAPTER 5      DISCUSSION AND CONCLUSIONS**

### **5.1 Conclusions**

In this work, a multicomponent walkaway VSP experiment was successfully processed and analyzed to predict the rock properties of a heavy oil reservoir.

In acquisition, the small receiver interval helped to record different wave modes. Techniques and workflows for the VSP processing were introduced. In order to provide reliable interpretations, special attention was taken for the true amplitude recovery in processing. Both post-stack image and pre-stack gathers were obtained for inversion and AVO analysis. A common shot reflectivity gather was also created for AVO study at the VSP well location.

P and S-wave impedance, reflectivity,  $V_p/V_s$  and density were determined from post-stack and pre-stack inversion. Those properties are related to changes in the sedimentary environment and constrain the AVO response. AVO attributes and their crossplots were studied and AVO Lambda-mu-rho analysis as well as AVO modeling were conducted. These analyses helped to identify different lithologies and changes of fluids in the target reservoir. The study showed no obvious gas effects in the target interval which was validated by production data.

In this work, the converted-wave data had good resolution and added value to reservoir characterization. PP-PS joint inversion added more details to P-wave only interpretation. The overlaying shale, top sand, reservoir sand and bottom water sand are discriminated by PP-PS joint inversion.

This case study demonstrated that multicomponent VSP is an effective tool to predict rock properties, characterize the reservoir and monitor production.

### **5.2 New achievements of this research**

It is a comprehensive case study of a heavy oil reservoir. New achievements of this work include integrating of converted-wave data, VSP survey, inversion and AVO analysis into the heavy oil reservoir characterization; taking advantages of the converted-wave data and VSP surveys to better describe the reservoir. Compared to conventional surface seismic survey, the VSP geometry yields better resolution and higher signal-to-noise ratio data. Therefore, the hydrocarbon effects may be more visible on VSP data. In addition, the zero-offset VSP shot provides accurate velocity which was applied to seismic data processing and time-depth conversion. The accurate time-depth conversion is critical for heavy oil reservoir production and

SAGD operations. VSP data also yielded high quality converted-wave data, which were used to conduct PP-PS joint inversion. The converted-wave data improved the accuracy of lithology and fluid discrimination. All these achievements help geologists to design new wells and help engineers to monitor and control productions.

### **5.3 Discussion and future work**

In general, a robust interpretation was obtained. But, there are a few aspects that need to be improved or have effects on reliability of the interpretation which are discussed as follows.

In acquisition, the shot offsets vary from 11 m to over 1031 m. For the large offset shots, the refractions and reflections interfered with the direct arrivals and were a significant challenge for processing. Considering the shallow depth of the target reservoir (about 500 m), the large offset shots have big incident angles that are not reliable for AVO analysis. In this work, the processing and interpretation were focused on zero to middle offset shots. The learnings from this project can be used to instruct geometry design for the future VSP surveys. For example, if the depth and velocities of the target interval can be estimated from the previous seismic data or well logs, accordingly, a reasonable offset range and shot interval can be designed before acquisition. These parameters help to obtain good quality seismic data and reduce the cost in acquisition.

In processing, special attention was taken for the true amplitude recovery which includes exponential gain. It is an alternative approach to compensate the Q attenuation. For the VSP survey, the downgoing wave is recorded which has great advantage in estimation of the Q value. Accurate estimation of Q could improve the processing and interpretation.

In this project, the S-wave velocity log is absent. It is also difficult to pick up first arrivals of converted-wave on seismic data. Alternatively, the S-wave velocities were achieved by a velocity scan. But this manual velocity scan method has limited resolution. In future work, ray tracing would be a better solution and may provide more accurate S-wave velocity field of the subsurface.

PSDM was tested in this work and it transformed PP and PS data from time into depth domain and tied the same reflections automatically. However due to the inaccuracy of estimated S-wave velocity and small aperture of the VSP survey, the quality of migration was limited. I expect this experiment to bring more interest and attention on further development of VSP

migration techniques. Combining processed VSP traces with surface seismic traces may be a feasible solution.

The VSP survey was conducted in an abandoned well, so conventional geophone or other types of receivers work well. But in the SAGD production area, due to the high temperature and high pressure, the traditional receivers would fail. Instead, an optical fiber can work in this condition. Single sensor fiber optical VSP called Distribute Acoustic Sensor (DAS) VSP, which can permanently cemented in the borehole, is convenient for 4D survey. DAS-VSP holds promise for reservoir characterization in SAGD operations.

## REFERENCES

- Aki, K. and Richards, P. G., 1980, Quantitative seismology: Theory and methods, Volume **1**, W. H. Freeman and Co.
- Bale, R., Gratacos, B., Mattocks, B., Roche, S., Poplavskii, K. and Li, X., 2009, Shear wave splitting applications for fracture analysis and improved imaging: some onshore examples: *First Break*, Volume **27**, 73-83.
- Bubshait, S., 2010, VSP processing for coal reflections: M.Sc. Thesis, Department of Geoscience, University of Calgary.
- Carcione, J. M. and Cavallini, F., 2002, Poisson's ratio at high pore pressure: *Geophysical Prospecting*, Volume **50**, 97-106.
- Cary, P. and Zhang, C., 2010, Technical Considerations for Converted-Wave Prestack Time Migration: 2010 SEG Annual Meeting, Expanded Abstract.
- Castagna, J. P. and Backus, M. M., Eds., 1993, Offset-dependent reflectivity-Theory and practice of AVO analysis: *Soc. Expl. Geophys.*
- Castagna, J.P. and Swan, H.W., 1997, Principles of AVO crossplotting: *The Leading Edge*, Volume **16**, 337-342.
- Castagna, J. P., Swan, H. W., and Foster, D. J., 1998, Framework for AVO gradient and intercept interpretation: *Geophysics*, Volume **63**, 948-956.
- Cheadle, B.A., Dudley, J. S., Eastwood, J. E., Lovell, R. W. W., Reed, K., W., Stancliffe, R. P. W. and Van Wagoner, J.C., 1995, Integrated reservoir description for resource management at Cold Lake, Alberta; in *Proceeding, Exploration, Evaluation, and Exploitation 1995, The Economic Integration of Geology and Formation Evaluation: Canadian Society of Petroleum Geologists/Canadian Well Logging Society(CSPG/CWLS) Joint Symposium, Core Conference, June 1-2, Calgary, 14p.*
- Chopra, S., Alexeev, V., Xu, Y., 2003, Successful AVO and Cross-plotting: *Canada CSEG Recorder*, Volume **28**, No. 09

- Chopra, S. and D. Pruden, 2003, Multiattribute seismic analysis on AVO-derived parameters: The Leading Edge, Volume **22**, 998-1002.
- Coulombe, C. A., Stewart, R. R., and Jones, M. J., 1996, AVO processing and interpretation of VSP data: Canadian Journal of Exploration Geophysics, Volume **32**, 41-62.
- Gassmann, F., 1951, Uber die Elastizitat poroser Medien: Vierteljahrsschrift der Naturforschenden Gesellschaft in Zurich, **96**, 1-23.
- Garotta, R., 1987, Two-component acquisition as a routine procedure, in Danbom, S. H., and Domenico, S. N., Eds., Shear-wave exploration: SEG, Geophysical development series 1, 122-136.
- Goodway, B., Chen, T. and Downton, J., 1997, Improved AVO fluid detection and lithology discrimination using Lamé petrophysical parameters;  $\lambda\rho$ ,  $\mu\rho$  and  $\lambda/\mu$  fluid stack from P and S inversions: CSEG National Convention Expanded Abstracts, 148-151.
- Goodway, B., 2001, AVO and Lamé constants for rock parameterization and fluid detection: CSEG Recorder, Volume **26**, 39-60.
- Greenberg, M. L., and J. P. Castagna, 1992, Shear-wave velocity estimation in porous rocks: Theoretical formulation, preliminary verification and applications: Geophysical Prospecting, Volume **40**, 195–209.
- Hall, K. W., Lawton, D. C., Holloway, D., and Gallant, E. V., 2012, Husky 2011 walkaway 3C-VSP: CREWES Research Report, Volume **24**.
- Hardage, B. A., 1983, Vertical seismic profiling-principles (1st ed.): Amsterdam, Geophysical Press, 470.
- Hein, F., Weiss, J., and Berhane, H., 2007, Cold Lake Oil Sands Area: Formation Picks and Correlation of Associated Stratigraphy: The Alberta Energy and Utilities Board/Alberta Geological Survey (EUB/AGS) Geo-Note, 2006-03.
- Hilterman, F., 1989, Is AVO the seismic signature of rock properties? 59th Ann. Internat. Mtg., SEG, Expanded Abstracts, 559.

- Hinds, R. C., Kuzmiski, R. D., Botha, W. J., and Anderson, N. L., 1989, Vertical and lateral seismic profile: Geophysical Atlas of Western Canadian Hydrocarbon Pools, CSEG/CSPG, 319-344
- Hinds, R. C., Anderson, N. L., and Kuzmiski, R. D., 2007, VSP interpretative processing: Theory and practice: SEG Continuing Education Course Notes.
- Hinds, R.C., and Kuzmiski, R.D., 2001, VSP for the interpreter/processor for 2001 and beyond: part1, CSEG Recorder, Volume **26**, 84-95.
- Lawton, D.C, Gary, M. F., and Stewart, R. R., 2012, Reflections on PS: An interactive discussion of problems and promise in converted-wave exploration: CREWES Research Report, Volume **24**.
- Lines, L. R., and Newrick, R. T., 2004, Fundamentals of geophysical interpretation: Geophysical Monograph Series, Number 13, Society of Exploration Geophysicists.
- Margrave, G.F., 2008, Methods of seismic data processing: Geophysics 557 Course Lecture Notes, Department of Geology and Geophysics, University of Calgary.
- Mattocks, B., Li, J., Roche, S. and Ronen, S., 2006, PS-Wave Azimuthal Anisotropy in a North American Carbonate Basin: EAGE 68th Conference & Exhibition, Expanded Abstract.
- Ramos, A.C.B., and Castagna, J. P., 2001, Useful approximations for converted-wave AVO: Geophysics, Volume **66**, 1721-1734.
- Ross, C.P., AND Kinman, D., L., 1995, Nonbright spot AVO: Two Examples: Geophysics, Volume **60**, 1398-1408.
- Rutherford, S. R. and R. H. Williams, 1989, Amplitude-versus-offset variations in gas sands: Geophysics, Volume **54**, 680–688.
- Shuey, R. T., 1985, A simplification of the Zoeppritz equation: Geophysics, Volume **50**, 609–614.
- Simm, R., and Bacon, M., 2014, Seismic Amplitude - an Interpreters Handbook: Cambridge University Press.

- Slotboom, R., Eaton, D. and Lawton, D., 1990, Improving converted-wave (P-S) moveout estimation: CREWES Research Reports, Volume **2**, 80-88.
- Stewart, R., Gaiser, J.E., Brown, R.J., and Lawton, D., 2002, Tutorial Converted-wave seismic exploration: Methods: Geophysics, Volume **67**, 1348-1363.
- Stewart, R., Gaiser, J. E., Brown, R.J., and Lawton, D., 2002, Tutorial Converted-wave seismic exploration: Applications, Geophysics, Volume **68**, 40-57.
- Tessmer, G. and Behle, A., 1988, Common reflection point data-stacking technique for converted waves: Geophysics, Volume **36**, 661-688.
- Wiggins, J.W., Ng, P., and Mazur, A., 1986, The relation between the VSP-CDP transformation and VSP migration: 55th Ann. Internat. Mtg., SEG Expanded Abstract.
- Wiggins, R., Kenny, G.S., and McClure, C.D., 1983, a method for determining and displaying the shear-velocity reflectivities of a geologic formation: European patent Application 0113944.
- Wu, B., Lawton, D. C., and Hall, K., 2014, Analysis of multicomponent walkaway vertical seismic profile data, CREWES Research Report, Volume **26**.
- Xu, C., and Stewart, R. R., 2003, Ross Lake 3C-3D seismic survey and VSP, Saskatchewan: A preliminary interpretation, CREWES Research Report, Volume **15**.
- Xu, C., and Stewart, R. R., 2003, Ross Lake 3C-3D seismic survey and VSP, Saskatchewan: A preliminary interpretation, CREWES Research Report, Volume **15**.
- Zoeppritz, K., 1919, Erdbebenwellen VIII B, On the reflection and propagation of seismic waves: Gottinger Nachrichten, I, 66-84.
- Zou, K., Dai, J., Xu, H., HannAn, A., and Koesoemadinata, A., 2006, A practical workflow of PP/PS event registration in multicomponent data interpretation: EAGE 68th Conference & Exhibition, Expanded Abstract.
- Zhang, D. and Lines, L., 2007, Effects of heavy oil cold production on Vp/Vs ratio: CREWES Research Reports, Volume **19**.

Zhang, H., and Brown, R. J., 2001, A review of AVO analysis: CREWES Research Report, Volume **13**.

Zhang, John J. and Bentley, Laurence R., 2005, Factors determining Poisson's ratio: CREWES Research Report ,Volume 17.